Numerical Aspects of the PUFEM for Efficient Solution of Helmholtz Problems

M Shadi Mohamed

Submitted for the degree of Doctor of Philosophy

Heriot-Watt University

School of the Built Environment

April 2010

Abstract

Conventional finite element methods (FEM) have been used for many years for the solution of harmonic wave problems. To ensure accurate simulation, each wavelength is discretised into around ten nodal points, with the finite element mesh being updated for each frequency to maintain adequate resolution of the wave pattern. This technique works well when the wavelength is long or the model domain is small. However, when the converse applies and the wavelength is small or the domain of interest is large, the finite element mesh requires a large number of elements, and the procedure becomes computationally expensive and impractical.

The principal objective of this work is to accurately model two-dimensional Helmholtz problems with the Partition of Unity Finite Element Method (PUFEM). This will be achieved by applying the plane wave basis decomposition to the wave field. These elements allow us to relax the traditional requirement of around ten nodal points per wavelength and therefore solve Helmholtz wave problems without refining the mesh of the computational domain at each frequency.

Various numerical aspects affecting the efficiency of the PUFEM are analysed in order to improve its potential. The accuracy and effectiveness of the method are investigated by comparing solutions for selected problems with available analytical solutions or to high resolution numerical solutions using conventional finite elements.

First, the use of plane waves or cylindrical waves in the enrichment process is assessed for wave scattering problems involving a rigid circular cylinder in both near field and far field. In the far field, the cylindrical waves proved to be more effective in reducing the computational effort. But given that the plane waves are simpler to analytically integrate for straight edge elements, during the finite element assembling process, they are retained for the remaining of the thesis.

The analysed numerical aspects, which may affect the PUFEM performance, include the conjugated and unconjugated weighting, the geometry description, the use of non-reflecting boundary conditions, and the h-, p- and q-convergence. To speed up the element assembling process at high wave numbers, an exact integration procedure is implemented.

The PUFEM is also assessed on multiple scattering problems, involving sets of circular cylinders, and on exterior wave problems presenting singularities in the geometry of the scatterer. Large and small elements, in comparison to the wavelength, are used with both constant and variable numbers of enriching plane waves.

Last, the PUFEM resulting system is iteratively solved by using an incomplete lower and upper based preconditioner. To further enhance the efficiency of the iterative solution, the resulting system is solved into the wavelet domain.

Overall, compared to the FEM, the PUFEM leads to drastic reduction of the total number of degrees of freedom required to solve a wave problem. It also leads to very good performance when large elements, compared to the wavelength, are used with high numbers of enriching plane waves, rather than small elements with low numbers of plane waves. Due to geometry detail description, it is practical to use both large and small elements. In this case, to keep the conditioning within acceptable limits it is necessary to vary the number of enriching plane waves with the element size.

Dedication

Once again here I stand looking back and forth. Looking to what have already been done and what still needs to be done. The last three years were too long yet were too short, too slow yet too fast. At this point when one part is just about to finish while another is just about to begin I want to take a break even though a short one to remember those without them life would have felt tasteless.

Abdo Rasho and Wa'hida Cieno, for your endless love.

The big one, Shereen, and the little one, Yara, for making life so colourful.

Mhyar and Farah for always being there.

To all of you I dedicate my work.

Acknowledgment

I am grateful to Dr. Omar Laghrouche not only for his advice and insightful comments but also for his patience and continuous support. He introduced me to the world of waves and guided me through so many ups and downs. It was an honor to work with him.

I am thankful to the UK Association of Computational Mechanics in Engineering (ACME). The ACME annual conferences were an important chance to meet different researchers and to learn from them. I am especially thankful to Professor Andrew Chan (Honorary Secretary), Professor Barry Topping (Honorary Treasurer) and Dr. Mohamed Rouainia (Charmian and organiser of ACME 2008) who awarded me "Best Paper by a Postgraduate Research Student in Computational Mechanics" which was a great encouragement and a great source of confidence.

I have learned a lot from my colleague Dr. Abdallah ElKacimi. He was an inspiration in work as in life.

I would like to express my gratitude to Heriot Watt University for awarding me James Watt scholarship. Without their financial support this work would not have been possible.

Contents

List of Tables

List of Figures

Notation

x, y and z: Cartesian coordinates.

r and θ: polar coordinates.

a: radius of a scattering body.

$a_j, x_j, y_j, \alpha_{jp}$ and R_{jp}: spatial attributes of a system of multiple scatterers.

λ: wavelength.

m: number of enriching plane waves.

m_j: number of enriching plane waves at node j.

n: number of nodes in a finite element.

i: imaginary number ($\mathrm{i}^2 = -1$).

k: wave number.

J_q: Bessel function of the first kind and order q.

H_q: Hankel function of the first kind and order q.

J'_q: derivative of the Bessel function with respect to the argument.

H'_q: derivative of the Hankel function with respect to the argument.

ϕ_I: potential of an incident plane wave.

ϕ_S: potential of a scattered plane wave.

ϕ_{T}: sum of the potentials of the incident and the scattered waves.

Ω: considered computational domain.

Ω_{area}: domain area.

Q_{min} and n_{min}: minimum number of components to be considered in analytical solutions.

R: distance of the farthest considered point of the computational domain from the center of the scatterer.

R^{in}: interpolated value of the radius R.

R^{ex}: exact value of the radius R.

ε_1: relative error on the interpolated radius R^{in}.

NC: number of scatterers in a multiple scattering problem.

$\underline{\nabla}$: gradient vector operator.

∇^2: Laplace operator.

c: propagation speed in the wave equation.

C: constant used to evaluate m_j.

ω: circular frequency.

Γ: domain boundary.

Ω_e: area of an element.

Γ_e: boundary of an element.

Γ_i: boundary of the scatterer number i.

Γ_r: outer boundary of a circular domain.

$\underline{\mathrm{n}}$: outward normal vector.

$\mathrm{n_x}$ and $\mathrm{n_y}$: components of the outward normal vector in a Cartesian coordinate system.

ϕ_j: nodal value of the potential at the node j.

A_l^j: amplitude factors in the PUFEM.

ψ_l: enriching function.

N_j: polynomial shape function.

p: order of the polynomial shape function.

$W_{(j-1)m+l}$: Weighting function.

$P_{(j-1)m+l}$: new shape function in the PUFEM.

i, j, l, p and q: indices of summation.

$\mathbf{K}^e, \mathbf{M}^e$, and $\mathbf{C}^e$: element matrices.

$\mathbf{A}^e$ and $\mathbf{F}^e$: element amplitude and load vectors.

$\mathbf{U}$: global system matrix.

n_{tot}: total number of nodal points in the computational domain.

n_{gauss}: number of Gauss integration points.

ε_2: L_2 norm error.

ε_2^i: L_2 norm error of the numerical solution based on the interpolated geometry.

ε_2^e: L_2 norm error of the numerical solution based on the exact geometry.

h: element size.

h_j: size of the longest edge connected to the node j.

τ: number of degrees of freedom per wavelength.

κ: condition number.

DOF: degrees of freedom.

BGT-1 and -2: Bayliss-Gunzburger-Turkel first and second order.

B: non-reflecting boundary condition operator.

B_l^p: unknowns in the multiple scattering analytical solution.

$Y(x, y)$: general polynomial.

(.): dot product.

$\underline{\mathrm{d}}$: direction vector.

$\underline{\mathrm{x}}$: position vector.

$I_l(Y(x, y))$: Area integral of the multiplication of a general polynomial $Y(x, y)$ with an exponential function.

$G_l(Y(x, y))$: Line integral of the multiplication of a general polynomial $Y(x, y)$ with an exponential function.

Γ_{ij}: edge i, j of a finite element.

$\underline{\mathrm{s}}_i$: position vector of the node i of a finite element.

$\underline{\mathrm{g}}_{ij}$: vector going form the node i to the node j of a finite element.

$totdof$: total number of degrees of freedom.

$totsys$: total number of stored entries of the system matrix.

$\mathbf{A}$: coefficients matrix of a linear system of equations.

$\mathbf{x}$: unknowns vector of a linear system of equations.

$\mathbf{b}$: right hand side vector of a linear system of equations.

$\mathbf{r}_k$: residual of the approximate solution vector $\mathbf{x}_k$ at the kth iteration.

$\mathbf{v}_{k+1}$: norm of the vector $\mathbf{r}_k$.

$\mathbf{v}$: general vector of n components.

$\mathbf{Q}$: preconditioning matrix.

$\mathbf{L}$: lower matrix resulting from matrix $\mathbf{A}$ decomposition.

$\mathbf{U}$: upper matrix resulting from matrix $\mathbf{A}$ decomposition.

$\mathbf{A}'$: approximation of the matrix $\mathbf{A}$.

$\mathbf{E}$: difference between the matrix $\mathbf{A}$ and its approximation $\mathbf{A}'$.

$lfill$: level of fill used in the incomplete LU factorization.

$dtol$: dropping tolerance used in the incomplete LU factorization.

z_j: low pass filter coefficients used in a discrete wavelet transform.

g_j: high pass filter coefficients used in a discrete wavelet transform.

s_j^{i+1}: wighted averages after applying a discrete wavelet transform i times.

d_j^{i+1}: wighted differences after applying a discrete wavelet transform i times.

p: order of a discrete wavelet transform.

$\mathbf{W}$: wavelet transform matrix.

Φ: zero matrix.

$\mathbf{I}$: identity matrix.

$\tilde{\mathbf{A}}$: matrix $\mathbf{A}$ transformed via a discrete wavelet transform.

$\tilde{\mathbf{x}}$: vector $\mathbf{x}$ transformed via a discrete wavelet transform.

$\tilde{\mathbf{b}}$: vector $\mathbf{b}$ transformed via a discrete wavelet transform.

$\mathbf{W}^\top$: transpose of matrix $\mathbf{W}$.

ε: tolerance for the termination criterion used with the iterative solver.

$iter$: number of iterations needed to solve the linear system.

NNZ: non-zero entries in the system matrix.

$NNZc$: non-zero entries in the conditioned system matrix.

List of publications

No part of the work referred to in this thesis has been submitted in support of an application for another degree or qualification of this or any other university. However some parts of the material contained herein have been previously published in the following papers:

Refereed journals

- M.S. Mohamed, O. Laghrouche, A. El Kacimi. "*Some numerical aspects of the PUFEM for efficient solution of 2D Helmholtz problems*". Computers & Structures, in print, doi:10.1016/j.compstruc.2010.01.012.

- O. Laghrouche, M.S. Mohamed. "*Locally enriched finite elements for the Helmholtz equation in two dimensions*". Computers & Structures, in print, doi:10.1016/ j.compstruc.2008.04.006.

Proceedings

- M.S. Mohamed, O. Laghrouche, J. Trevelyan. "*A q-adaptive partition of unity finite element method for the solution of the 2-D Helmholtz equation.* WCCM/APCOM 2010, The 9th World Congress on Computational Mechanics and 4th Asian Pacific Congress on Computational Mechanics, Sydney, Australia 2010.

- M.S. Mohamed, A. El Kacimi, O. Laghrouche. "*Multi-wavelength sized finite elements for Helmholtz wave problems*". WAVES 2009, The 9th International Conference on Mathematical and Numerical Aspects of Waves, University of Pau, France, 2009.

- M.S. Mohamed, A. El Kacimi, O. Laghrouche. "*Exact integration scheme for the solution of Helmholtz problems with the PUFEM*". ACME 2009, The 17th UK Conference of the Association of Computational Mechanics in Engineering, The University of Nottingham, UK, 2009.

- M.S. Mohamed[1], O. Laghrouche. "*Partition of unity finite element method for the Helmholtz equation: Conjugated versus unconjugated formulation*". ACME 2008, The 16th UK Conference of the Association of Computational Mechanics in Engineering, Newcastle University, UK, 2008.

- O. Laghrouche, M.S. Mohamed. "*Locally enriched finite elements for the Helmholtz equation*". ACME 2007, The 15th UK Conference of the Association of Computational Mechanics in Engineering, University of Glasgow, UK, 2007.

[1]Won the prize of *Best Post-graduate Research Student* at *ACME 2008*.

Chapter 1

Introduction

1.1 Waves and the Helmholtz equation

The word wave is the modern form of the ancient English word "wafian" that its origin goes back to Indo-European roots. It probably goes even further back to very early stages in the human history. We have always been in contact with phenomena that we call waves. First water-surface disturbances, later sound and more recently light and gravity all these are understood as forms of waves. Although these phenomena share many physical aspects, like for example radiating from a source and fading as getting away, still each one of them is unique. Therefore it has always been difficult to find a general definition or a mathematical model that is valid for all waves.

1.1.1 Waves definition

Observing water, people used to think of waves as a disturbance in a medium. Although this is true for mechanical waves but it was an obstacle to understand how electromagnetic waves, including light, propagate in vacuum. Therefore it took humanity too long to understand what is called today electromagnetic waves. Newton argued against the wave-nature of light. In his article entitled "An hypothesis explaining the properties of light" he stated that light is composed of particles which are emitted everywhere from a shinning object [1].

By the 19th century Maxwell demonstrated with his set of equations that electric and magnetic fields behave like waves and that light is a form of what he called "an electromagnetic disturbance in the form of waves propagated through the electromagnetic field according to electromagnetic laws" [2]. Later Hertz was able to measure the electromagnetic waves experimentally [3]. Still at that time people did not accept the fact that electromagnetic waves propagate in a vacuum. Instead it was common to think that electromagnetic waves propagate in Ether which was thought of as a substance that fills the universe. It was only by the beginning of the 20th century that Einstein explained in the special relativity theory that Ether does not exist and electromagnetic waves travel in vacuum and in matter [4].

In our current understanding, the term wave may be defined as: "a pattern of matter or energy that is spread over a volume of space" [5, 6], "A wave behaves like a material particle in very particular conditions but has more characteristic parameters than a particle" [7] and "a disturbance that carries energy from one place to another" [8]. Or one may simply say that a wave is a from of energy transmittance through a medium. A form that did amaze the human being through out the history and it still does today.

1.1.2 Mathematical models of waves

Since the 16th century mathematicians and physicians have started to work on mathematical models of wave problems. Euler, Lagrange, Bernoulli, and d'Alembert studied the problem of a vibrating string [9, 10]. These studies later lead to the wave equation which can model mechanical waves including the string vibration. Apart from this, Maxwell was the first to propose a mathematical model for electromagnetic waves through the set of equations named after him.

One of the most important mathematical models proposed in this regards is the elliptical partial differential equation that is named after the German physician Hermann von Helmholtz. The importance of the Helmholtz equation comes from the fact that the mathematical models of mechanical and electromagnetic waves could be reduced to this equation.

The wave equation which describes many mechanical waves leads to the Helmholtz

equation when a harmonic solution is considered [11] while for an electromagnetic wave and starting from Maxwell's equations both electric and magnetic fields might be expressed in a mathematical form similar to the wave equation which may again be reduced to the Helmholtz equation [12]. This makes solving the Helmholtz equation particularly interesting in physics.

1.2 Wave problems and numerical methods

Wave problems are encountered in many engineering fields including aerospace engineering (radar), civil engineering (earthquake exposed structures, offshore structures), mechanical engineering (noise and vibration control), optical engineering (laser) and many other fields. Solving these problems is becoming ever more important as many modern technologies based on wave applications are becoming part of our everyday life. Microwave ovens, mobile phones and GPS systems are only some examples.

To solve a wave problem or the partial differential equation describing this problem, two approaches are possible. Indeed other approaches are possible as well such as statistical approaches but the discussion here will be limited to what is called deterministic approaches. The first approach consists to develop an analytical solution for the problem. In references [11] and [13] to [16] the analytical solutions of many classical wave problems are described. However, these solutions are limited to idealized geometries and homogeneous domains. Even with these limitations it is virtually impossible to find such a solution for every problem. The second approach is to find an approximate solution so that instead of searching for a complicated function that satisfies the differential equation a much simpler function or combination of functions are sought that can well approximate the solution.

This latter approach is developed based on numerical methods which were not obvious until the recent revolutionary development in the computing facilities. In the last two decades of the twentieth century an intensive work was undertaken to develop numerical methods for the solution of partial differential equations. Because of this advancement many real world problems which were previously unsolved or only solved with poor approximations are now solvable and with much improved

approximations.

Many numerical methods are quite flexible and general that they can practically be applied to any partial differential equation. Some of the most common numerical methods in engineering are the Finite Element Method (FEM) and the Boundary Element Method (BEM) (see references [12] and [17] to [21]).

1.3 Enrichment methods

The rapid advancement in computing facilities has continuously increased the range of problems that can be solved numerically. However, when solving a wave problem, in order to get an acceptable level of accuracy, the domain should be meshed with a discretization level of about seven to ten nodal spaces per wavelength [17, 19, 20]. As higher wave numbers are considered this requirement increases to even more than ten nodal spaces per wavelength. This is due to the so-called pollution error [22, 23]. Considering a large domain and a short wavelength, the required number of degrees of freedom may become prohibitively large which is a limitation for numerical methods [24]. An example of such a problem [25] could be a radar wave scattered by an aircraft where the radio wavelength is of a few millimetres whereas the aircraft size is of tens of meters. Considering a cube computational domain with the side length being 20 m and the incident wavelength being 2 cm, the model requires 10^{12} complex nodal variables and a storage of 1.6×10^{21} bytes for a finite element solution using a classical direct solver. Although 20 m is not large for an aircraft and 2 cm is not small for a radio wavelength but clearly the computational cost is severely large even on supercomputers.

Many efforts have been invested to extend the wavelength range where the numerical methods are applicable, which has lead to some promising outcome. A major break through came from an idea suggesting to enrich the methods with the analytical solutions of the differential equation. Although the enriched methods may lack some of the generality of the original ones but the results show a dramatic reduction in the computational effort in terms of memory and CPU time.

In the next sections, the main contributions to the solution of wave problems with

the enriched numerical methods are highlighted. Because this thesis is devoted to the solution of the Helmholtz equation with locally enriched finite element spaces a special attention is paid to the developments in this research area.

1.4 Finite element methods

1.4.1 Partition of unity finite element method

In his PhD thesis "On Generalized Finite Element Methods" Melenk [26] proposed the Partition of Unity Finite Element Method (PUFEM). His idea might be summarized as building a finite element space where *a priori* knowledge of the solved differential equation is included. Unlike the conventional finite elements where the solution is approximated with polynomial trial functions, here the trial functions are constructed by incorporating the physical feature of the problem. To achieve this, functions with desired local approximation properties are considered on the problem domain. Then by multiplying these functions with the trial functions on each element a global finite element space is constructed with also the desired approximation properties and without losing the conformity of the trial functions.

It is proven in his thesis that under the weak formulation the global space has the same approximation properties of the local approximation spaces which are derived for the Laplace, the Helmholtz, and the two-dimensional elasticity equations. For the Helmholtz equation two types of approximation spaces are identified: a space generated by a set of plane wave basis functions and a space generated by generalized harmonic polynomials based on Vekua functions.

This work was published later in two journal papers. In reference [27] Melenk and Babuška showed the classes of problems where the proposed method could be efficient. The method is demonstrated through the solution of some Helmholtz problems at high wave numbers. In reference [28] a proof of convergence is presented and the results of some numerical tests are also shown.

A similar approach was proposed by Mayer and Mandel [29] for the Helmholtz equation where the linear shape functions in the FEM are multiplied with a combination of plane waves propagating in different directions. The method is used to solve

a plane wave propagation problem. Although the incident wave is not contained in the approximating set of plane waves, the results show accurate approximation properties of the proposed approach.

Laghrouche *et al.* [30] to [34] are among the first to use the PUFEM to solve wave scattering problems with various shapes in both two-dimensions and three-dimensions. The finite element space is enriched with plane waves where the potential at each node of the meshed domain is expressed as a combination of uniformly distributed plane waves. The method is implemented to solve propagation problems of a single plane wave and a Hankel source wave, and then to solve wave scattering problems using elements spanning many wavelengths. The results show a large reduction in the required number of degrees of freedom compared to the conventional finite element method [30].

In a second paper [31], further numerical aspects of this method including the conditioning and the numerical integration are presented and discussed. The number of enriching plane waves is changed from one node to another. The enriching plane waves are clustered around a direction of preference instead of evenly distributing them. This further reduced the total number of degrees of freedom required to solve a problem. This approach is demonstrated with numerical examples. The efficiency of the PUFEM is tested in wave scattering problems where elliptical scatterers are considered. However, it is noted that the PUFEM faces stability problems due to ill conditioning of the system matrix at a high number of enriching plane waves.

In further work [32, 33], the PUFEM is implemented for the solution of the three-dimensional Helmholtz problems where a numerical example of a plane wave diffracted by a sphere is used to demonstrate the efficiency of the method. Then the PUFEM is extended to solve problems with a sudden change in the wavelength [34], where the finite elements on each side of the change are enriched with plane waves of the relevant wavelength. The continuity at the interface is enforced through Lagrange multipliers. The method is implemented to solve a plane wave diffraction problem where a circular scatterer is immersed in water with discontinuity in the water depth.

In a recent work El Kacimi and Laghrouche [35] implemented the PUFEM for the solution of the two-dimensional elastic wave equations where the displacement field is approximated via the standard finite element shape functions enriched by pressure

(p) and shear (s) plane waves. The method is used to solve scattering problems where p and s waves impinge in a circular rigid body at high frequencies in an elastic medium. The results show a very good accuracy in approximating the displacement field. In this context, the performances of the 4-noded and the 9-noded elements are compared based on the quality of the results and the conditioning in reference [36]. Laghrouche and Mohamed [37] investigated enriching the PUFEM with Vekua functions instead of the plane waves enrichment for the solution of acoustic wave scattering where the computational domain is placed at various distances from the scatter. The enriched finite elements show a significant improvement of the accuracy of the PUFEM at the far field with Vekua functions.

Astley *et al.* [38] solved inhomogeneous two-dimensional mean flow problems using the PUFEM with plane waves enrichment. The results show a better performance when the method is compared to the FEM. Later, Gamallo and Astley [39] extended this work by enriching the solution space with plane waves with the wave number being a function of the Mach number related to the flow movement. They investigated the accuracy and the conditioning of the numerical solution for a range of frequencies and Mach number characteristic of aero-engine bypass ducts. The results show the good performance of the method.

A further development is presented by Mertens *et al.* [40] where an infinite partition of unity method is developed and coupled with the PUFEM to solve acoustic flow problems in unbounded domains. Numerical examples are presented to show the advantages of this coupling compared to the classical coupling of the finite and infinite element methods.

Ortiz and Sanchez [41] investigated the Higdon boundary condition [42] on the exterior domain and tried a generalized conjugate gradient solver [43] to deal with the conditioning problem. They presented an exact integration scheme which leads to a reduction of the number of operations needed in comparison to the numerical integration scheme. Later, Ortiz [44] extended the previous work by considering a smoothly varying wavenumber through the problem domain. For the enrichment, he proposed plane waves with an interpolated wave number to reflect this variation. The advantages of the proposed method are shown with numerical examples in comparison to the conventional finite element method.

1.4.2 Generalized finite element method

The previously mentioned partition of unity technique is implemented in the Generalized Finite Element Method (GFEM) by Stroubuolis *et al.* [45]. Again here the finite element space is enriched with local approximating functions pasted at the mesh vertices. In reference [46] different aspects and advantages of the GFEM are discussed.

Stroubuolis *et al.* authored a two-part paper on the solution of the Helmholtz equation with the GFEM. In part I [47], the convergence of the method is discussed. Numerical examples are used to show the efficiency of the method. While in part II [48], the effect of using different approximating functions and the contribution of the boundary conditions to the solution error are addressed. It should be mentioned that the effect of the approximating functions is discussed by the same authors in another work but in the context of the PUFEM [49]. Stroubuolis *et al.* stated that the plane wave enrichment is a favorable choice because it involves only trigonometric functions for which the integrals are evaluated numerically at a lower cost compared to the Bessel functions which are included in Vekua functions.

1.4.3 Discontinuous enrichment method

The Discontinuous Enrichment Method (DEM) proposed by Farhat *et al.* in reference [50] belongs to a class of the finite element methods that is called the Discontinuous Galerkin Method (DGM) [51]. Unlike the PUFEM, in the DEM the plane waves are added to, rather than multiplied by, the shape functions. Therefore the DEM is discontinuous and the continuity is weakly enforced with Lagrange multipliers applied at element boundaries.

An important advantage of this approach is the possibility of evaluating the integrals, needed for elementary matrices, analytically which leads to a big reduction in the computation time if the elements are multi-wavelength sized. The method is tested in solving some one- and two-dimensional Helmholtz problems. The results suggest that the solution with the DEM has a better conditioning compared to the PUFEM. In another work by Farhat *et al.* [52] further numerical tests are performed to show the efficiency of the method compared to the FEM. Again it is showed that the

resulting system is better conditioned compared to the PUFEM. In following papers by Farhat *et al.* the DEM is extended to solve three-dimensional Helmholtz problems [53, 54] and the two-dimensional elastic wave problems [55]. The numerical results, in these papers, show a significant efficiency improvement when the DEM is compared to the FEM. A proof of the method convergence and *a priori* error estimate for lower order elements is found in reference [56]. It should be added that many numerical aspects of the DEM are thoroughly examined in a paper authored by Grosu and Harari [57] where the pollution effect was studied.

An approach similar to the DEM was proposed by Gillman *et al.* [58], where oscillated polynomials are chosen as approximating functions. Again the continuity across element boundaries is weakly enforced through Lagrange multipliers. The efficiency of the new approximating functions is shown through solving two-dimensional Helmholtz problems. The results show similar performance when compared to the DEM.

1.4.4 Ultra weak variational formulation

The basic idea in the Ultra Weak Variational Formulation (UWVF) is to divide the problem's domain into subdomains/elements. In each element the weak formulation is derived in the same fashion like the FEM but with two considerations. First, extra boundary conditions are applied on the element interfaces to enforce the continuity between elements. Second, the trial functions are formed based on the analytical solution of the considered partial differential equation. Because the continuity is weakly enforced in this formulation, it is called ultra weak. This idea was first proposed and implemented by Cessenat and Despres [59, 60] with plane waves enrichment.

The UWVF was later adopted by Huttunen *et al.* [61] to solve the two-dimensional Helmholtz equation. The numerical examples suggest that solving wave problems with the UWVF is more efficient than the FEM. In this paper a severe conditioning problem is pointed out when the method is implemented in inhomogeneous problems or with unstructured mesh grids. The UWVF is extended to solve the time harmonic elastic wave equation in two-dimensions where the conditioning problem becomes even clearer due to the wave number discrepancy between the S-wave and the P-

wave [62]. The numerical results show that the UWVF is more efficient compared to the FEM. The method was extended later to solve the three-dimensional Helmholtz equation in reference [63].

Huttunen *et al.* [64] compared the UWVF to the PUFEM in two cases: an acoustic wave propagating in a rigid duct and a singular Helmholtz problem where the analytical solution of the problem has a singular derivative at a corner of a non-convex domain. In the first case the PUFEM leads to more accurate results for lower frequencies while the opposite is true for higher frequencies. Both methods suffer ill-conditioning but the UWVF presents a higher condition number. For the second case the results are satisfactory with both methods and could be improved with refining the mesh near the singularity.

1.4.5 Other methods

Other methods for the Helmholtz equation include the least-squares method presented by Monk and Wang [65] where plane wave basis and then Bessel function basis are used to approximate the solution of a scattering problem. The continuity across element boundaries is enforced through minimizing a least-squares quadratic functional.

The Hybrid Numerical Asymptotic Method was developed by Giladi and Keller [66], where the FEM space is enriched with asymptotically derived basis functions. This method is practically wave number independent and requires much fewer unknowns to achieve the same accuracy compared to the FEM. It was developed further and implemented in the BEM [67].

The Wave-Based Method (WBM), was proposed by Desmet in his PhD thesis [68] as an indirect Trefftz method. Unlike the FEM where approximate solutions are sought, the WBM tends to find the exact solution. This is achieved by finding the general solution of the governing differential equation and its particular solution over the whole domain. This is possible when the domain has a regular shape. Otherwise the domain is divided into relatively large subdomains of regular shapes. The main disadvantage of this method is the limitation to regular geometries. This is overcome by implementing a hybrid method FEM-WBM [69]. In this hybrid method,

the domain is divided into large regular sub-domains that are solved with the WBM while the rest of the domain is solved with the FEM. This hybrid method has the advantage of being unlimited to regular geometries thanks to the FEM, while the required computations are reduced significantly thanks to the WBM.

In a recent work by Barnett and Betcke [70] another non-polynomial based finite element method is introduced for acoustic scattering by non-smooth objects. A combination of Fourier and Bessel functions is used at the nodes of elements to enrich the method while the continuity across the element boundaries is ensured using a least square finite element formulation. It is shown that an exponential convergence is achieved through the increase of the number of basis functions. Some challenging numerical examples are solved including mono and multiple scattering problems where convex and non-convex scatterers with geometric singularities are considered.

1.5 Boundary element methods

The idea of enriching the FEM space with plane wave basis functions is implemented also in the BEM for the solution of Helmholtz problems. de La Bourdonnaye [71, 72] investigated this idea for scattering problems involving the Helmholtz equation at high frequencies. The conditioning problem of this method is studied in reference [73] where it is proposed to transform the linear system into the wavelet domain in order to improve the rate of the convergence of the solution.

Another contribution in this regard was published by Perrey-Debain *et al.* in reference [74] where the BEM is enriched with plane wave basis to solve problems governed by the two-dimensional Helmholtz equation. The method is used to solve wave scattering problems where circular scatterers are considered. Numerical aspects of the method namely the conditioning and error analysis are discussed, and further problems of plane wave scattering by rigid scatterers of different cross sections are presented [75, 76]. The numerical experiments show significant improvement of the efficiency when compared to the conventional BEM. The method is extended to include elastic wave problems [77] and three-dimensional Helmholtz problems [33, 78]. The convergence of the enriched FEM and BEM methods with plane wave basis is

studied further in reference [79] while in reference [80] different strategies are proposed to deal with irregular mesh grids and non-smooth scatterers.

Chandler-Wilde *et al.* [81] solved the problem of acoustic scattering by impedance boundary where the approximation space consists of polynomials multiplied by a plane wave. An analysis of the method shows that in order to keep the error constant with an increasing wave number it is enough to logarithmically increase the total number of degrees of freedom. The method was used to approximate the solution of a scattered wave by a convex polygon using a graded mesh with smaller elements closer to the polygon corners [82]. The numerical results prove the mentioned logarithmic relationship. This was improved further such that the error becomes independent of the wave number [83].

1.6 Overview

In this Chapter an introduction is given to wave problems in general and Helmholtz problems in particular. Some main contributions in solving these problems using numerical methods with different enrichment functions are highlighted. Other contributions may be found in the work of different authors cited in this Chapter. Further contributions will be mentioned in relevant parts of this thesis.

In Chapter 2, Helmholtz problems and the enriched finite element formulations will be presented. Two different types of enrichment are discussed. Then numerical tests are carried out to assess their performances. The accuracy and the conditioning of the method are discussed in Chapter 3 while some sources of error are studied in Chapter 4. In Chapter 5, an exact integration scheme is implemented to evaluate the elementary matrices of 3-noded elements. The considered numerical applications are extended to multiple scattering problems in Chapter 6. Then a variable number of enriching plane waves is considered for non-uniform meshing in Chapter 7. The PUFEM resulting linear system of equation is solved using an iterative approach in the standard and in the wavelet domains, in Chapter 8. Finally, problems involving singularities due to non-smooth scatterers, are presented and solved in Chapter 9.

Chapter 2

Locally enriched finite elements

In this work, the partition of unity method is adopted to enrich the finite element field using analytical solutions of the Helmholtz equation. As previously mentioned Melenk and Babuška [26, 27, 28] proposed two families of solutions, namely plane waves and Vekua functions, called in their work generalized harmonic polynomials, to enrich the solution space. However, different researchers used only plane waves while Vekua functions are limited to only a few examples (in the GFEM by Strouboulis *et al.* [48] and in the PUFEM by Laghrouche and Mohamed [37]). In recent work, Huttunen *et al.* [84, 85] enriched the UWVF with harmonic polynomials based on weighted Bessel functions. Also Barnett and Betcke [70] introduced fundamental solutions of the Helmholtz equation in the form of Hankel function series on the artificial outer boundary and used Fourier-Bessel functions at the corners of a non-convex domain. The latter enrichment was stated to capture singularities and ensure exponential convergence for an increasing number of basis functions.

In this Chapter, first, the weak form corresponding to the Helmholtz problem is introduced. Then it is shown how the solution space is enriched using either plane waves or Vekua functions. Results obtained by various authors for both enrichment types are briefly summarized. A mono scattering problem is then considered with the computational domain placed at different distances from the scatterer and for different wave numbers. Both enrichment techniques are assessed and compared.

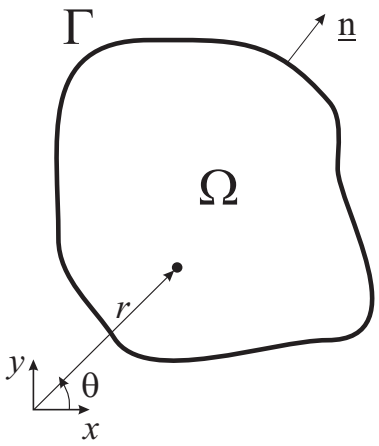

Figure 2.1: Schematic diagram of the problem.

2.1 Boundary value problem

The considered problem is governed by the homogeneous time harmonic Helmholtz equation which can be obtained starting form the wave equation

$$\frac{\partial^2 \Phi}{\partial t^2} = c^2 \nabla^2 \Phi \tag{2.1}$$

where c is the wave speed, which is assumed to be constant. Considering a harmonic time variation of $\Phi(x, y, t) = \phi(x, y)e^{-\mathrm{i}\omega t}$ leads to

$$(\nabla^2 + k^2)\phi = 0 \qquad \text{in} \quad \Omega \tag{2.2}$$

where x and y are the Cartesian coordinates, ∇^2 is the Laplace operator, i is the imaginary number ($\mathrm{i}^2 = -1$), $k = \frac{\omega}{c}$ is the wave number and ω is the circular frequency.

The domain Ω is chosen to be in the vicinity of the rigid scattering object. Figure (2.1) shows a schematic diagram of the considered domain. The analytical solution of the scattering problem is imposed on the domain boundary Γ through a Robin type boundary condition

$$\underline{\nabla \phi}.\underline{\mathrm{n}} + \mathrm{i}k\phi = g \qquad \text{on} \quad \Gamma \tag{2.3}$$

where $\underline{\nabla}$ is the gradient vector operator, g is the source term defined from the analytical solution and $\underline{\mathrm{n}}$ is the outward normal vector to Γ.

2.2 Weighted residual scheme

To solve the above boundary value problem the weighted residual finite element scheme is used. Equation (2.2) is multiplied by a weighting function W and integrated over the domain Ω

$$\int_{\Omega} W(\nabla^2\phi + k^2\phi)d\Omega = 0 \tag{2.4}$$

By applying the divergence theorem the Laplace operator ∇^2 is reduced to the gradient vector operator $\underline{\nabla}$ such that

$$\int_{\Omega}(-\underline{\nabla W}.\underline{\nabla\phi} + k^2W\phi)d\Omega + \int_{\Gamma} W\underline{\nabla\phi}.\underline{\mathrm{n}}\ d\Gamma = 0 \tag{2.5}$$

Introducing the boundary condition (2.3) gives

$$\int_{\Omega}(\underline{\nabla W}.\underline{\nabla\phi} - k^2W\phi)d\Omega + \mathrm{i}k\int_{\Gamma} W\phi d\Gamma = \int_{\Gamma} Wgd\Gamma \tag{2.6}$$

which is the weak form of the Helmholtz problem to be solved.

2.3 Finite element formulation

The domain of interest is meshed into n-noded finite elements. The potential within each finite element Ω_e is given by

$$\phi = \sum_{j=1}^{n} N_j\phi_j \tag{2.7}$$

where N_j with $j = 1, n$ are the shape functions and the nodal values ϕ_j are the unknowns of the problem. Due to the oscillatory nature of the solution and the low order of the polynomial shape functions, about 10 nodal points are usually required per wavelength to accurately approximate the solution.

Using the partition of unity technique the general solutions of the Helmholtz equation, namely plane waves or Vekua functions, are introduced in the shape functions. Hence instead of having only polynomial shape functions a combination of polynomial and oscillatory functions are used.

To implement this idea in the PUFEM, each nodal value ϕ_j is expressed as a combination of m oscillatory functions, ψ_l with $l = 1, 2, ..., m$, multiplied by amplitude

factors A_j^l which are now the new unknowns.

$$\phi_j = \sum_{l=1}^{m} \psi_l A_j^l \tag{2.8}$$

Let us consider first the Vekua function type enrichment.

2.3.1 Vekua function enrichment

Herrera and Sabina [86] proved that the system of functions

$$J_l(kr)e^{\mathrm{i}l\theta} \qquad \text{with} \quad l = 0, 1, ... \tag{2.9}$$

is a c-complete system in any bounded region and forms a basis for the two-dimensional Helmholtz equation (2.8) where r and θ are the polar coordinates. In other words, a combination of all cylindrical waves given in expression (2.9) constitutes a general solution of the Helmholtz equation.

These solutions are used to expand the nodal values of the potential into m functions multiplied by amplitude factors A_j^l. Thus (2.8) becomes

$$\phi_j = \sum_{l=0}^{m-1} J_l(kr)e^{\mathrm{i}l\theta} A_j^l \tag{2.10}$$

The potential over an element is written as

$$\phi = \sum_{j=1}^{n} \sum_{l=0}^{m-1} N_j J_l(kr)e^{\mathrm{i}l\theta} A_j^l \tag{2.11}$$

For notation convenience, the product of the polynomial shape functions N_j by the basis functions $J_l(kr)e^{\mathrm{i}l\theta}$ are considered to form new shape functions $P_{(j-1)m+l}$ so that

$$P_{(j-1)m+l} = N_j J_l(kr)e^{\mathrm{i}l\theta} \tag{2.12}$$

The global derivatives of the new shape functions are obtained from the global derivatives of the polynomial shape functions and the basis functions as follows

$$\begin{Bmatrix} \frac{\partial P_{(j-1)m+l}}{\partial x} \\ \frac{\partial P_{(j-1)m+l}}{\partial y} \end{Bmatrix} = \left[\begin{Bmatrix} \frac{\partial N_j}{\partial x} \\ \frac{\partial N_j}{\partial y} \end{Bmatrix} J_l(kr) + \frac{kN_j}{r} \begin{Bmatrix} x \\ y \end{Bmatrix} J_l'(kr) \right] e^{\mathrm{i}l\theta} + \left[\frac{\mathrm{i}l}{r^2} \begin{Bmatrix} -y \\ x \end{Bmatrix} J_l(kr) \right] e^{\mathrm{i}l\theta} \tag{2.13}$$

It should be mentioned that Vekua functions used in this work are centered globally at the coordinate system origin. Other implementations may center them at the element corners [48] or at the element centroids [84].

2.3.2 Plane wave enrichment

Using Jacobi-Anger expansion, it is possible to express a Bessel function as a combination of plane waves and *vice versa*. Therefore Vekua functions could also be expressed as a combination of plane waves and hence the system of plane waves

$$e^{\mathrm{i}k(x\cos\theta_l+y\sin\theta_l)} \qquad \text{with} \quad l=0,1,... \tag{2.14}$$

is a c-complete system too [30] where the angles θ_l are the directions of the plane waves taken in the range [0,2π]. Taking m plane waves as the basis in the equation (2.8) gives

$$\phi_j = \sum_{l=1}^{m} A_j^l e^{\mathrm{i}k(x\cos\theta_l+y\sin\theta_l)} \tag{2.15}$$

The potential over an element is then expressed by

$$\phi = \sum_{j=1}^{n}\sum_{l=1}^{m} N_j e^{\mathrm{i}k(x\cos\theta_l+y\sin\theta_l)} A_j^l \tag{2.16}$$

Again here the product of the polynomial shape functions N_j by the plane waves $e^{\mathrm{i}k(x\cos\theta_l+y\sin\theta_l)}$ is considered to produce the new shape functions

$$P_{(j-1)m+l} = N_j e^{\mathrm{i}k(x\cos\theta_l+y\sin\theta_l)} \tag{2.17}$$

The global derivatives of which are given by

$$\left\{ \begin{array}{c} \frac{\partial P_{(j-1)m+l}}{\partial x} \\ \frac{\partial P_{(j-1)m+l}}{\partial y} \end{array} \right\} = \left[\left\{ \begin{array}{c} \frac{\partial N_j}{\partial x} \\ \frac{\partial N_j}{\partial y} \end{array} \right\} + \mathrm{i}kN_j \left\{ \begin{array}{c} \cos\theta_l \\ \sin\theta_l \end{array} \right\} \right] e^{\mathrm{i}k(x\cos\theta_l+y\sin\theta_l)} \tag{2.18}$$

2.4 Element matrices and integration

Expression (2.6) leads to the following set of discrete equations of the form

$$[[K]-k^2[M]+\mathrm{i}k[C]]\{A\} = \{F\} \tag{2.19}$$

Where $\{A\}$ is the unknown vector. The element matrices are obtained by evaluating the following integrals

$$K_{qs}^e = \int_{\Omega_e} \underline{\nabla} W_q . \underline{\nabla} P_s \; d\Omega \tag{2.20}$$

$$M_{qs}^{e} = \int_{\Omega_e} W_q P_s \, d\Omega \tag{2.21}$$

$$C_{qs}^{e} = \int_{\Gamma_e} W_q P_s \, d\Gamma \tag{2.22}$$

$$F_{q}^{e} = \int_{\Gamma_e} W_q g \, d\Gamma \tag{2.23}$$

Where Γ_e and Ω_e are the element boundary and domain, respectively, while q and s are integers equal to $1, 2, \ldots, n \times m$.

The standard Galerkin finite element formulation is used, thus the weighting functions W_s are chosen to be the same as the shape functions P_s.

The assembling process of the elementary matrices obtained from (2.19) leads to the following global system of equations

$$\mathbf{A}\mathbf{x} = \mathbf{b} \tag{2.24}$$

For the solution of the system (2.24) the global matrix $\mathbf{A}$ is stored by columns. The stored entries start from the first non-zero value to the diagonal term of each column. The location of the first stored entry at each column is stored in a steering vector. The system is solved using a direct solver which factorizes the matrix $\mathbf{A}$ into the form $\mathbf{L}\mathbf{D}\mathbf{L}^{\top}$ where $\mathbf{L}$ is a lower triangular matrix with the diagonal values equal to 1, $\mathbf{L}^{\top}$ is the transpose matrix of $\mathbf{L}$ and $\mathbf{D}$ is a real diagonal matrix [87].

By solving the system (2.24), the amplitude vector $\mathbf{x}$ is obtained and hence the potential at any point of the computational domain is evaluated using the approximations (2.16) or (2.17).

The integrals (2.20) to (2.23) contain products of highly oscillatory functions. To capture all details inside the elements, a high order numerical integration scheme is necessary. Obviously, the number of integration points depends on the number of wavelengths contained within each element. The Gauss-Legendre integration scheme is used. It was found that around ten integration points per wavelength lead to good quality results.

2.5 Plane waves versus Vekua functions

Plane waves and Vekua functions were used by various authors and extensive numerical testing was carried out to show their efficiency. Here, first, the most important results are summarised, which basically state that both kind of enrichment lead to similar results in terms of accuracy and computational effort. Then a complementary numerical testing is carried out to show how the Vekua function enrichment could be more economical compared to the plane waves when dealing with a far field scattering problem.

2.5.1 Review of past important results

The enrichment of the finite element with oscillatory functions has proved to be an efficient method to reduce the required number of degrees of freedom per wavelength for solving Helmholtz problems. In references [33, 34] it was stated that, in the case of plane wave basis finite elements, a discretization level of around 2.5 variables per wavelength is sufficient to achieve satisfying results at high wave numbers. Consequently, in practical terms, these elements enable the compression of the information by a factor of 16 in two-dimensional problems and 64 in three-dimensional problems, over conventional finite elements. These estimations are obviously subject to variations depending on the problem. Using plane wave enrichment in the DEM reduced the required total number of degrees of freedom by up to 7 times in comparison to the FEM for a fixed accuracy and the resulting linear system has up to 10 times fewer non-zero entries [52].

Considering the same number of degrees of freedom in both enrichments, plane waves and Vekua functions, leads to practically the same accuracy [49]. However, the plane waves are more practical than Vekua functions as the integrals with plane waves can be evaluated analytically with straight edge elements, which is not possible with Vekua functions [65]. Plane waves, expressed with trigonometric functions, are evaluated numerically at lower cost compared to Vekua functions which are a combination of Bessel functions and trigonometric functions [49, 65]. Therefore the plane waves enrichment is usually the preferable choice.

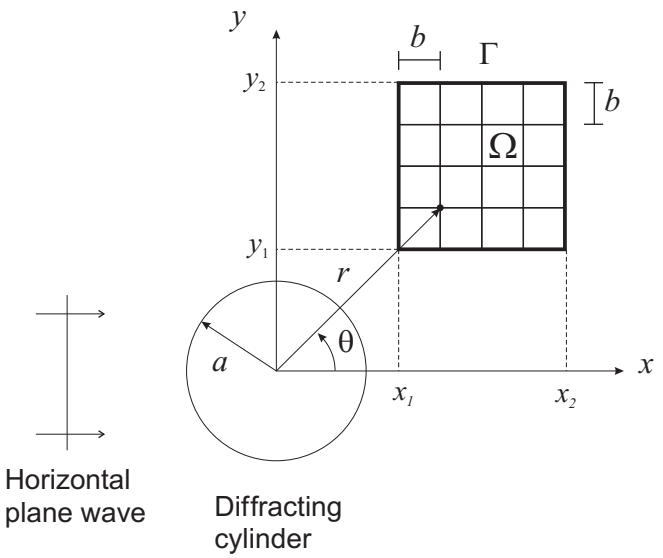

Figure 2.2: Computational domains of interest.

2.5.2 Complementary results

In this section the performance of the two types of enrichment is investigated in a mono scattering problem for different locations of the computational domain, with respect to the diffracting object, and for increasing wave number. A horizontal plane wave scattered by a rigid circular cylinder is considered. The analytical solution of this problem given by [88, 89] (see Appendix A)

$$\tilde{\phi_S} = -\sum_{n=0}^{\infty} \mathrm{i}^n \epsilon_n \frac{J_n'(ka)}{H_n'(ka)} H_n(kr)(\cos n\theta) \tag{2.25}$$

is imposed on the domain boundary Γ through the Robin boundary condition given in expression (2.3). The computational domain of interest Ω, shown in Figure 2.2, is taken such that $(x_1, y_1) \leq (x, y) \leq (x_2, y_2)$ and is meshed into 4×4 square bilinear finite elements of size b. For convenience, the radius a of the diffracting cylinder and the size b of the elements are chosen equal to a unit of length. All dimensions are normalised with respect to a. The location of the domain is defined by d where $d = x_1/a = y_1/a$.

The accuracy of the numerical results is measured by the relative L_2-norm error defined by

$$\varepsilon_2 = \frac{||\phi - \tilde{\phi_S}||_{L_2(\Omega)}}{||\tilde{\phi_S}||_{L_2(\Omega)}} \times 100\%, \tag{2.26}$$

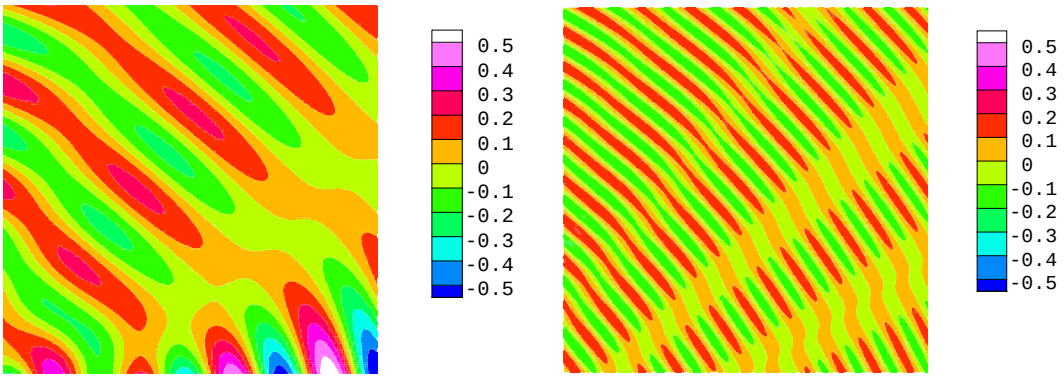

Figure 2.3: Real part of the diffracted potential in the computational domain Ω, (left) plane wave basis finite element model, $d = 1$, $ka = 2\pi$, $m = 16$, $\tau = 5$, $\varepsilon_2^P = 0.02\%$, (right) Vekua function basis finite element model, $d = 3$, $ka = 6\pi$, $m = 16$, $\tau = 1.7$, $\varepsilon_2^V = 0.6\%$.

where ϕ is the numerical solution of the diffracted potential. A parameter τ which indicates the number of degrees of freedom per wavelength (DOF/λ) is defined by

$$\tau = \lambda \times \sqrt{\frac{n_{tot} \times m}{\Omega_{area}}} \tag{2.27}$$

where n_{tot} is the total number of nodal points in the computational domain Ω while Ω_{area} is the domain area.

Figure 2.3 shows two examples of the numerical results. The contour plots represent the real part of the diffracted potential around the cylinder, inside the computational domain Ω. In the first example (left), the problem is solved for $ka = 2\pi$, which corresponds to a nodal spacing of one wavelength. The lower left corner of the computational domain Ω is placed such that $d = 1$. In this case, the domain Ω is considered to be close to the diffracting cylinder because in terms of the wavelength $d = \lambda/a$. A basis of 16 plane waves is used in the approximation of the diffracted potential, which leads to $\tau = 5$. For the evaluation of the element matrices 10 integration points are used in each spatial direction. The corresponding L_2 error shows very good agreement between the numerical and the analytical results; $\varepsilon_2^P = 0.02\%$.

In the second example (right), the wave number is increased to $ka = 6\pi$ which leads to a nodal spacing of 3λ. The computational domain is placed where $d = 3$. In this case, the domain Ω is considered to be in the far field in terms of the wavelength because $d = 9\lambda/a$ which is relatively far from the cylinder. The diffracted potential

is approximated using Vekua functions with $m = 16$. This time, because the wave number is higher, the number of degrees of freedom per wavelength is lower; $\tau = 1.7$. For the numerical integration of the element matrices, 40 Gauss points are used in each direction. The corresponding L_2 error shows the good accuracy of the results; $\varepsilon_2^V = 0.6\%$.

A set of numerical tests is carried out to compare the two types of enrichment. First, the considered wave number is $ka = 2\pi$ which gives a wavelength of $\lambda/a = 1$ and so a nodal spacing of one wavelength. At each node, the potential is either approximated by 16 Vekua functions with $l = 0, 1, ...15$ or 16 plane waves with the directions given by $\theta_l = 2\pi l/16$, $l = 1, 2, ...16$. This gives a global number of degrees of freedom per wavelength $\tau = 5$. Table 2.1 gives the values of the L_2 error in the case of the Vekua function approximation, ε_2^V, and in the case of the plane wave approximation, ε_2^P, when the computational domain is moved radially from the scatterer such that d varies from 1 to 7.

d	$\varepsilon_2^V[\%]$	$\varepsilon_2^P[\%]$
1	20	0.02
2	0.3	0.013
3	0.013	0.010
4	0.004	0.009
5	0.001	0.009
6	0.0009	0.009
7	0.0002	0.009

Table 2.1: L_2 error for different locations of the computational domain, $ka = 2\pi, m = 16, \tau = 5$.

Apart from the case of Vekua function approximation with $d = 1$ all other results show that both approximations lead to good accuracy. The results show when the computational domain is near the scatterer the plane wave approximation provides better accuracy ($\varepsilon_2^P < \varepsilon_2^V$ for $d \leq 3$). However, in the far field, Vekua function approximation leads to more accurate results ($\varepsilon_2^V < \varepsilon_2^P$ for $d > 3$). In this case, while the results obtained using Vekua functions improve in accuracy, the plane wave ap-

proximation results remain with a constant L_2 error of 0.009%. This may be due to the fact that near the scatterer, many interferences occur and the plane wave approximation is more capable of capturing them. In the far field, the diffracted potential behaves like a radial source and therefore Vekua functions are more adequate to approximate the wave potential.

In the next series of numerical experiments, the computational domain is kept at $d = 3$. The wave number is increased from $ka = \pi$ to 8π which leads to a wavelength decreasing from $\lambda/a = 2$ to 0.25. The number of approximating plane waves, or alternatively the number of approximating Vekua functions, is kept constant, $m = 16$. To evaluate the element matrices, the number n_{gauss} of integration points has to be increased to accommodate the oscillatory behaviour of the integrand within the multi-wavelength sized elements.

Table 3.6 gives the L_2 error of both approximations and the number τ of degrees of freedom per wavelength which is decreasing as the wave number increases. From the results, it is obvious that the plane waves perform better than Vekua functions only for $ka = \pi$. For $ka = 2\pi$, both models lead to similar accuracy. At higher wave numbers, $ka \geq 3\pi$, Vekua function approximation leads to a better accuracy and the corresponding L_2 error remains lower than 1%, up to $ka = 6\pi$, while the L_2 error corresponding to the approximating plane waves indicates that the numerical solution is deteriorating. For $ka \geq 7\pi$, the approximating Vekua functions still give results within engineering accuracy while those corresponding to the plane waves continue to deteriorate. In terms of DOF/λ, the plane wave basis finite element model performs well for $\tau > 2.5$ while Vekua function basis model continues to perform well below 2.5 DOF/λ.

To clarify the sensitivity of the proposed models to the frequency regime as well as to the location of the computational domain, the above studied example is reconsidered with the only difference being the location of the computational domain. This time, it is placed at $d = 11$ and all other parameters are kept unchanged. Results of Table 3.7 show again that the plane wave basis finite elements lead to engineering accuracy up to $\tau = 2.5$ and below this discretisation level the L_2 error increases rapidly. The Vekua function approximation model, however, provides very accurate results even

ka	τ	n_{gauss}	$\varepsilon_2^V[\%]$	$\varepsilon_2^P[\%]$
π	10	10	0.22	0.000009
2π	5	10	0.01	0.01
3π	3.3	20	0.1	0.8
4π	2.5	20	0.3	5
5π	2	30	0.5	41
6π	1.7	40	0.6	76
7π	1.4	40	1.7	95
8π	1.2	50	2.8	98

Table 2.2: L_2 error for increasing wave number ka, $d = 3$, $m = 16$.

at the highest considered wave number, $ka = 8\pi$, where the number of DOF/λ is very low, $\tau = 1.2$.

It is worth mentioning that when the wave number increases, the distance between the scatterer and the computational domain increases as well, in terms of the wavelength ($d/\lambda = 5.5$ for $ka = \pi$ and $d/\lambda = 44$ for $ka = 8\pi$). Therefore, for increasing wave number, the computational domain becomes a far field one. Hence, it is clearly shown that, in the far field, the approximating Vekua functions extend the efficiency of the proposed enriched finite element model to lead to accurate results with a parameter $\tau < 2.5$, unlike the plane wave basis finite element model.

ka	τ	n_{gauss}	$\varepsilon_2^V[\%]$	$\varepsilon_2^P[\%]$
π	10	10	0.000006	0.000008
2π	5	10	0.00005	0.008
3π	3.3	20	0.0003	0.5
4π	2.5	20	0.0013	3
5π	2	30	0.0016	14
6π	1.7	40	0.002	29
7π	1.4	40	0.04	59
8π	1.2	50	0.01	63

Table 2.3: L_2 error for increasing wave number ka, $d = 11$, $m = 16$.

More numerical experiments are carried out to further investigate this aspect. The computational domain is kept at $d = 11$ but, this time, to approximate the unknown potential, only 6 Vekua functions, or alternatively 6 plane waves, are attached at each nodal point of the mesh. This leads to a low number τ of degrees of freedom per wavelength, compared to the previous case (Table 3.7), for increasing wave number. Once again, it is obvious from the results of Table 2.4 that the Vekua function approximating model leads to accurate results. Its corresponding L_2 error remains below 1% even though the number τ of degrees of freedom per wavelength is very low; for the case of $ka = 8\pi$, $\tau = 0.8$ and $\varepsilon_2^V = 0.25\%$. However, the results corresponding to the plane wave approximating model shows that the numerical solution deteriorates quickly as the wave number increases.

ka	τ	n_{gauss}	$\varepsilon_2^V[\%]$	$\varepsilon_2^P[\%]$
π	6.1	10	0.003	0.5
2π	3.1	10	0.004	7.6
3π	2	20	0.001	82
4π	1.5	20	0.003	123
5π	1.2	30	0.05	115
6π	1	40	0.10	112
7π	0.9	40	0.16	107
8π	0.8	50	0.25	104

Table 2.4: L_2 error for increasing wave number ka, $d = 11$, $m = 6$.

2.6 Modified Vekua function basis

Vekua function is a product of a Bessel function $J_l(kr)$ and an oscillatory function $e^{\mathrm{i}l\theta}$. Increasing the number of Vekua basis functions means including higher order Bessel functions which might be of less efficiency than the lower order because the amplitude of Bessel functions decay exponentially as a higher order is considered.

When changing the order l of a Bessel function, the multiple of the angle θ in the trigonometric function is changed as well. To increase the effect of the lower orders,

one may vary the multiples of θ independently of the order of Bessel function. So that for each order a set of m_θ multiples are used. Instead of increasing the order which could be less effective, the first few orders are used each with a set of oscillatory functions.

A new variable m_θ is hence introduced as the number of θ multiples to be considered with each order. The modified Vekua basis then becomes

$$J_l(kr)e^{\mathrm{i}q\theta} \qquad \text{with} \quad l = 0, 1, \ldots m \quad \text{and} \quad q = 0, 1, \ldots m_\theta \tag{2.28}$$

The total number of the considered basis at each node is therefore $m \times m_\theta$. Thus expression (2.8) becomes

$$\phi_j = \sum_{l=1}^{m} \sum_{q=1}^{m_\theta} J_l(kr)e^{\mathrm{i}q\theta} A_j^{l,q} \tag{2.29}$$

Then the potential over an element could be rewritten as

$$\phi = \sum_{j=1}^{n} \sum_{l=1}^{m} \sum_{q=1}^{m_\theta} N_j J_l(kr)e^{\mathrm{i}q\theta} A_j^{l,q} \tag{2.30}$$

The new shape functions are

$$P_{(j-1)m+l+q} = N_j J_l(kr)e^{\mathrm{i}q\theta} \tag{2.31}$$

The global derivatives of these shape functions are

$$\begin{aligned} \begin{Bmatrix} \frac{\partial P_{(j-1)m+l}}{\partial x} \\ \frac{\partial P_{(j-1)m+l}}{\partial y} \end{Bmatrix} &= \left[\begin{Bmatrix} \frac{\partial N_j}{\partial x} \\ \frac{\partial N_j}{\partial y} \end{Bmatrix} J_l(kr) + \frac{kN_j}{r} \begin{Bmatrix} x \\ y \end{Bmatrix} J_l'(kr) \right] e^{\mathrm{i}q\theta} \\ &- \left[\frac{\mathrm{i}q}{r^2} \begin{Bmatrix} y \\ x \end{Bmatrix} J_l(kr) \right] e^{\mathrm{i}q\theta} \end{aligned} \tag{2.32}$$

To check the performance of these modified Vekua basis, they are compared to the original Vekua basis and the plane wave basis. The problem in section 2.5 is reconsidered. The domain is placed at $d = 1$ and then at $d = 3$. The number of functions attached to each node is increased by steps of four from 8 to 20. The resulting errors at each step are compared for the three cases: the plane waves, Vekua and the modified Vekua functions. In the modified Vekua basis the considered multiples of θ are $0, 1, 2$ and 3. Table (2.5) shows the L_2 error for the wavelength $\lambda = 1$ with an increased number of basis functions for $d = 1$ and $d = 3$.

τ	$\varepsilon_2^P[\%]$	$\varepsilon_2^V[\%]$	$\varepsilon_2^{Vm}[\%]$	$\varepsilon_2^P[\%]$	$\varepsilon_2^V[\%]$	$\varepsilon_2^{Vm}[\%]$
3.5	4.07	31	2.13	2.37	0.84	0.06
4.3	0.27	63	0.39	0.22	0.04	0.07
5	0.02	20	0.13	0.01	0.01	0.004
5.6	0.001	33	0.04	0.001	0.01	0.001
6.1	0.00014	8	0.03	0.00003	0.02	0.0008

Table 2.5: L_2 error for increasing m with $ka = 2\pi$, $m_\theta = 4$: (left) $d = 1$, (right) $d = 3$.

When increasing the number of plane waves the error improves one digit for every step, which is a consistent behaviour. For $d = 3$ (Table (2.5), (right)), with Vekua function the error is lower than with plane waves up to a certain number of basis functions and then the error stops to improve with Vekua basis. Thereafter the error with plane waves becomes lower. This may be due to the Bessel function exponential decay with an increasing order therefore the first few orders contribute more than the higher orders.

With the modified Vekua basis the error is not as good as with plane waves when $d = 1$. However, the modified Vekua basis performs significantly better than the original Vekua function basis. The error with the modified Vekua basis behaves in a similar way when $d = 3$ but here the error is lower than with the plane waves for the first three orders before the performance with plane waves becomes better.

2.7 Conclusion

In this Chapter, a Helmholtz problem with a Robin type boundary condition is dealt with using the PUFEM. Two types of enrichment are described, namely the Vekua functions and the plane waves. From past work, various authors stated that both enrichments lead to the same quality results. However, for their simplicity, plane waves are more popular. In this work, both enrichments are used to solve a scattering problem where the computational domain is located at different distances from the scatterer. The numerical tests show an improved efficiency with the Vekua basis when the computational domain is located far from the scatterer, in terms

of the wavelength. Different authors proposed a number of degrees of freedom per wavelength of about $\tau = 2.5$ to reach engineering accuracy with the plane wave enrichment [34, 33]. Here, it is shown that a discretization level of about 1.0 is enough to obtain a good quality results with Vekua functions when dealing with a far field domain.

Last, as the amplitude of Bessel function decays exponentially at higher orders, it is proposed to modify the Vekua functions such that more terms include lower orders of Bessel functions. It is found that the proposed modification leads to better results compared to the original Vekua basis.

In the following chapter, the plane wave enrichment is retained and both the convergence and the conditioning are thoroughly investigated with respect to various key parameters.

Chapter 3

Accuracy and conditioning

Although both type of enrichments, plane waves and Vekua functions, were reported by various authors to perform in a similar way [65, 49], the plane wave enrichment is more popular. One of the reasons lays in the fact that plane waves are easier to integrate than cylindrical waves. For example, in the UWVF and in the DEM where plane waves are used, the oscillatory integrals are evaluated exactly. In this work, the plane wave enrichment is also retained.

Many authors mentioned the need of around ten nodal points per wavelength to solve harmonic wave problems using polynomial based FEM. This was described as a *rule of thumb*. Ihlenburg [21] showed in his work that this rule is only a rough approximation and is not enough at high wave numbers. To keep the error under a certain level, not only hk should be kept small but also h^2k^3 [21, 22, 23, 90]. This is due to the pollution effect which is basically the difference between the problem true wave number and the numerical results wave number.

In comparison to the conventional finite element method, the enriched methods are less affected by the pollution effect, which could be counted as an extra advantage besides reducing the number of degrees of freedom required to solve a problem. This is shown in various convergence analyses of the enrichment methods [47, 49, 56]. This advantage is the consequence of including *a priori* knowledge of the solution, namely the wave number, in the approximation field.

In this Chapter, the convergence of the PUFEM is studied with respect to the element size h (h-convergence), the order p of the polynomial shape functions (p-convergence)

and the number m of enriching plane waves (q-convergence). The finite elements used for this study are 3-noded elements. For the p-convergence, 6-noded elements are also considered. The conditioning of the PUFEM is also quantified as a function of the various parameters mentioned above.

In references [47, 49], to study the convergence with respect to the number of enriching plane waves, the error is considered as a function of the number of enriching plane waves or the square root of the total number of degrees of freedom. Here, the q-convergence is investigated by considering the L_2 error against the number τ of degrees of freedom per wavelength. This is similar to what is proposed in reference [47] when taking the square root of the total number of degrees of freedom, but within the relative element size.

When solving Helmholtz problems with the PUFEM or with any other enrichment technique, each element may contain many wavelengths per nodal spacing. To measure the discretization level, the parameter τ giving the number of degrees of freedom per wavelength, was defined in references [34, 33]. It is given by expression (2.27). It was shown that a discretization level of about 2.5 of degrees of freedom per wavelength is sufficient to achieve results of engineering accuracy, i.e. about 1%, at high wave numbers [34, 33]. It was also mentioned that results can quickly deteriorate if τ is taken below 2.5.

The above defined τ gives an average value of the discretization level for the entire problem. In a uniform mesh, where all elements have the same size, and when a constant number of plane waves is used for the enrichment, τ is constant over all elements. However, with non-uniform mesh grids where element sizes vary throughout the problem domain and/or with variable number of enriching plane waves, the number of degrees of freedom per wavelength at an element level may differ from the average number of degrees of freedom given above. In practical terms, one can define a global (or average) discretization level given by expression (2.27) and a local discretization level given at every element. In the current Chapter, only uniform mesh grids with constant numbers of enriching plane waves are considered. Hence the global and the local discretization levels are identical.

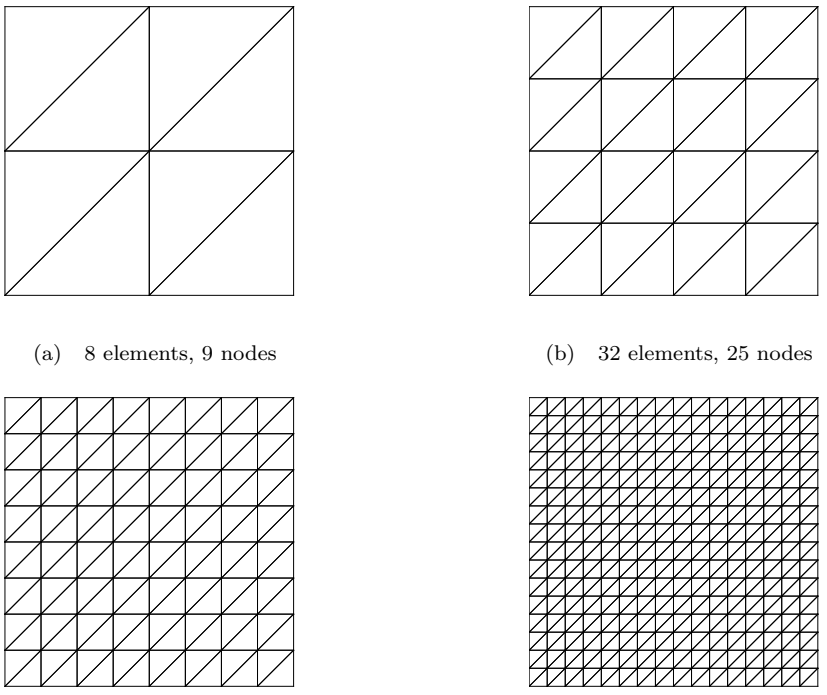

(a) 8 elements, 9 nodes

(b) 32 elements, 25 nodes

(c) 128 elements, 81 nodes

(d) 512 elements, 289 nodes

Figure 3.1: Various mesh grids with 3-noded elements.

m	h	h/λ	$totdof$	$totsys$	τ	$\varepsilon_2[\%]$	$\log(\kappa)$
8	$\frac{\sqrt{2}}{2}$	0.71	972	109998	7.79	0.0068	8.35
36	$\sqrt{2}$	1.41	900	172170	7.50	0.00074	19.60
100	$2\sqrt{2}$	2.83	900	285450	7.50	0.00006	19.14

Table 3.1: Relative size of the element with respect to the wavelength and its effect on the error and the conditioning, $ka = 2\pi$.

3.1 h-convergence

The scattering problem of Chapter 2 is reconsidered and all problem parameters are retained. The computational domain is placed close to the scatterer with its lower left corner $(x_1/a, y_1/a)$ located at $(1, 1)$. To solve this problem using the PUFEM the domain is meshed into right-angled triangular elements of size h, where h is the largest side length.

First the effect of the relative element size, expressed by the ratio h/λ, on the L_2 error and the conditioning is investigated, for a given wave number ka and a fixed number τ of degrees of freedom per wavelength. The number m of plane waves and

m	h	h/λ	$totdof$	$totsys$	τ	$\varepsilon_2[\%]$	$\log(\kappa)$
8	$\frac{\sqrt{2}}{2}$	1.41	972	109998	3.90	1.73	5.03
36	$\sqrt{2}$	2.83	900	172170	3.75	0.00016	15.56
100	$2\sqrt{2}$	5.66	900	285450	3.75	0.00013	19.55

Table 3.2: Relative size of the element with respect to the wavelength and its effect on the error and the conditioning, $ka = 4\pi$.

m	h	h/λ	$totdof$	$totsys$	τ	$\varepsilon_2[\%]$	$\log(\kappa)$
10	$\frac{\sqrt{2}}{2}$	2.12	1134	149625	2.81	12.31	4.98
48	$\sqrt{2}$	4.24	1200	305880	2.89	0.00015	16.60
134	$2\sqrt{2}$	8.49	1206	512349	2.89	0.00009	19.16

Table 3.3: Relative size of the element with respect to the wavelength and its effect on the error and the conditioning, $ka = 6\pi$.

m	h	h/λ	$totdof$	$totsys$	τ	$\varepsilon_2[\%]$	$\log(\kappa)$
10	$\frac{\sqrt{2}}{2}$	2.83	1134	149625	2.10	21.32	3.76
48	$\sqrt{2}$	5.66	1200	305880	2.17	0.57	12.17
134	$2\sqrt{2}$	11.31	1206	512349	2.17	0.00078	19.19

Table 3.4: Relative size of the element with respect to the wavelength and its effect on the error and the conditioning, $ka = 8\pi$.

the mesh size h are adjusted such that τ stays constant for this wave number. In fact, due to the integer nature of n and m, τ varies slightly.

Three mesh grids are considered for this study where the element sizes are $h/a = 2, 1$ and 0.5 (Figure 3.1; mesh grids (a), (b) and (c), respectively). Tables 3.1 to 3.4 illustrate the total number of degrees of freedom, $totdof$, the total number of storage locations, $totsys$, the L_2 error and the condition number $\log(\kappa)$, for different values of m so that $\tau \approx 7.5, 3.8, 2.9$ and 2.2 when $ka = 2\pi, 4\pi, 6\pi$ and 8π, respectively.

The results show different aspects of the PUFEM. First, the exponential decrease of the L_2 error is clear when both h/λ and m increase, while the total number of degrees of freedom remains approximately unchanged. However, the decrease in the error is accompanied by a significant increase of the total number of storage locations and of the condition number. Indeed, the behaviour of the conditioning is due to the increasing fill-in of the global matrix. Second, for a fixed τ, different levels of accuracy are achievable depending on the relative element size and the number of approximating plane waves. In order to get more accurate results, it is preferable to use coarse mesh grids and large numbers of plane waves but this leads to high condition numbers. Third, the matrix of the global linear system becomes ill-conditioned as m increases but still accurate solutions are obtained. This suggests that a preconditioning of the system and the use of an iterative solver may lead to accurate results and even lower computational cost for a fixed number τ. Finally, as the ratio h/λ and the wave number increase the number τ of degrees of freedom per wavelength required to obtain a certain error level decreases. This is clear, for example, for the error 0.0001% achieved with $\tau = 7.5$ at $h/\lambda = 1.41$ and $ka = 2\pi$, which could be achieved with $\tau = 2.17$ at $h/\lambda = 11.31$ and $ka = 8\pi$.

Next the effect of the element size on the error is studied. The previous problem is solved again using the mesh grids (b), (c) and (d) in Figure 3.1, which are now denoted by $h_1, h_{\frac{1}{2}}$ and $h_{\frac{1}{4}}$, respectively. Tables 3.5, 3.6 and 3.7 show the L_2 error for each mesh size when increasing m and for the wave numbers $ka = 2\pi$, 4π and 6π, respectively. It is observed, that h-refinement leads to an exponential decrease of the L_2 error with an estimated rate $\alpha \geq \frac{m}{2} - 1$. But continuing to increase m does not lead to a further decrease of the error. This is clear for example in the case of $m = 18$ at $ka = 2\pi$, $m = 22$ at $ka = 4\pi$ and $m = 30$ at $ka = 6\pi$. The stagnation of the

m	6	10	14	18
h_1	26.43	11.97	0.12	0.0086
$h_{\frac{1}{2}}$	2.16	0.054	0.0010	0.00007
$h_{\frac{1}{4}}$	0.14	0.0011	0.000017	0.000027
α	6.69	6.69	6.43	4.17

Table 3.5: L_2 error in [%] and average rate of convergence α for $ka = 2\pi$.

m	10	14	18	22
h_1	55.71	21.03	11.22	1.11
$h_{\frac{1}{2}}$	5.15	1.62	0.034	0.0017
$h_{\frac{1}{4}}$	0.068	0.0014	0.000052	0.000090
α	4.84	6.94	8.86	6.80

Table 3.6: L_2 error in [%] and average rate of convergence α for $ka = 4\pi$.

m	18	22	26	30
h_1	22.84	11.48	2.51	1.13
$h_{\frac{1}{2}}$	1.20	0.37	0.013	0.055
$h_{\frac{1}{4}}$	0.00090	0.00017	0.00024	0.0010
α	7.31	8.04	6.68	5.03

Table 3.7: L_2 error in [%] and average rate of convergence α for $ka = 6\pi$.

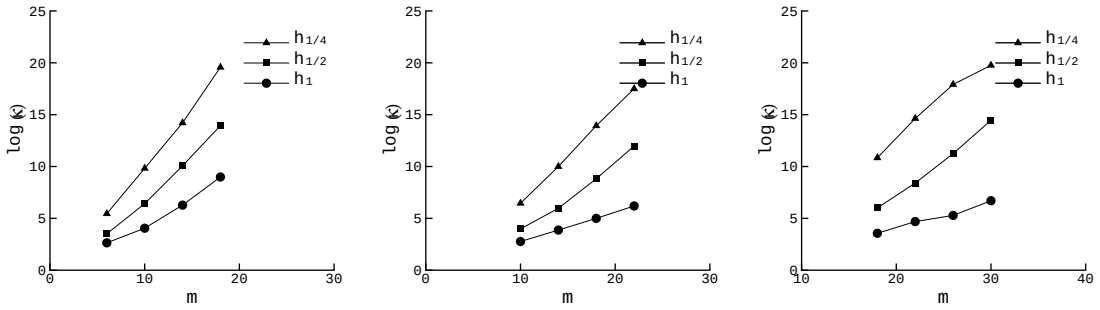

Figure 3.2: Condition number for (left) $ka = 2\pi$, (middle) $ka = 4\pi$ and (right) $ka = 6\pi$.

error level is due to the matrix of the final system which becomes ill-conditioned. To clarify this, the condition number κ of the linear system is investigated with respect to the 1-norm and values of $\log \kappa$ are summarised in Figure 3.2 for $ka = 2\pi$, 4π and 6π, and for increasing the number m of approximating plane waves.

It is clear that decreasing the mesh size h and/or increasing the number m of approximating plane waves leads to an increase of the condition number. In general, $\log \kappa$ is linearly increasing when the number m of plane waves increases. However, for fixed h and m, the conditioning decreases when the wave number increases. This makes the PUFEM suitable for the solution of high frequency problems and if the conditioning stays within acceptable limits, the effect of increasing m and decreasing the mesh size h leads to better accuracy of the results.

3.2 p-convergence

In order to study the effect of the order of the polynomial shape functions associated to the 3-noded linear ($Q3$) and the 6-noded quadratic ($Q6$) enriched finite elements on the L_2 error and the conditioning, the above problem is reconsidered again. For a given wave number ka and a number m of enriching plane waves, the corresponding $Q3$ and $Q6$ mesh grids are taken in such a way to get the same number τ of degrees of freedom per wavelength. The mesh grids (b) and (c) are reconsidered and denoted by $Q3h_1$ and $Q3h_{\frac{1}{2}}$. The corresponding mesh grids of 6-noded elements are respectively (e) and (f) displayed in Figure 3.3 and denoted by $Q6h_1$ and $Q6h_{\frac{1}{2}}$. The mesh grids $Q3h_1$ and $Q6h_1$, where the same number of nodes is maintained, have a similar number τ of degrees of freedom per wavelength for any number m of enriching plane

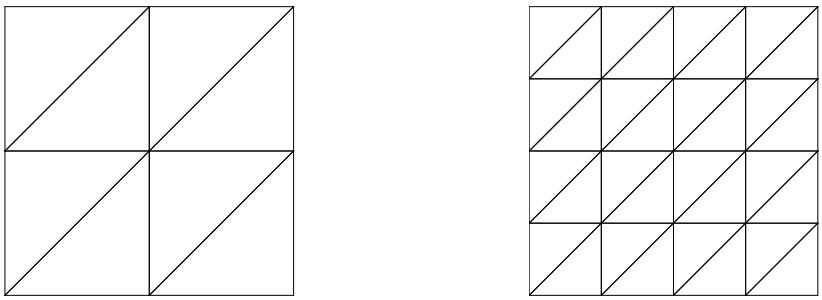

(e) 8 elements, 25 nodes (f) 32 elements, 81 nodes

Figure 3.3: Mesh grids with 6-noded elements.

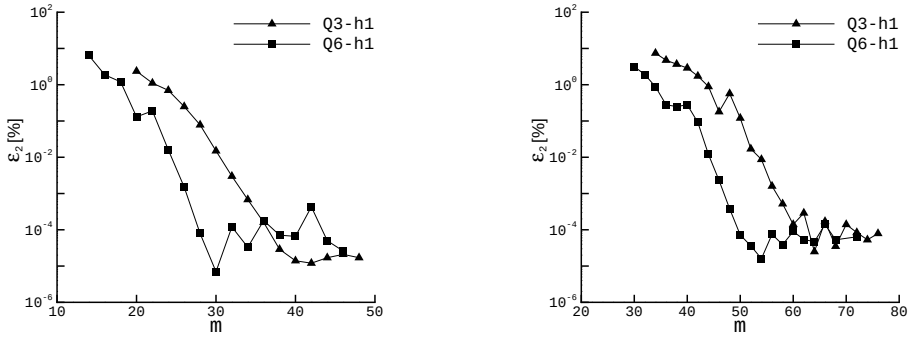

Figure 3.4: p-convergence, L_2 error plots for (left) $ka = 4\pi$ and (right) $ka = 8\pi$; h_1.

waves. However, the two mesh grids have different numbers of elements.

The four mesh grids are used for the solution of the problem for two values of the wave number $ka = 4\pi$ and 8π, with increasing the number m of plane waves. Figures 3.4 and 3.5 show the L_2 error and the condition number κ, respectively, as functions of m for the wave numbers $ka = 4\pi$ and 8π using the mesh grids $Q3h_1$ and $Q6h_1$. Similar results are presented on Figures 3.6 and 3.7 for the mesh grids $Q3h_{\frac{1}{2}}$ and $Q6h_{\frac{1}{2}}$.

The results show for both finite element schemes $Q3$ and $Q6$, for increasing values of

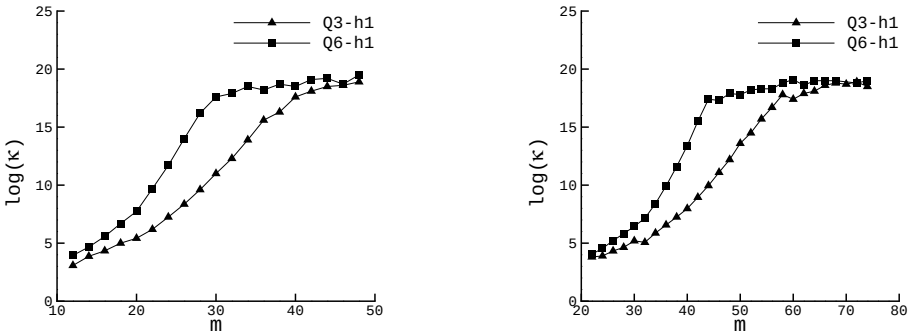

Figure 3.5: p-convergence, condition number κ plots for (left) $ka = 4\pi$ and (right) $ka = 8\pi$; h_1.

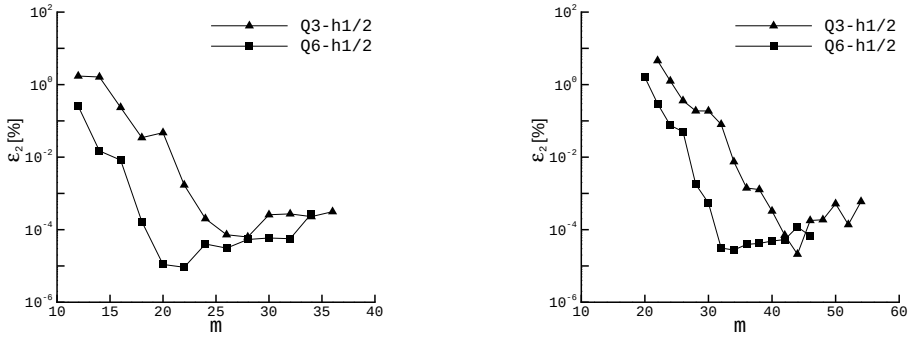

Figure 3.6: p-convergence, L_2 error plots for (left) $ka = 4\pi$ and (right) $ka = 8\pi$; $h_{\frac{1}{2}}$.

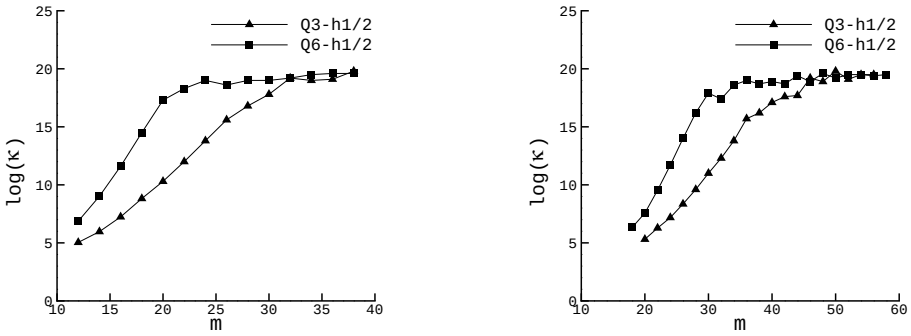

Figure 3.7: p-convergence, condition number κ plots for (left) $ka = 4\pi$ and (right) $ka = 8\pi$; $h_{\frac{1}{2}}$.

m, an exponential decrease of the L_2 error and an increase of the condition number. This happens up to a certain level at which the condition number may become rather large, as a consequence, the L_2 error oscillates rather than decrease (Figure 3.4, (left, $m > 30$) and (right, $m > 50$) and Figure 3.6 (left, $m > 20$) and (right, $m > 30$)). It is obvious, like in the conventional FE framework, the $Q6$ plane wave finite element scheme leads to more accurate results than the $Q3$ scheme, for the same discretization level, but the conditioning of the $Q3$ scheme is better.

This could be explained by noting that for the $Q6$ scheme, the elementary matrices are of the dimension $6m \times 6m$, which leads to a larger bandwidth of the global system matrix compared to the $Q3$ scheme for which the elementary matrices are of the dimension $3m \times 3m$. As a consequence, more storage locations are needed for the $Q6$ scheme in the global system matrix.

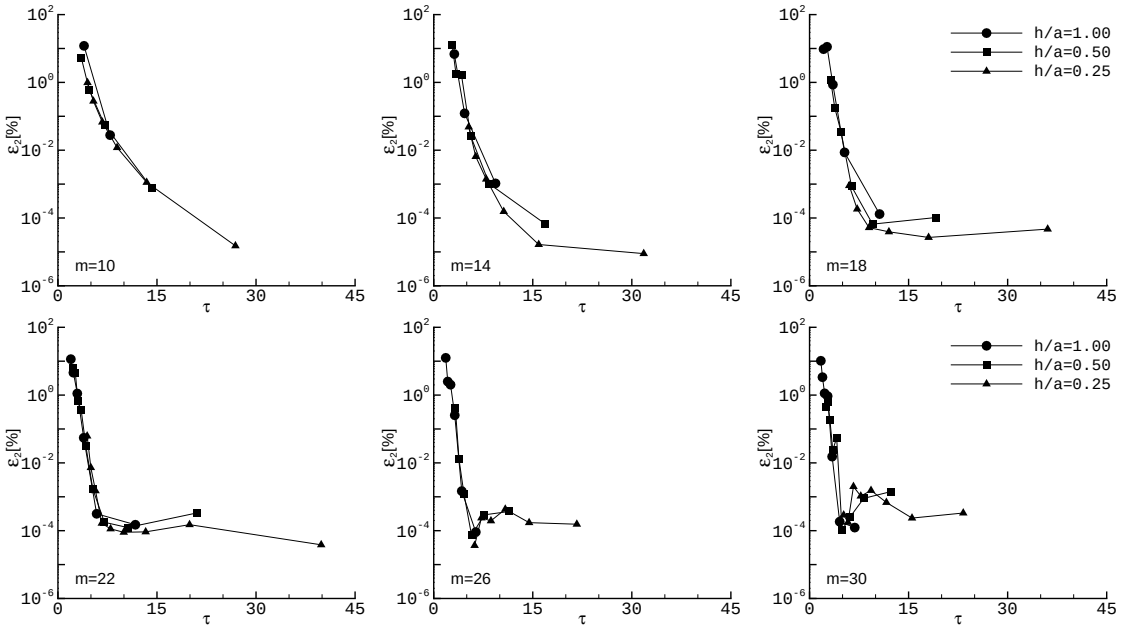

Figure 3.8: q-convergence, L_2 error plotted against τ.

3.3 q-convergence

The mesh (b) in Figure 3.1, denoted by h_1, is reconsidered with the solution space enriched by 10 plane waves. The problem is solved for an increasing wave number and the L_2 error is plotted against the number τ of degrees of freedom per wavelength in Figure 3.8 (the graph is noted by $m = 10$). Then the mesh grids (c) and (d) of Figure 3.1, denoted by $h_{\frac{1}{2}}$ and $h_{\frac{1}{4}}$, are used to solve the same problem with $m = 10$ again for an increasing wave number. The L_2 error is again plotted in Figure 3.8 on the same graph. Although the number of plane waves is kept constant $m = 10$ for all considered wave numbers, τ increases due to the increase of the number of elements. The resulting three lines of convergence are referred to with $h/a = 1, 0.5$ and 0.25 on the graph.

In the same way, convergence lines are plotted for different numbers of plane waves $m = 14, 18, 22, 26$ and 30. The L_2 errors corresponding to each number of plane waves are reported in Figure 3.8 on a separate graph as a function of τ.

In all cases shown in Figure 3.8, an error of less than 1% is obtained for values of τ much smaller than 10. In spite of using different wave numbers and different mesh grids, the errors corresponding to each number of plane waves are located on the same line of convergence. This may suggest for each number of enriching plane waves a

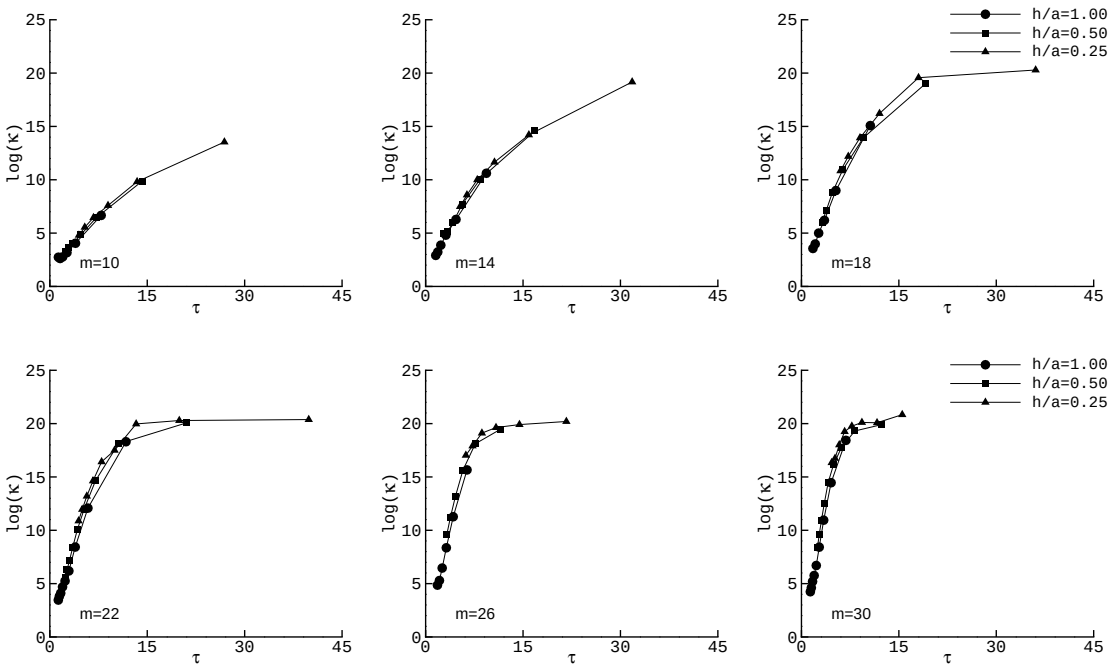

Figure 3.9: q-convergence, condition number κ plotted against τ.

certain pattern of convergence that is repeated independently of the mesh size or the wave number. As a higher number of plane waves is considered the slope of the convergence line becomes steeper. In other words the convergence rate increases as the number of plane waves increases, which is in agreement with previous conclusions [35, 91]. The results also show an improvement of the error with an increasing τ until a certain level ($\varepsilon_2 \approx 0.00001\%$) thereafter the error ceases to improve. This is due to the conditioning problem mentioned earlier.

The graphs in Figure 3.9 show the condition number corresponding to the L_2 error values in Figure 3.8. For each number of plane waves it is shown that the condition number keeps increasing with τ until it reaches a certain value and then remains practically unchanged.

For the highest considered number of plane waves ($m = 30$) the condition number is relatively low at a low τ. Therefore one may conclude that with high numbers of plane waves it is still possible to get a relatively low condition number by decreasing τ through the use of large elements. The reduction of τ is possible up to a certain limit thereafter a smaller value might be insufficient to obtain an acceptable error. However, the results obtained in this work suggest that it is possible to consider a quite low value of τ and still obtain good quality results.

3.4 Conclusion

In this Chapter, the convergence of the PUFEM is studied with respect to the element size h, the order p of the polynomial shape functions and the number m of plane waves. To get the most of the PUFEM potential, large elements compared to the wavelength with high numbers of enriching plane waves are suitable. If the same number of degrees of freedom per wavelength is considered with smaller elements and fewer plane waves the PUFEM solution deteriorates.

The large elements with high numbers of enriching plane waves have the advantage of a better quality results. However, such elements are less accurate in describing curved geometries. This may induce errors in the method. In the following chapter, different sources of errors affecting the efficiency of the PUFEM are analysed. When possible, each source of error is considered separately to avoid the influence of other parameters.

Chapter 4

Some sources of error in the PUFEM

In this chapter, various sources of errors affecting the accuracy of the PUFEM are identified and analysed. Anticipating the influence of these errors aims at minimizing their effect on the numerical solution or, when possible, eliminating their contribution to the global error. First, the effect of using uniform and non-uniform mesh grids and the effect of conjugated and unconjugated weighting are investigated. Then, the error due to geometry interpolation is considered and compared to the case where the geometry is exactly described. Last, the effect of the radiation boundary condition is also analysed.

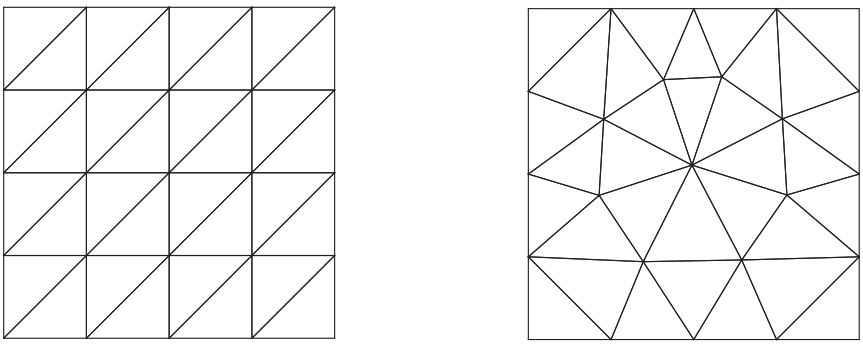

(d) 32 elements, 25 nodes (e) 32 elements, 25 nodes

Figure 4.1: Uniform and non-uniform mesh grids.

4.1 Uniform versus non-uniform mesh grids

Usually, in problems with simple geometry, structured mesh grids with uniformly distributed nodal points are used. Such mesh grids are easily obtained and the value of τ, number of degrees of freedom per wavelength, is constant all over the computational domain. In many problems of practical importance, however, the domains of interest are of complicated geometries and hence non-structured mesh grids are required. In such meshes the elements are of various sizes and the distribution of the nodal points is not uniform. Moreover, the number of degrees of freedom per wavelength generally varies within the domain.

	$\varepsilon_2[\%]$		$\log(\kappa)$	
m	uniform	non-uniform	uniform	non-uniform
10	11.97	2.61	4.05	3.92
14	0.12	0.31	6.28	6.42
18	0.0086	0.0071	8.99	8.88
22	0.00032	0.00029	12.08	12.08
26	0.000091	0.000061	18.93	15.69
30	0.00012	0.00012	18.43	18.50

Table 4.1: Uniform versus non-uniform meshing, L_2 error and condition number, $ka = 2\pi$.

The mono-scattering problem dealt with in Chapter 3 is reconsidered here with the triangular mesh grid h_1 shown in Figure 3.1, mesh (b). To consider a non-structured mesh, the distribution of the nodal points is modified such that the domain is filled with triangular elements of various sizes. In general, the mesh size h is kept practically constant within the mesh grid, h being the largest element size in the domain. The two mesh grids are shown in Figure 4.1.

The problem is solved for the wave number $ka = 2\pi$ where the number m of approximating plane waves is increased from 10 to 30. The L_2 error and the condition number are reported in Table 4.1. The results show when a sufficient number of plane waves is used, both meshes lead to good accuracy results. However, with the non-uniform mesh the error is slightly smaller. This is due to the fact that most of

the elements in the non-uniform mesh are practically equilateral triangles, or very close while those in the structured mesh grid are all isosceles with a right internal angle. Therefore, the elements of the non-uniform mesh grid are of better quality, this may justify the good quality results obtained in this example.

4.2 Conjugated versus unconjugated formulation

The plane wave enrichment used in the PUFEM is also encountered in other methods as well, such as the DEM [52] and the UWVF [64]. Some of these methods used the complex conjugate of the shape functions for the weighting functions while other methods followed a standard Galerkin formulation where the shape functions are used as the weighting functions. This choice of the weighting functions is qualified here as conjugated or unconjugated weighting. Examples of a conjugated formulation could be found in references [26, 64] and of an unconjugated formulation in references [30, 52]. It is worth mentioning that both conjugated and unconjugated formulations were used in the infinite element method (IEM) to solve Helmholtz problems and the two formulations were compared in reference [92].

All previous calculations performed in this thesis were based on a Galerkin weighting i.e. $W_{(j-1)m+l} = P_{(j-1)m+l} = N_j e^{\mathrm{i}k\xi_l \cdot \mathbf{r}}$, which corresponds to the unconjugated weighting. The resulting formulation

$$\int_\Omega (\underline{\nabla W}.\underline{\nabla \phi} - k^2 W\phi) d\Omega + \mathrm{i}k \int_\Gamma W\phi d\Gamma = \int_\Gamma W g d\Gamma \tag{4.1}$$

leads to a symmetric linear system of equations. Whereas the use of a conjugated formulation, such that $W_{(j-1)m+l} = \bar{P}_{(j-1)m+l} = N_j e^{-\mathrm{i}k\xi_l \cdot \mathbf{r}}$, leads to sum of a Hermitian matrix obtained from the domain integral and a skew Hermitian matrix obtained from the boundary integral.

The previous problem is reconsidered with both conjugated and unconjugated formulations where the mesh grid h_1 of Figure 3.1 is used for the solution. The considered wave numbers are $ka = 2\pi$, 4π and 6π. The L_2 error for each wave number and for increasing number m of enriching plane waves are reported in Figure 4.2 for both formulations.

It can be seen from the error plots that, in general, for an odd number m of plane

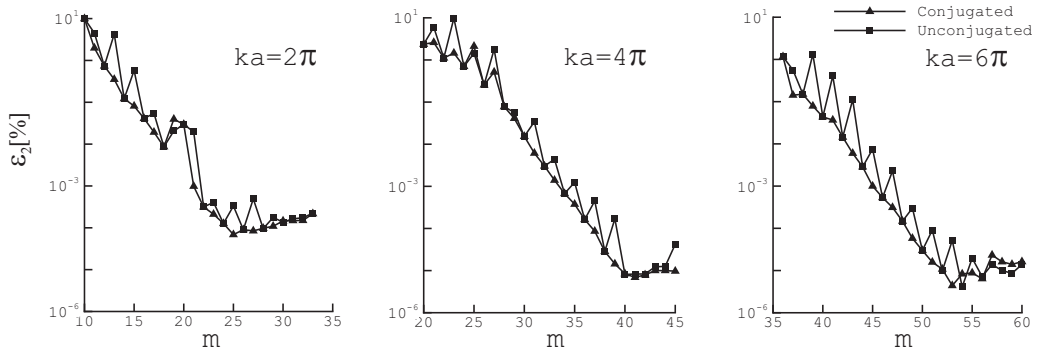

Figure 4.2: Conjugated versus unconjugated formulations, L_2 error plots.

waves, the conjugated formulation performs better than the unconjugated one. When m is even, however, both formulations lead to similar L_2 errors. The error decreases as m increases up to a certain value, $m = 25$ for $ka = 2\pi$, $m = 40$ for $ka = 4\pi$, and $m = 53$ for $ka = 6\pi$. Continuing to increase m, for a fixed wave number, does not affect the L_2 error, which remains practically unchanged because of the conditioning as shown in Chapter 3.

Regarding the two formulations, the conjugated and the unconjugated, it is shown that they are equivalent for an even number m of approximating plane waves, when their corresponding directions are evenly distributed in the plane. Let us consider a case in which $m = 4$ with the directions $\frac{2\pi l}{4}$ where $l = 0, 1, 2$ and 3. The plane waves corresponding to these directions are $e^{-\mathrm{i}kx}$, $e^{-\mathrm{i}ky}$, $e^{\mathrm{i}kx}$ and $e^{\mathrm{i}ky}$. For the unconjugated formulation a block of the equivalent element 'mass' matrix $M_{unconj} = \int_\Omega W\phi \; d\Omega$ is given by

$$M_{unconj} = \int_\Omega \begin{bmatrix} e^{-\mathrm{i}2kx} & e^{-\mathrm{i}k(x+y)} & 1 & e^{-\mathrm{i}k(x-y)} \\ e^{-\mathrm{i}k(x+y)} & e^{-\mathrm{i}2ky} & e^{\mathrm{i}k(x-y)} & 1 \\ 1 & e^{\mathrm{i}k(x-y)} & e^{\mathrm{i}2kx} & e^{\mathrm{i}k(x+y)} \\ e^{-\mathrm{i}k(x-y)} & 1 & e^{\mathrm{i}k(x+y)} & e^{\mathrm{i}2ky} \end{bmatrix} Q \; d\Omega \qquad (4.2)$$

where Q represents the contribution of the polynomial parts to the integrand. It is obvious that the resulting M_{unconj} is symmetric and with a few real elements, equal to 1, scattered in the matrix.

Now, let us consider the conjugated formulation, in which the complex conjugates of the 4 considered plane waves are used as weighting functions. In this case, the

'mass' matrix M_{conj} is given by

$$M_{conj} = \int_{\Omega} \begin{bmatrix} 1 & e^{\mathrm{i}k(x-y)} & e^{\mathrm{i}2kx} & e^{\mathrm{i}k(x+y)} \\ e^{-\mathrm{i}k(x-y)} & 1 & e^{\mathrm{i}k(x+y)} & e^{\mathrm{i}2ky} \\ e^{-\mathrm{i}2kx} & e^{-\mathrm{i}k(x+y)} & 1 & e^{-\mathrm{i}k(x-y)} \\ e^{-\mathrm{i}k(x+y)} & e^{-\mathrm{i}2ky} & e^{\mathrm{i}k(x-y)} & 1 \end{bmatrix} Q \; d\Omega \tag{4.3}$$

which is a Hermitian matrix with real diagonal elements. In fact, this matrix could be obtained from the unconjugated version by carrying out permutations of the first and second rows/columns with the third and fourth rows/columns, respectively. In the same way one can see the equivalence of the element 'stiffness' matrix $\int_{\Omega} \underline{\nabla W}.\underline{\nabla \phi} \; d\Omega$ with both formulations.

The last part of the weak form to be included in the system matrix is resulting from the line integral $\mathrm{i}k \int_{\Gamma} W\phi \; d\Gamma$. This part is symmetric with the unconjugated formulation while, unlike the first two parts, it is skew Hermitian with the conjugated formulation because it is multiplied by the imaginary number i. However, domain integrals of the weak form (4.1) constitute the majority of the system matrix while the influence of the line integral part is limited to the elements on the boundary. This may explain why the two formulations are equivalent for even numbers of approximating plane waves, evenly distributed in the plane.

On the other hand, for odd numbers m of plane waves or even numbers of plane waves not evenly distributed, the two formulations are not equivalent. This is shown for an example with an odd number of plane waves. Let us Consider the case of 3 plane waves with the directions $\frac{l\pi}{3}$ with $l = 0, 1$ and 2. The plane waves corresponding to these directions are $e^{\mathrm{i}kx}$, $e^{\mathrm{i}k(-\frac{x}{2}+\frac{\sqrt{3}}{2}y))}$ and $e^{\mathrm{i}k(-\frac{x}{2}-\frac{\sqrt{3}}{2}y)}$. The 'mass' matrices are given by

$$M_{unconj} = \int_{\Omega} \begin{bmatrix} e^{2ikx} & e^{\frac{1}{2}\mathrm{i}k\left(x+\sqrt{3}y\right)} & e^{\frac{1}{2}\mathrm{i}k\left(x-\sqrt{3}y\right)} \\ e^{\frac{1}{2}\mathrm{i}k\left(x+\sqrt{3}y\right)} & e^{-\mathrm{i}k\left(x-\sqrt{3}y\right)} & e^{-\mathrm{i}kx} \\ e^{\frac{1}{2}\mathrm{i}k\left(x-\sqrt{3}y\right)} & e^{-\mathrm{i}kx} & e^{-\mathrm{i}k\left(x+\sqrt{3}y\right)} \end{bmatrix} \tag{4.4}$$

and

$$M_{conj} = \int_{\Omega} \begin{bmatrix} 1 & e^{-\frac{1}{2}\mathrm{i}k\left(3x-\sqrt{3}y\right)} & e^{-\frac{1}{2}\mathrm{i}k\left(3x+\sqrt{3}y\right)} \\ e^{\frac{1}{2}\mathrm{i}k\left(3x-\sqrt{3}y\right)} & 1 & e^{-\mathrm{i}k\sqrt{3}y} \\ e^{\frac{1}{2}\mathrm{i}k\left(3x+\sqrt{3}y\right)} & e^{\mathrm{i}k\sqrt{3}y} & 1 \end{bmatrix} \tag{4.5}$$

Again the resulting matrix is symmetric for the unconjugated formulation and Hermitian for the conjugated formulation. But it is clear that the two matrices lead to

two different linear systems.

For the rest of the thesis, the unconjugated formulation is retained and even numbers of plane waves evenly spaced in the plane are used. The resulting system matrix is therefore symmetric.

4.3 Effect of geometry description

Within the FEM, it is generally well accepted to describe the element geometry using linear or quadratic interpolations. Even when curved domains are dealt with, the mentioned interpolations provide a very good approximation of the geometry provided that sufficiently fine mesh grids are used. In the PUFEM, however, where multi-wavelength sized elements are involved, the geometry becomes an issue and consequently any inaccuracy in the geometry description will have a significant effect on the quality of the numerical results.

To show this, a scattering problem is investigated in which an annular domain enclosing the rigid scatterer is considered (Figure 4.3). First, the difference between the interpolated geometry and the exact geometry, circular in this case, is quantified. Then the influence of the interpolated geometry on the numerical solution is analysed by comparing the results obtained using both geometry descriptions; interpolated and exact.

4.3.1 Interpolated versus exact geometry

An element edge on the outer boundary Γ_2 (Figure 4.3) is considered for different values of the radius and different lengths of the circular arc. The arc is described using a quadratic interpolation such that

$$x = \sum_{j=1}^{3} N_j(\eta) x_j \quad \text{and} \quad y = \sum_{j=1}^{3} N_j(\eta) y_j \tag{4.6}$$

with the local coordinate η varying between -1 and 1 and N_j being the Lagrange interpolation functions. The relative error on the interpolated radius R^{in} is measured by computing

$$\varepsilon_1 = \frac{\mid R^{in} - R^{ex} \mid}{R^{ex}} \times 100[\%] \tag{4.7}$$

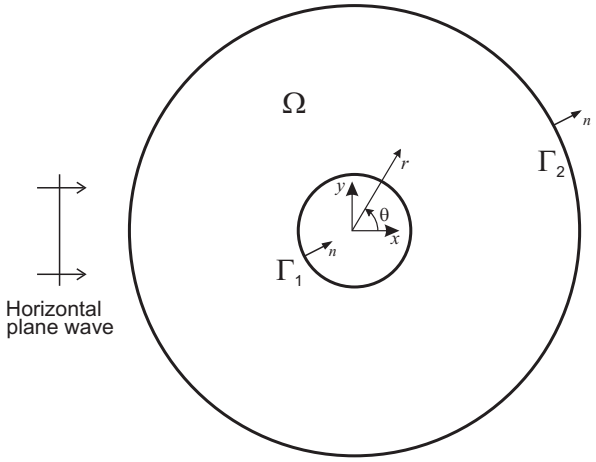

Figure 4.3: Schematic diagram of the problem domain.

where R^{ex} is the exact value of the radius and $R^{in} = \sqrt{x^2 + y^2}$.

Three values of the outer radius are considered $R^{ex}/a = 2, 4$ and 8. The inner radius is kept unchanged at $r/a = 1$. The domain is meshed into 4, 8 and 16 elements of the same size.

Figure 4.4 shows the mesh grids with 4 elements for the different outer radii, $R^{ex}/a = 2, 4$ and 8, and the corresponding plots of ε_1 against the local coordinate η. Similar plots are shown in Figures 4.5 and 4.6 when 8 and 16 elements are used in the mesh grids, respectively.

It is obvious that R^{in} is exact at the nodal points where $\eta = -1, 0$ and 1. Between the nodes, however, the value of R^{in} varies depending on the extent R^{ex} of the outer boundary and the angle θ subtended by the element. For a constant angle θ, the relative error ε_1 remains unchanged as R^{ex}/a increases from 2 to 8, which implies that the difference between R^{in} and R^{ex} gets larger with R^{ex}. For example an error of 1.08% with $R/a = 2$ leads to a difference $\mid R^{in} - R^{ex} \mid /a = 0.022$ while the same error with $R/a = 8$ leads to a difference of 0.086 which is 4 times larger than the previous difference.

For a constant R^{ex} and increasing the subtended angle θ, the relative error ε_1 increases, from 0.005% for $\theta = \pi/16$ to more than 1% for $\theta = \pi/2$. These results are obtained with quadratic interpolation and hence using linear interpolation will lead to even higher differences between R^{in} and R^{ex}.

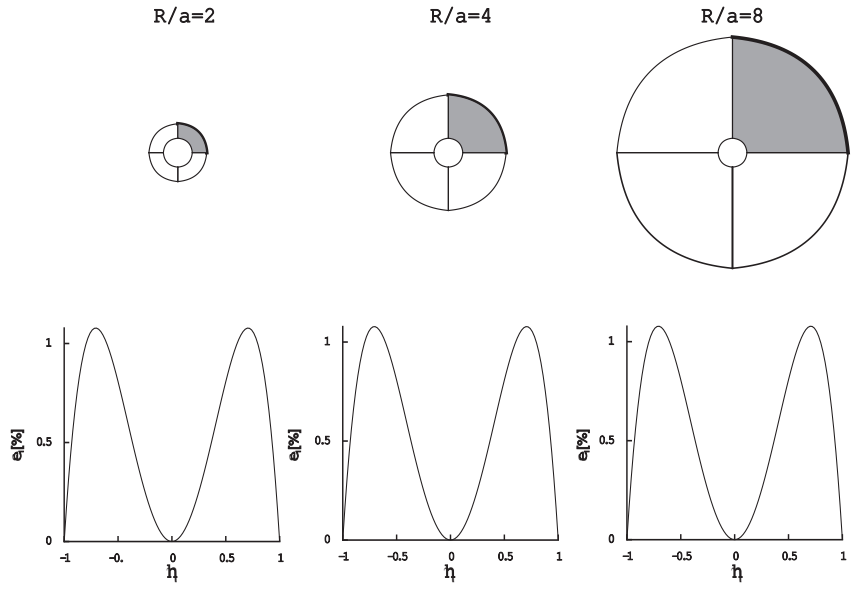

Figure 4.4: Relative error of R^{in} with respect to R^{ex} along the highlighted edge, $\theta = \pi/2$.

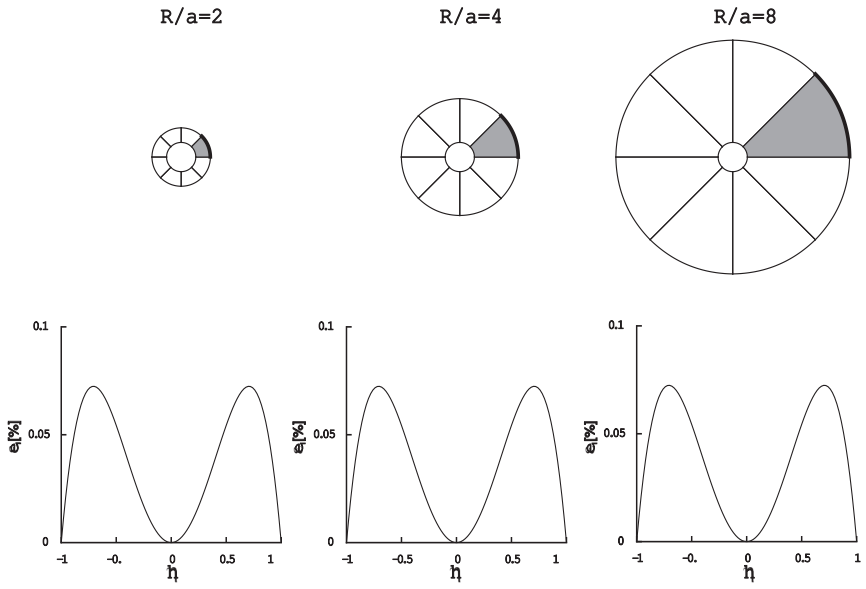

Figure 4.5: Relative error of R^{in} with respect to R^{ex} along the highlighted edge, $\theta = \pi/4$.

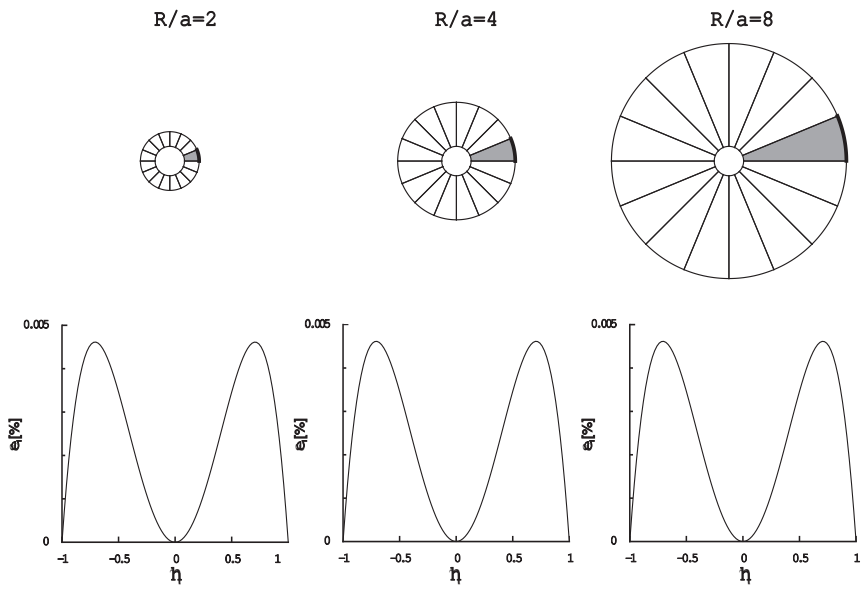

Figure 4.6: Relative error of R^{in} with respect to R^{ex} along the highlighted edge, $\theta = \pi/8$.

4.3.2 Effect of geometry description on the PUFEM

The previous subsection shows the difference between the approximated and the exact geometry of a circular arc on the outer boundary of the considered scattering problem. Here, it is intended to analyse the effect of the interpolated geometry on the PUFEM results, especially when the elements span many wavelengths. To do this, the exact geometry description is used as a reference.

The outer boundary of the scattering problem domain shown in Figure 4.3 is a circle. It is possible to describe this geometry exactly with linear shape functions in a polar coordinate system (ρ, θ). This idea is presented here with a 4-noded element where the implementation with $Q9$ elements is similar. Considering the element highlighted in Figure 4.7

$$r = \frac{1}{2}(1-\xi)r_1 + \frac{1}{2}(1+\xi)r_2 \tag{4.8}$$

$$\theta = \frac{1}{2}(1-\eta)\theta_1 + \frac{1}{2}(1+\eta)\theta_2 \tag{4.9}$$

The derivatives of r and θ with respect to ξ and η are

$$\frac{\partial r}{\xi} = \frac{r_2 - r_1}{2} \tag{4.10}$$

$$\frac{\partial r}{\eta} = 0 \tag{4.11}$$

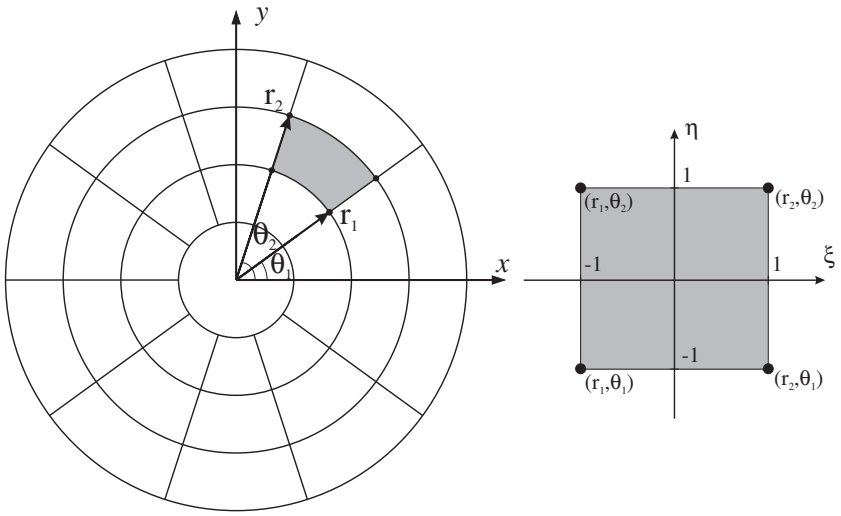

Figure 4.7: Geometry interpolated from polar coordinates.

τ	$\varepsilon_1[\%]$	$\varepsilon_2^e[\%]$	$\varepsilon_2^i[\%]$
2.93	1.08	1.55	2.25
4.15	0.08	0.15	0.11
6.56	0.015	0.0018	0.022
7.57	0.005	0.00055	0.0066

Table 4.2: Errors obtained with different $Q9$ mesh grids, $ka = 4\pi, m = 36$.

$$\frac{\partial \theta}{\xi} = 0 \tag{4.12}$$

$$\frac{\partial \theta}{\eta} = \frac{\theta_2 - \theta_1}{2} \tag{4.13}$$

Because $x = r\cos\theta$ and $y = r\sin\theta$, the Jacobian matrix may be written as

$$[J] = \begin{bmatrix} \frac{r_2 - r_1}{2}\cos\theta & \frac{r_2 - r_1}{2}\sin\theta \\ -r\frac{\theta_2 - \theta_1}{2}\sin\theta & r\frac{\theta_2 - \theta_1}{2}\cos\theta \end{bmatrix} \tag{4.14}$$

the rest of the computations are carried out in the same way as before.

The considered problem has a weak form which is similar to the expression (2.6), however, the analytical solution is applied on Γ_1 and Γ_2 rather than only on Γ in expression (2.6)

$$\int_\Omega (\underline{\nabla W} \cdot \underline{\nabla \phi} - k^2 W\phi)\, d\Omega + \mathrm{i}k \int_{\Gamma_1} W\phi\, d\Gamma + \mathrm{i}k \int_{\Gamma_2} W\phi\, d\Gamma = \int_{\Gamma_1} Wg\, d\Gamma + \int_{\Gamma_2} Wg\, d\Gamma \tag{4.15}$$

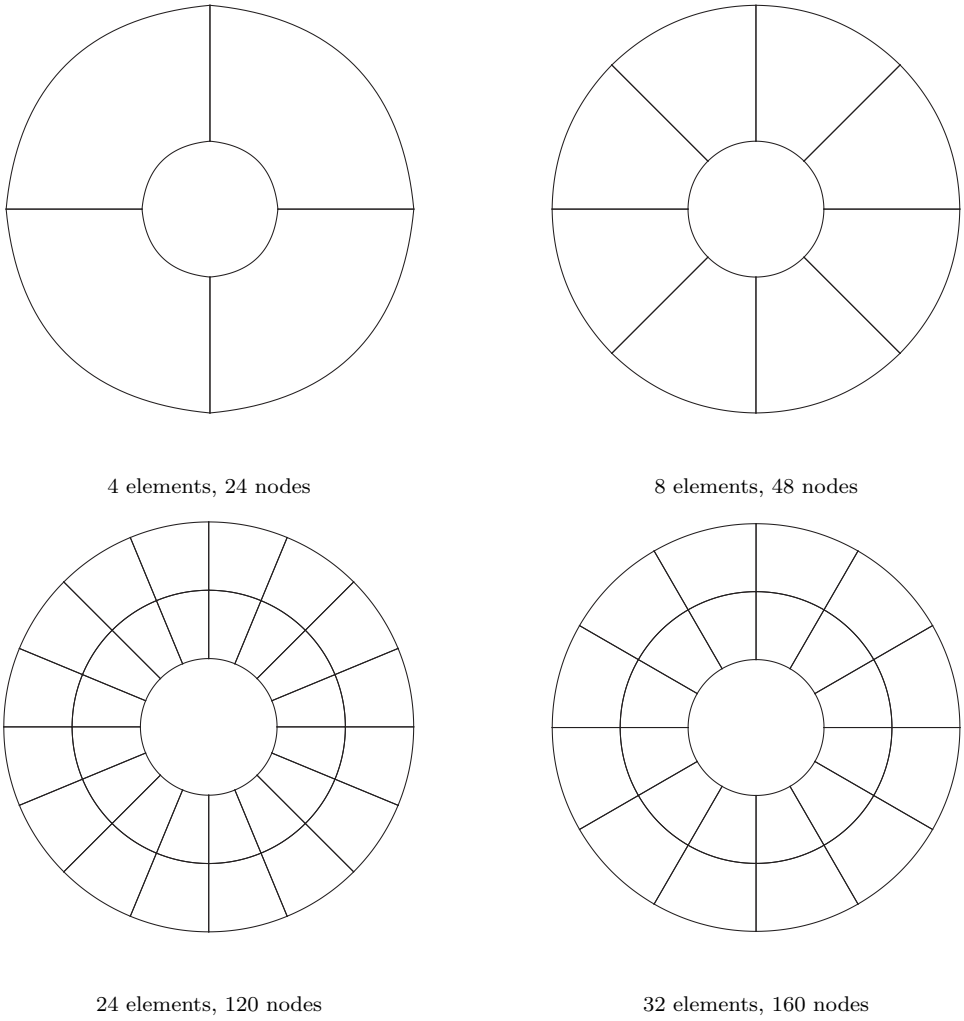

Figure 4.8: Interpolated geometry, $Q9$ mesh grids.

τ	$\varepsilon_1[\%]$	$\varepsilon_2^e[\%]$	$\varepsilon_2^i[\%]$
4.79	1.08	0.19	0.76
6.77	0.08	0.005	0.057
10.71	0.015	0.0006	0.012
12.36	0.005	0.00043	0.003

Table 4.3: Errors obtained with different $Q9$ mesh grids, $ka = 2\pi, m = 24$.

The exact and the interpolated geometries are used to solve the problem where the computational domain is defined by the outer and inner radii, $R/a = 3$ and $r/a = 1$, respectively. Four $Q9$ mesh grids displayed in Figure 4.8 are considered for the solution such that the number of elements is increased from 4 to 8, 24 and finally 32. As a higher number of elements is considered, the geometry interpolation is improved.

The problem is solved for the wave number $ka = 4\pi$ with the solution space enriched with 60 plane waves. The L_2 error of the result obtained with the exact geometry, ε_2^e, is compared to those of the interpolated geometry, ε_2^i, in Table 4.2 alongside τ and ε_1. Similar comparison is made for $ka = 2\pi$ with $m = 24$ in Table 4.3.

Both geometry descriptions lead to good quality results with the exact geometry providing a lower error.

The difference between both errors is investigated further. The mesh grids of 8 and 32 elements are considered. The first mesh is enriched with 60 plane waves. In order to achieve the same number of degrees of freedom per wave length the second mesh is enriched with 24 plane waves. The problem is solved for an increasing wave number $ka = 2\pi$ up to 10π.

The results obtained with both mesh grids for the exact and the interpolated geometries, are compared in Table 4.4. Again here, using the exact geometry leads to a smaller error. However, at a smaller number of degrees of freedom per wave length, $\tau = 2.14$ with 8 elements and $\tau = 3.57$ with 32 elements, the results with both geometries become similar. This may be expected as at low τ the accuracy of the method is reduced and the effect of the geometry interpolation is not obvious.

It should be noted that with larger elements, 8 elements mesh grid in this case, the effect of the geometry is clear even with $\tau = 2.68$. As mentioned earlier, the main point of using the PUFEM is utilizing large elements for the solution of wave problems. Therefore the effect of the geometry interpolation should be considered as it may affect the results especially when a high accuracy is sought.

		$Q9$ 8 elements		$Q9$ 32 elements	
ka	τ	$\varepsilon_2^e[\%]$	$\varepsilon_2^i[\%]$	$\varepsilon_2^e[\%]$	$\varepsilon_2^i[\%]$
2π	10.7	0.0073	0.057	0.00043	0.003
3π	7.14	0.017	0.083	0.00057	0.0056
4π	5.35	0.011	0.098	0.00049	0.0065
6π	3.57	0.027	0.21	0.015	0.015
8π	2.68	0.11	0.19	0.27	0.21
10π	2.14	0.99	0.94	1.79	1.87

Table 4.4: Errors obtained with $Q9$ mesh grids; $m = 60$ with 8 elements, $m = 24$ with 32 elements.

4.4 Effect of the radiation boundary condition

When solving a diffraction problem in an infinite media with numerical methods such as the PUFEM only a finite size domain can be considered. Different schemes were suggested to truncate the problem into a finite size where all the waves approaching the outer boundaries leave without any reflection or very little. In other words, the outer boundary must appear transparent to the outgoing waves. This is achieved through the use of either local Non-Reflecting Boundary Conditions (NRBCs), which are approximate boundary conditions [93, 94, 95] or non-local NRBCs, which are exact [96, 97, 98].

The word local means the boundary condition is applicable on each element separately such that there is no coupling between the elements on the boundaries. This is important at the implementation level with the finite element methods because a non-local operator results in a densely populated system matrix on the outer boundary spoiling the sparse character of the global system matrix. Thus the resulting system matrix is much more expensive to solve. Local and non-local boundary conditions are discussed in details in reference [95].

In a recent work, different boundary conditions of various orders, combined with the PUFEM, are compared for problems governed by the Helmholtz equation [99]. It is found that the Bayliss, Gunzburger and Turkel boundary condition of the second

order (BGT-2) leads to the smallest error among the considered boundary conditions.

Here, the Bayliss-Gunzburger-Turkel boundary condition of the first (BGT-1) and second (BGT-2) orders are implemented and their efficiency to allow waves to radiate away toward infinity is assessed by comparing their respective L_2 errors to the case where Robin boundary condition is used.

4.4.1 Problem formulation

Figure 4.3 shows a schematic diagram of the problem domain. The new boundary value problem is described by the Helmholtz equation

$$(\nabla^2 + k^2)\phi = 0 \qquad \text{in} \quad \Omega \tag{4.16}$$

Instead of implementing Robin boundary conditions as before Neumann and a non-reflecting radiation boundary conditions are applied on the domain inner (Γ_1) and outer (Γ_2) boundaries, respectively

$$\underline{\nabla\phi}.\underline{\mathrm{n}} = -\underline{\nabla\phi_I}.\underline{\mathrm{n}} \qquad \text{on} \quad \Gamma_1 \tag{4.17}$$

$$\underline{\nabla\phi}.\underline{\mathrm{n}} = B\phi \qquad \text{on} \quad \Gamma_2 \tag{4.18}$$

where B is an operator related to the choice of a non-reflecting boundary condition. Substituting the boundary conditions in the expression (2.5) leads to

$$\int_\Omega (-\underline{\nabla W}.\underline{\nabla\phi} + k^2 W\phi)d\Omega + \int_{\Gamma_2} WB\phi \; d\Gamma = \int_{\Gamma_1} W\underline{\nabla\phi_I}.\underline{\mathrm{n}} \; d\Gamma \tag{4.19}$$

The first and the second orders BGT boundary conditions are given by

$$\mathrm{BGT}-1: \qquad (\partial_\mathrm{r} - \mathrm{ik} + \frac{1}{2\mathrm{r}})\phi = 0 \tag{4.20}$$

$$\mathrm{BGT}-2: (\partial_\mathrm{r} - \mathrm{ik} + \frac{5}{2\mathrm{r}})(\partial_\mathrm{r} - \mathrm{ik} + \frac{1}{2\mathrm{r}})\phi = 0 \tag{4.21}$$

Implementing each order in (4.19) gives for the first order

$$\int_\Omega (\underline{\nabla W}.\underline{\nabla\phi} - k^2 W\phi)d\Omega + \int_{\Gamma_1} W\underline{\nabla\phi_I}.\underline{\mathrm{n}} \; d\Gamma + \int_{\Gamma_2} W(-\mathrm{i}k + \frac{1}{2R})\phi \; d\Gamma = 0 \tag{4.22}$$

and for the second order

$$\begin{aligned}\int_\Omega (\underline{\nabla W}.\underline{\nabla\phi} - k^2 W\phi)d\Omega + \int_{\Gamma_1} W\underline{\nabla\phi_I}.\underline{\mathrm{n}} \; d\Gamma + \int_{\Gamma_2} W\frac{1}{2R^2}(\mathrm{i}k - \frac{1}{R})^{-1}\frac{\partial^2\phi}{\partial\theta^2} \; d\Gamma \\ + \int_{\Gamma_2} W\frac{1}{2}(\mathrm{i}k - \frac{1}{R})^{-1}(2k^2 + \frac{3\mathrm{i}k}{R} - \frac{3}{4R^2})\phi \; d\Gamma = 0\end{aligned} \tag{4.23}$$

No. of elements	τ	BGT-1	BGT-2	Robin
4	4.79	1.98	0.191	0.190
8	6.77	1.98	0.061	0.0055
24	10.7	1.98	0.060	0.0060
36	12.4	1.98	0.060	0.0043

Table 4.5: L_2 errors result of different boundary conditions, $ka = 2\pi, m = 24$.

where R is the radius of the outer boundary. It should be noted that the boundary integral along Γ_2 in (4.19) involving a partial second derivative of the unknown potential ϕ with respect to θ, is treated as a second order total derivative because R is constant. Thus the following integration by part is possible

$$\int_{\Gamma_2} W \frac{d^2\phi}{d\theta^2}\, d\Gamma = \int_{\Gamma_2} \frac{dW}{d\theta}\frac{d\phi}{d\theta}\, d\Gamma \tag{4.24}$$

given that Γ_2 is a smooth closed curve which is the case as Γ_2 is a circle.

4.4.2 Numerical tests

The previous problem is solved for the wave number $ka = 2\pi$ using the exact geometry. The previous mesh grids of Figure 4.8 are reconsidered for the solution with the solution space enriched by 24 plane waves. Table 4.5 shows the L_2 errors corresponding to the different boundary conditions.

The results in all the cases are better with BGT-2 compared to when BGT-1 is used. The error introduced by the artificial boundary conditions is exposed when BGT-1 or -2 are compared to the Robin boundary condition. The L_2 error with the Robin boundary condition improves by refining the mesh thanks to the increase in the number of degrees of freedom. On the other hand the error with BGT-1 does not improve ($\varepsilon_2^e = 1.98\%$) while with BGT-2 it improves up to the case with 8 elements ($\varepsilon_2^e = 0.06\%$). It is obvious that increasing the number of degrees of freedom does not reduce the error further.

To improve the previous error obtained with BGT-1 and BGT-2, it is possible to move the artificial boundary further away from the scatterer. This effect is studied by solving the problem with the exact geometry and for various extent of the com-

R/a	2	3	4	5	6
8 elements	5.18	1.978	1.055	0.656	0.447
16 elements	5.12	1.978	1.055	0.656	0.447

Table 4.6: Increasing outer radius with BGT-1, L_2 error in [%] for $ka = 2\pi$, $m = 24$.

R/a	2	3	4	5	6
8 elements	0.397	0.060	0.017	0.0069	0.0033
16 elements	1.192	0.060	0.017	0.0068	0.0033

Table 4.7: Increasing outer radius with BGT-2, L_2 error in [%] for $ka = 2\pi$, $m = 24$.

putational domain. In the angular direction two discretization levels are considered (8 and 16 elements). In the radial direction a layer of element is considered for each unit of length. The domain outer radius is increased in steps from $R/a = 2$ to 6 thus the number of element layers is increased from 1 to 5, respectively. To ensure the accuracy of the method, the number τ of degrees of freedom per wavelength is kept all the time above 5 by enriching the solution space with 24 plane waves. The L_2 error corresponding to each case is reported in Tables 4.6 and 4.7 for BGT-1 and BGT-2, respectively.

It can be seen from this set of results that the BGT-2 performs better than BGT-1. As the outer boundary gets farther from the scatterer the performance of the boundary conditions improves. The discretization levels with 8 or 16 elements, except for the case $R/a = 2$ with BGT-2, seems to have a small influence on the error. By moving the domain boundary away, the minimum error is reduced to about 0.5% with BGT-1 and to 0.003% with BGT-2.

4.5 Conclusion

In this Chapter, various sources of error in the PUFEM are investigated and their effect is analysed on the quality of the results. It is shown that both structured and non-structured mesh grids may lead to good quality results provided that the elements of the mesh grids are of good quality as well. It is also shown that conjugated

and unconjugated formulations are practically similar for an even number of enrichment plane waves evenly spaced in the plane. Given that the elements span many wavelengths, it is crucial to accurately describe the geometry of the problem to avoid a contribution to the error. Last, using the second order Bayliss-Gunzburger-Turkel boundary condition at a reasonable distance from the scattering object ensures good quality results in exterior scattering problems.

In the next Chapter, the integration process is discussed. It is known that, in the PUFEM, the computational burden shifts from the solution process to the assembling process because of the required high integration scheme. To overcome this difficulty, an exact integration scheme is proposed for the 3-noded elements.

Chapter 5

Exact integration scheme for 3-noded elements

Up to now, in this work, the element matrices involving the integration of highly oscillatory functions were obtained by using high order Gauss-Legendre quadratures. Because the elements are capable of containing many wavelengths per nodal spacing, huge numbers of integration points are required to perform the integration. In past work, for example, Laghrouche and Bettess [30] used up to 120 by 120 integration points to evaluate element matrices entries in order to solve a wave scattering problem in two dimensions. A total of 14,400 are therefore used across each element and the same approach in three-dimensional problems would require, under similar conditions, a total of 1,728,000 integration points per finite element. Despite the fact that the integration process is independent from an element to another and hence suitable for parallel computing, it remains a heavy computational burden.

In contrast to the FEM, in which the assembling process is fast in comparison to the solution process, in the PUFEM the computational effort shifts from the solver to the assembling process as a consequence of the numerical integration. Therefore efforts to overcome this difficulty are necessary to make the method competitive.

Different attempts were made to speed up the integration of the highly oscillatory functions in particular those involving plane waves. Ortiz and Sanchez [41] replaced the integral over an area with linear integrals by rotating the local coordinate system. In other attempts, semi-analytical integration schemes were developed for quadrilat-

eral and triangular elements by Sugimoto *et al.* [100] and Bettess *et al.* [101]. In another approach, found in reference [102], Darrigrand introduced two mesh grids such that the problem unknowns are defined over a coarse mesh while the geometry is defined through a finer mesh. This approach leads to the evaluation of the integrals over small 'elements' where a low order quadrature is used, typically only two integration points would be needed. However, this approach does not lead to a reduction in the computation effort of the integration process. In other words, it uses low order quadratures, rather than high order schemes, but over high number of elements.

Another approach where the integrals are evaluated over subdivisions of the elements rather than the elements themselves is found in the work of Trevelyan and Honnor [103]. The subdivisions are aligned such that the oscillations are minimized in one direction. Thus the integral may be evaluated over these subdivisions with a low order numerical scheme as it only oscillates in one direction.

Gordon [104] used the divergence theorem to exactly integrate an oscillatory function over a polygon. This approach reduces the surface integral to a line integral over the polygon boundary, which can in turn be evaluated at the vertices of the polygon edges provided that they are straight lines. This work was extended to volume integrals by Gabard [105]. A similar approach was adopted by El Kacimi and Laghrouche [35] in the evaluation of element matrices obtained by the PUFEM for elastic wave scattering problems.

It is obvious that an exact integration procedure would significantly speed up the PUFEM and make it even more competitive. Here, the same approach presented in references [35, 104] is used to evaluate the matrices of 3-noded elements. The scheme is tested numerically on a wave scattering problem by comparing its results to a high order numerical integration scheme. The comparison include the conditioning, the L_2 error and the computation time needed to obtain a solution.

5.1 Exact integration scheme

First, the idea found in references [35, 104] is explained. Let us consider the following integral over an element Ω_e

$$I_l(Y) = \int_{\Omega_e} (\underline{\mathrm{d}}.\underline{\nabla})^l Y(x,y) e^{\mathrm{i}k(\underline{\mathrm{d}}.\underline{\mathrm{x}})} d\Omega \tag{5.1}$$

where

$$\begin{aligned}(\underline{\mathrm{d}}.\underline{\nabla})^{l+1} Y(x,y) &= (\underline{\mathrm{d}}.\underline{\nabla})((\underline{\mathrm{d}}.\underline{\nabla})^l Y(x,y)) \\ (\underline{\mathrm{d}}.\underline{\nabla})^0 Y(x,y) &= Y(x,y)\end{aligned} \tag{5.2}$$

with $\underline{\mathrm{d}}$ and $\underline{\mathrm{x}}$ being the direction and the position vectors, respectively, such that $\underline{\mathrm{d}} = (\cos\theta, \sin\theta)^\top$ and $\underline{\mathrm{x}} = (x,y)^\top$. Using

$$(\underline{\mathrm{d}}.\underline{\nabla}) e^{\mathrm{i}k(\underline{\mathrm{d}}.\underline{\mathrm{x}})} = \mathrm{i}k|\underline{\mathrm{d}}|^2 e^{\mathrm{i}k(\underline{\mathrm{d}}.\underline{\mathrm{x}})} = \mathrm{i}k e^{\mathrm{i}k(\underline{\mathrm{d}}.\underline{\mathrm{x}})} \tag{5.3}$$

where $|\underline{\mathrm{d}}|$ is the Euclidean norm of the vector $\underline{\mathrm{d}}$, and making use of expression (5.3) it is possible to rewrite the integral (5.1) as

$$I_l(Y) = \frac{1}{\mathrm{i}k} \int_{\Omega_e} (\underline{\mathrm{d}}.\underline{\nabla})^l Y(x,y) (\underline{\mathrm{d}}.\underline{\nabla}) e^{\mathrm{i}k(\underline{\mathrm{d}}.\underline{\mathrm{x}})} d\Omega \tag{5.4}$$

Applying the divergence theorem leads to

$$\begin{aligned}I_l(Y) =& \frac{1}{\mathrm{i}k} \int_{\Gamma_e} (\underline{\mathrm{d}}.\underline{\nabla})^l Y(x,y) e^{\mathrm{i}k(\underline{\mathrm{d}}.\underline{\mathrm{x}})} (\underline{\mathrm{d}}.\underline{\mathrm{n}}) d\Gamma \\ & - \frac{1}{\mathrm{i}k} \int_{\Omega_e} (\underline{\mathrm{d}}.\underline{\nabla})^{l+1} Y(x,y) e^{\mathrm{i}k(\underline{\mathrm{d}}.\underline{\mathrm{x}})} d\Omega\end{aligned} \tag{5.5}$$

or

$$I_l(Y) = \frac{1}{\mathrm{i}k}(G_l(Y) - I_{l+1}(Y)) \tag{5.6}$$

where

$$G_l(Y) = \int_{\Gamma_e} (\underline{\mathrm{d}}.\underline{\nabla})^l Y(x,y) e^{\mathrm{i}k(\underline{\mathrm{d}}.\underline{\mathrm{x}})} (\underline{\mathrm{d}}.\underline{\mathrm{n}}) d\Gamma \tag{5.7}$$

In the same way as above and using a recurrence formula it is possible to show that

$$I_0(Y) = -\sum_{j=0}^{l} (-\frac{1}{\mathrm{i}k})^{j+1} G_j(Y) - (-\frac{1}{\mathrm{i}k})^{l+1} I_{l+1}(Y) \tag{5.8}$$

If the polynomial $Y(x,y)$ function is of the order p then by taking $l = p$ the previous equation (5.8) could be reduced to

$$I_0(Y) = -\sum_{j=0}^{p} (-\frac{1}{\mathrm{i}k})^{j+1} G_j(Y) \tag{5.9}$$

which is a valuable result that could be easily used in the PUFEM, when integrating over straight edge elements, where the integrals are of the form

$$\int_{\Omega_e} N_j N_i e^{\mathrm{i}k(x\cos\theta_l + y\sin\theta_l)} e^{\mathrm{i}k(x\cos\theta_q + y\sin\theta_q)} d\Omega \tag{5.10}$$

Considering a 3-noded element where the shape functions are given by

$$\begin{aligned} N_1 =& 1-\xi-\eta \\ N_2 =& \xi \\ N_3 =& \eta \end{aligned} \tag{5.11}$$

and their first order derivative are constants, the implementation of the above conclusion is straightforward which is shown next for $N_j = N_1$ and $N_i = N_2$ while other integrals could be obtained in a similar way.

Let us write the integral (5.10) as

$$I_0(N_1N_2) = \int_{\Omega_e} N_1N_2 e^{\mathrm{i}k(x(\cos\theta_l+\cos\theta_q)+y(\sin\theta_l+\sin\theta_q))} d\Omega \tag{5.12}$$

or

$$I_0(N_1N_2) = -\sum_{j=0}^{2} (-\frac{1}{\mathrm{i}k|\underline{\mathrm{d}}|^2})^{j+1} G_j(N_1N_2) \tag{5.13}$$

where

$$G_j(N_1N_2) = \int_{\Gamma_e} (\underline{\mathrm{d}}.\underline{\nabla})^j (N_1N_2) e^{\mathrm{i}k(\underline{\mathrm{d}}.\underline{\mathrm{x}})} (\underline{\mathrm{d}}.\underline{\mathrm{n}}) d\Gamma \tag{5.14}$$

for notation convenience let us put $\underline{\mathrm{d}} = (\cos\theta_l + \cos\theta_q, \sin\theta_l + \sin\theta_q)^\top$. The equation (5.13) is a summation of three terms. Each term is discussed separately.

For $j = 2$

$$\begin{aligned} (\underline{\mathrm{d}}.\underline{\nabla})^2(N_1N_2) &= (\underline{\mathrm{d}}.\underline{\nabla})((\underline{\mathrm{d}}.\underline{\nabla})(N_1N_2)) \\ &= (\underline{\mathrm{d}}.\underline{\nabla})(N_1(\underline{\mathrm{d}}.\underline{\nabla})(N_2) + N_2(\underline{\mathrm{d}}.\underline{\nabla})(N_1)) \\ &= 2(\underline{\mathrm{d}}.\underline{\nabla}N_1)(\underline{\mathrm{d}}.\underline{\nabla}N_2) \end{aligned} \tag{5.15}$$

Thus the first term of the summation becomes

$$G_2(N_1N_2) = 2(\underline{\mathrm{d}}.\underline{\nabla}N_1)(\underline{\mathrm{d}}.\underline{\nabla}N_2) \int_{\Gamma_e} e^{\mathrm{i}k(\underline{\mathrm{d}}.\underline{\mathrm{x}})} (\underline{\mathrm{d}}.\underline{\mathrm{n}}) d\Gamma \tag{5.16}$$

In a similar way one can obtain the terms for $j = 1$

$$G_1(N_1N_2) = (\underline{\mathrm{d}}.\underline{\nabla}N_1) \int_{\Gamma_e} N_2 e^{\mathrm{i}k(\underline{\mathrm{d}}.\underline{\mathrm{x}})} (\underline{\mathrm{d}}.\underline{\mathrm{n}}) d\Gamma + (\underline{\mathrm{d}}.\underline{\nabla}N_2) \int_{\Gamma_e} N_1 e^{\mathrm{i}k(\underline{\mathrm{d}}.\underline{\mathrm{x}})} (\underline{\mathrm{d}}.\underline{\mathrm{n}}) d\Gamma \tag{5.17}$$

and for $j = 0$

$$G_0(N_1N_2) = \int_{\Gamma_e} N_1N_2 e^{\mathrm{i}k(\underline{\mathrm{d}}.\underline{\mathrm{x}})}(\underline{\mathrm{d}}.\underline{\mathrm{n}})d\Gamma \tag{5.18}$$

Taking into consideration that $N_1N_2 = 0$ on the edges Γ_{13} and Γ_{23} then the above integrals need only to be evaluated on the edge Γ_{12}

$$\begin{aligned} G_2(N_1N_2) &= 2(\underline{\mathrm{d}}.\underline{\nabla}N_1)(\underline{\mathrm{d}}.\underline{\nabla}N_2)D_{12}(1) \\ G_1(N_1N_2) &= (\underline{\mathrm{d}}.\underline{\nabla}N_1)D_{12}(N_2) + (\underline{\mathrm{d}}.\underline{\nabla}N_2)D_{12}(N_1) \\ G_0(N_1N_2) &= D_{12}(N_1N_2) \end{aligned} \tag{5.19}$$

where

$$D_{12}(Y) = \int_{\Gamma_{12}} Y e^{\mathrm{i}k(\underline{\mathrm{d}}.\underline{\mathrm{x}})}(\underline{\mathrm{d}}.\underline{\mathrm{n}})d\Gamma \tag{5.20}$$

The Jacobian matrix is given by

$$J = \begin{bmatrix} \frac{\partial x}{\partial \xi} & \frac{\partial x}{\partial \eta} \\ \frac{\partial y}{\partial \xi} & \frac{\partial y}{\partial \eta} \end{bmatrix}$$

Since

$$\underline{\mathrm{x}} = \underline{\mathrm{x}}_1N_1 + \underline{\mathrm{x}}_2N_2 + \underline{\mathrm{x}}_3N_3 \quad \text{and} \quad dxdy = det(J)d\xi d\eta \tag{5.21}$$

where $det(J)$ is the determinant of the Jacobian matrix, then it is possible to change the x and y in the integral (5.10) into ξ and η. Using the integration by parts the values of the integrals (5.20) could be found explicitly

$$\begin{aligned} D_{12}(1) &= \gamma\underline{\mathrm{d}}.\underline{\mathrm{n}}_1|\underline{\mathrm{g}}_{12}|(e^{\mathrm{ik}\underline{\mathrm{d}}.\underline{\mathrm{s}}_2} - e^{\mathrm{ik}\underline{\mathrm{d}}.\underline{\mathrm{s}}_1}) \\ D_{12}(N_1) &= \gamma(-\underline{\mathrm{d}}.\underline{\mathrm{n}}_1|\underline{\mathrm{g}}_{12}|(e^{\mathrm{ik}\underline{\mathrm{d}}.\underline{\mathrm{s}}_1} + D_{12}(1)) \\ D_{12}(N_2) &= \gamma(\underline{\mathrm{d}}.\underline{\mathrm{n}}_1|\underline{\mathrm{g}}_{12}|(e^{\mathrm{ik}\underline{\mathrm{d}}.\underline{\mathrm{s}}_2} - D_{12}(1)) \\ D_{12}(N_1N_2) &= \gamma(-D_{12}(N_1) + D_{12}(N_2)) \end{aligned} \tag{5.22}$$

where $\gamma = \frac{1}{\mathrm{i}k(\underline{\mathrm{d}}.\underline{\mathrm{g}}_{12})}$, with $\underline{\mathrm{s}}_i$ being the position vector of the node i and $\underline{\mathrm{g}}_{ij}$ being the vector going from the node i to the node j in a finite element.

If $\underline{\mathrm{d}}.\underline{\mathrm{g}}_{12} = 0$ then $\underline{\mathrm{d}}$ is perpendicular to the edge Γ_{12}. The above integrals are easily evaluated as

$$\begin{aligned} D_{12}(1) &= \underline{\mathrm{d}}.\underline{\mathrm{n}}_1|\underline{\mathrm{g}}_{12}|e^{\mathrm{i}k\underline{\mathrm{d}}.s^1} \\ D_{12}(N_1) &= \frac{1}{2}D_{12}(1)) \\ D_{12}(N_2) &= \frac{1}{2}D_{12}(1)) \\ D_{12}(N_1N_2) &= \frac{1}{6}D_{12}(N_2)) \end{aligned} \tag{5.23}$$

Another special case happens when $\underline{d} = \underline{0}$. Then the exponential term is equal to one and the integral (5.13) becomes a polynomial integral which can be easily evaluated

$$I_0(N_1 N_2) = \frac{1}{24} det(J) \tag{5.24}$$

For the numerical implementation, the quantities $\underline{d}.\underline{g}_{12}$ and $\underline{d}$ are considered to be equal to zero if $|\underline{d}.\underline{g}_{12}| \leq \varepsilon$ and $|\underline{d}| \leq \varepsilon$, respectively, where $\varepsilon = 10^{-6}$.

5.2 Numerical results

The mono scattering problem of Chapter 3 is reconsidered with the mesh grid h_1 (Figure 3.1, mesh (b)). Solving the linear system takes the same time with both the numerical and exact integration schemes. The difference lies in the time needed to evaluate the entries of the system matrix. The total computational times required to obtain the numerical solutions with both schemes are then compared.

For the numerical integration the number of integration points is chosen such that there are ten integration points per wavelength. Table 5.1 shows the wave number ka for which the problem is solved, with the other considered parameters: the number m of enriching plane waves, the ratio h/λ, the number τ of degrees of freedom per wavelength, the number n_{gauss} of Gauss points and the total number of locations of the system matrix to be stored, $totsys$.

The number of enriching plane waves is kept constant for a range of wave numbers that is $m = 4$ for $(\frac{2\pi}{7} \leq ka \leq \frac{2\pi}{3})$ and $m = 80$ for $(6\pi \leq ka \leq 12\pi)$. The resulting system matrix has a fixed size for each of the two ranges, $totsys = 2170$ and $849,000$ respectively. The calculations were performed using a Fortran 90-95 code with double precision variables on an Intel Xeon 3.0 GHz processor with 3.75 GB of RAM under Microsoft Windows Server 2003. For illustration purpose, Figure 5.1 shows the real part of the diffracted potential obtained with the PUFEM for the smallest and largest values of the wave number $ka = \frac{2\pi}{7}$ and 12π.

Figures 5.2, 5.3 and 5.4 show the CPU time, the L_2 error and the condition number κ, being plotted against the wave number for all the cases presented in Table 5.1.

For a low wave number, where only a few integration points are needed, it is clear that using the exact or the numerical integration schemes leads practically to the same

ka	m	h/λ	τ	n_{gauss}	$totsys$
$\frac{2\pi}{7}$	4	0.20	17.5	6	2170
$\frac{2\pi}{6}$	4	0.24	15.0	6	2170
$\frac{2\pi}{5}$	4	0.28	12.5	6	2170
$\frac{2\pi}{4}$	4	0.35	10.0	6	2170
$\frac{2\pi}{3}$	4	0.47	7.5	6	2170
6.0π	80	4.24	3.73	42	849000
6.5π	80	4.60	3.44	46	849000
7.0π	80	4.95	3.19	50	849000
7.5π	80	5.30	2.98	54	849000
8.0π	80	5.66	2.80	58	849000
8.5π	80	6.01	2.63	62	849000
9.0π	80	6.36	2.48	64	849000
9.5π	80	6.72	2.35	68	849000
10.0π	80	7.07	2.24	72	849000
10.5π	80	7.42	2.13	76	849000
11.0π	80	7.78	2.03	78	849000
11.5π	80	8.13	1.94	82	849000
12.0π	80	8.49	1.86	86	849000

Table 5.1: Considered parameters for different mesh grids and enrichments.

CPU time, L_2 error and condition number. However, when a high wave number is considered, where many integration points are needed, the exact integration scheme needs a significantly shorter CPU time compared to the numerical scheme. The results obtained with both schemes lead to the same condition number and L_2 error.

Unlike the FEM, where most of the computational time is dedicated to the solution of the linear system of equations, in the PUFEM most of the computational time is dedicated to the evaluation of elementary matrices, when the numerical integration is used with multi-wavelength sized elements. Therefore reducing the assembling process time in the PUFEM through the use of an exact integration is significantly rewarding in terms of computational effort reduction. One can see this in Figure 5.2

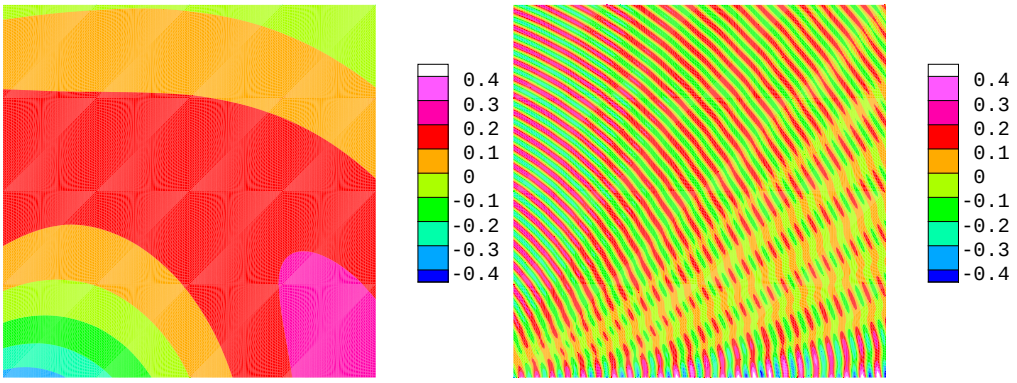

Figure 5.1: Real part of the diffracted potential for (left) $ka = \frac{2\pi}{7}, \tau = 17.5, \varepsilon_2 = 0.23\%$ and (right) $ka = 12.0\pi, \tau = 1.86, \varepsilon_2 = 0.0015\%$.

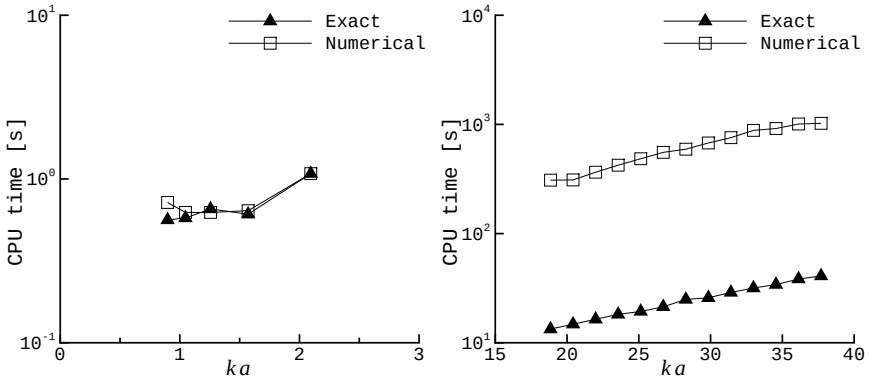

Figure 5.2: Solution CPU time for (left) $m = 4$ and (right) $m = 80$.

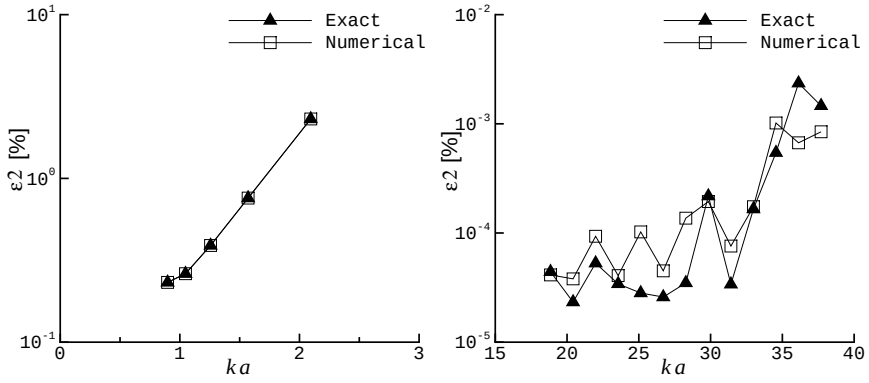

Figure 5.3: Solution L_2 error for (left) $m = 4$ and (right) $m = 80$.

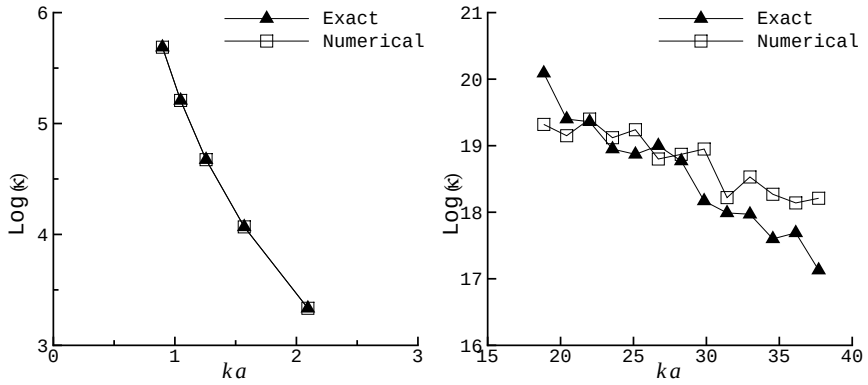

Figure 5.4: Condition number κ plots for (left) $m = 4$ and (right) $m = 80$.

where the full solution time is reduced by more than 90% when the exact scheme is used.

The drastic reduction resulting from the use of the exact integration makes the PUFEM very competitive compared to the conventional FEM. The integration scheme presented above could be developed to other types of finite elements. The only constraint of the scheme, however, is being limited to straight edge finite elements, in two dimensions, and flat surfaces elements with straight edges, in three dimensions. But, in general, it is possible to fill-in most of the computational domain with straight edge elements and hence use an exact integration, while near curved boundaries use elements with curved edges, which then require the use of numerical integration. Also, to speed up the solution process further, parallel processing of the element matrices could be an extra option.

5.3 Conclusion

The results of the previous chapters show that the performance of the PUFEM improves when multi-wavelength sized elements are used. The large elements having the advantage of containing many wavelengths per nodal spacing result in a new difficulty which is integrating highly oscillatory functions over relatively large elements, thus a high order integration scheme is needed which is computationally expensive.

In this Chapter, an exact integration scheme is presented for 3-noded elements, which effectively reduces the solution time with multi-wavelength sized elements. However, the new scheme is limited to straight edge elements. Hence it is proposed to fill

the computational domain with such elements which are exactly integrated and use curved edge elements to describe geometrical details, such as curved boundaries, which are numerically evaluated and for which parallel processing is suitable.

Another approach consists to keep straight edge elements but refine the mesh near curved boundaries to accurately describe geometrical details. This is proposed in the next Chapter when dealing with multiple scattering problems.

Chapter 6

Multiple scattering problem

Waves diffract when propagating between different media or when bending around obstacles. This characteristic behaviour of waves has been explored and modelled by many scientists. In the mathematical physics, the paper of Watson [106] published in 1918 is perhaps one of the earliest works where an analytical model of a wave diffraction problem was proposed. Other notable contributions on different aspects of this problem include, but not limited to, the work of Van der Pol and Bremmer [107], Franz *et al.* [108, 109, 110] and Clemmow [111].

In offshore engineering, a plane wave scattered by a vertical obstacle is a classical problem governed by the Helmholtz equation. Havelock [88] developed the first analytical model for this problem where the wave propagates in deep water and the scatterer is a vertical rigid circular cylinder. Later, MacCamy and Fuchs [112] extended this work to scattering in medium depth water. Other contributions were made by developing analytical models where the scatterer is not circular. Chen and Mei [113] and later Williams [114] worked on problems with an elliptical scatterer, Hillion [115] considered a parabolic scatterer and Mansour *et al.* [116] studied a cosine-type radial perturbation scatterer.

All the work mentioned above is limited to a single scatterer situation which could be encountered in different physical phenomena, for example a leg of an offshore platform. However, such a platform is usually supported by four legs. Thus the wave scattered by one leg will hit the other legs to scatter again and so on. This re-scattering process could only be neglected if the legs are far apart with respect to

the wavelength otherwise it is not negligible. In this context, Linton and Evans [117] extended the mono-scattering problem to multiple scattering. Martin [118] discussed many theoretical aspects and gathered different references in his textbook which is dedicated to multiple scattering problems. The analytical model of a multiple scattering problem involving rigid circular cylinders is presented in Appendix B.

So far the solution of the Helmholtz equation with the PUFEM was investigated by solving mono scattering problems. In this Chapter, the solution is extended to multiple scattering problems. A sequence of problems with up to nine scatterers is solved using 3-noded linear or 6-noded quadratic elements.

6.1 Boundary value problems

Two boundary value problems are considered in this Chapter. The first one is governed by the Helmholtz equation with a Robin type boundary condition. The weak formulation of this problem is equivalent to the one presented in Chapter 2 but the source term g in expression (2.3) must be reevaluated using the multiple scattering analytical solution.

The potential of the plane wave scattered by N cylinders is given by (see B.6)

$$\phi_S = \sum_{j=1}^{NC} \sum_{q=-\infty}^{+\infty} B_q^j \frac{J_q'(ka_j)}{H_q'(ka_j)} H_q(kr_j) e^{\mathrm{i}q\theta_j} \tag{6.1}$$

the derivative of the scattered potential with respect to the normal to the boundary is given by

$$\underline{\nabla \phi_S}.\underline{\mathrm{n}} = \frac{\partial \phi_S}{\partial x}\mathrm{n_x} + \frac{\partial \phi_S}{\partial \mathrm{y}}\mathrm{n_y} \tag{6.2}$$

where $\mathrm{n_x}$ and $\mathrm{n_y}$ are the components of the normal vector in a Cartesian coordinate system. The diffracted potential given by equation (6.1) is expressed in NC local polar coordinate systems defined at the centres of the diffracting cylinders, thus the derivative must be redefined with respect to these local coordinates

$$\underline{\nabla \phi_S}.\underline{\mathrm{n}} = \left(\frac{\partial \phi_S}{\partial r_j}\frac{\partial r_j}{\partial x} + \frac{\partial \phi_S}{\partial \theta_j}\frac{\partial \theta_j}{\partial x}\right)\mathrm{n_x} + \left(\frac{\partial \phi_S}{\partial \mathrm{r_j}}\frac{\partial \mathrm{r_j}}{\partial \mathrm{y}} + \frac{\partial \phi_S}{\partial \theta_\mathrm{j}}\frac{\partial \theta_\mathrm{j}}{\partial \mathrm{y}}\right)\mathrm{n_y} \tag{6.3}$$

where r_j and θ_j are the local polar coordinates located at the center of the jth cylinder (x_j, y_j). All these local coordinates could be expressed as a function of the

same Cartesian coordinate system

$$r_j = \sqrt{(x - x_j)^2 + (y - y_j)^2} \qquad \theta_j = \arctan\left(\frac{y - y_j}{x - x_j}\right) \tag{6.4}$$

The derivatives expressed in the Cartesian system are

$$\begin{aligned} \frac{\partial r_j}{\partial x} &= \cos\theta_j \qquad & \frac{\partial \theta_j}{\partial x} &= -\frac{1}{r_j}\sin\theta_j \\ \frac{\partial r_j}{\partial y} &= \sin\theta_j \qquad & \frac{\partial \theta_j}{\partial y} &= +\frac{1}{r_j}\cos\theta_j \end{aligned} \tag{6.5}$$

Differentiating (6.1) with respect to the normal $\underline{\mathrm{n}}$ and making use of (6.3) and (6.5) results, expression (6.2) becoming

$$\begin{aligned} \underline{\nabla\phi_S}.\underline{\mathrm{n}} = \sum_{j=1}^{NC}\sum_{q=-Q}^{+Q} B_q^j \frac{J_q'(ka_j)}{H_q'(ka_j)}[kH_q'(kr_j)e^{\mathrm{i}q\theta_j}(\mathrm{n_x}\cos\theta_\mathrm{j} + \mathrm{n_y}\sin\theta_\mathrm{j}) \\ + \frac{\mathrm{i}q}{r_j}H_q(kr_j)e^{\mathrm{i}q\theta_j}(-\mathrm{n_x}\sin\theta_\mathrm{j} + \mathrm{n_y}\cos\theta_\mathrm{j})] \end{aligned} \tag{6.6}$$

where the unknown B_q^j is constant for a specific system of scatterers because it only depends on the spatial distribution and the geometry of the cylinders. Substituting (6.1) and (6.6) into (2.3) yields the required value of g

$$\begin{aligned} g = \sum_{j=1}^{NC}\sum_{q=-Q}^{+Q} B_q^j \frac{J_q'(ka_j)}{H_q'(ka_j)}e^{\mathrm{i}q\theta_j}[kH_q'(kr_j)(\mathrm{n_x}\cos\theta_\mathrm{j} + \mathrm{n_y}\sin\theta_\mathrm{j}) \\ + \mathrm{i}H_q(kr_j)(-\mathrm{n_x}\frac{\mathrm{q}}{\mathrm{r_j}}\sin\theta_\mathrm{j} + \mathrm{n_y}\frac{\mathrm{q}}{\mathrm{r_j}}\cos\theta_\mathrm{j} + \mathrm{k})] \end{aligned} \tag{6.7}$$

The second boundary value problem considered in this Chapter is governed by the Helmholtz equation with Neumann boundary condition applied on the scatterers surfaces and BGT-2 radiation condition [99] applied on the domain exterior boundary. The weak form for this problem is similar to expression (4.24) which is fully derived in Chapter 4. However, here Neumann boundary condition is applied on all the scatterers rather than a single one. Thus the weak form is rewritten in the following way

$$\begin{aligned} \int_\Omega (\underline{\nabla W}.\underline{\nabla\phi} - k^2 W\phi)d\Omega + \sum_{j=1}^{NC}\int_{\Gamma_j} W\underline{\nabla\phi_I}.\underline{\mathrm{n}}\; d\Gamma + \int_{\Gamma_R} W\frac{1}{2R^2}(\mathrm{i}k - \frac{1}{R})^{-1}\frac{\partial^2\phi}{\partial\theta^2}\; d\Gamma \\ + \int_{\Gamma_R} W\frac{1}{2}(\mathrm{i}k - \frac{1}{R})^{-1}(2k^2 + \frac{3\mathrm{i}k}{R} - \frac{3}{4R^2})\phi\; d\Gamma = 0 \end{aligned} \tag{6.8}$$

where Γ_R is the exterior boundary and Γ_j is the surface of the scatterer number j; $j = 1, 2, \ldots NC$. First, a general form of Neumann boundary condition should be

derived where the centre of the scatterer number j is located at an arbitrary point (x_j, y_j).

$$\underline{\nabla\phi_S}.\underline{\mathrm{n_j}} + \underline{\nabla\phi_I}.\underline{\mathrm{n_j}} = 0 \qquad \text{on} \quad \Gamma_j \tag{6.9}$$

where $\underline{\mathrm{n}}_j$ is the normal to the surface of this scatterer. The derivative of the incident wave with respect to the normal, is found in the same way as in (6.2)

$$\underline{\nabla\phi_I}.\underline{\mathrm{n}} = \frac{\partial\phi_I}{\partial x}\mathrm{n_x} + \frac{\partial\phi_\mathrm{I}}{\partial \mathrm{y}}\mathrm{n_y} \tag{6.10}$$

The normal at any point (x, y) of the scatterer surface could be expressed as a function of this point and the centre of the scatterer

$$\underline{\mathrm{n_j}} = \frac{1}{\sqrt{(x_j - x)^2 + (y_j - y)^2}} \left\{ \begin{array}{c} (x_j - x) \\ (y_j - y) \end{array} \right\} \tag{6.11}$$

If the incident wave is a plane wave propagating in the positive x-direction

$$\phi_I = e^{\mathrm{i}kx} \tag{6.12}$$

then making use of (6.10) and (6.11) the derivative could be expressed as

$$\underline{\nabla\phi_I}.\underline{\mathrm{n_j}} = \mathrm{i}ke^{\mathrm{i}kx}\frac{x_j - x}{\sqrt{(x_j - x)^2 + (y_j - y)^2}} \tag{6.13}$$

Thus the integral over the scatterers surfaces in (6.8) could be rewritten as

$$\mathrm{i}k\sum_{j=1}^{NC}\int_{\Gamma_j}\frac{We^{\mathrm{i}kx}(x_j - x)}{\sqrt{(x_j - x)^2 + (y_j - y)^2}}d\Gamma \tag{6.14}$$

Substituting this back into (6.8) gives

$$\begin{gathered}\int_{\Gamma_R} W\frac{1}{2R^2}(\mathrm{i}k - \frac{1}{R})^{-1}\frac{\partial^2\phi}{\partial\theta^2}\,d\Gamma + \int_{\Gamma_R} W\frac{1}{2}(\mathrm{i}k - \frac{1}{R})^{-1}(2k^2 + \frac{3\mathrm{i}k}{R} - \frac{3}{4R^2})\phi\,d\Gamma \\ \int_\Omega(\underline{\nabla W}.\underline{\nabla\phi} - k^2W\phi)d\Omega + \mathrm{i}k\sum_{j=1}^{NC}\int_{\Gamma_j}\frac{We^{\mathrm{i}kx}(x_i - x)}{\sqrt{(x_i - x)^2 + (y_i - y)^2}}\,d\Gamma = 0\end{gathered} \tag{6.15}$$

which is the second weak form to be solved in this Chapter. The boundary integral along Γ_R in (6.15) involving a partial second derivative of the unknown potential ϕ with respect to θ, is treated in the same way as in Chapter 4.

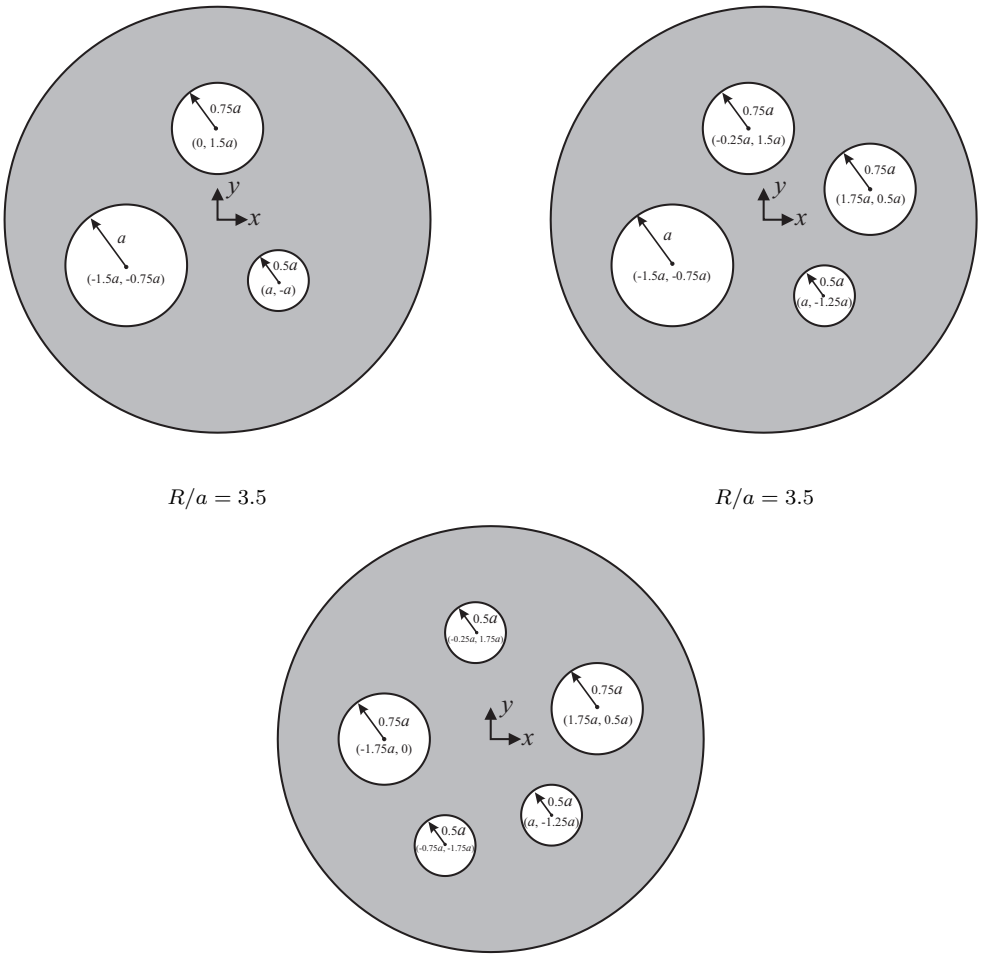

Figure 6.1: Non-uniform distribution of the scatterers with different radii.

6.2 Multiple scattering configurations

Six different configurations are dealt with, in which $3, 4, 5, 6, 8$ and 9 rigid diffracting cylinders are considered. The scatterers are not uniformly distributed and are of different radii in the first three configurations while they are uniformly distributed and of the same radius in the last three configurations. Figures 6.1 and 6.2 show the layout of these examples where the domain outer radius R/a is mentioned for each problem.

A plane wave propagating in the positive x-direction hits the scatterers. The diffracted potential is obtained with the PUFEM using 3-noded elements enriched with 12 plane waves then 6-noded elements enriched with 18 plane waves, for different wave numbers ($ka = 2\pi, 4\pi, 6\pi$ and 8π). Figures 6.3 to 6.8 show the mesh grids used with each configuration. The corresponding number τ of degrees of freedom per wave-

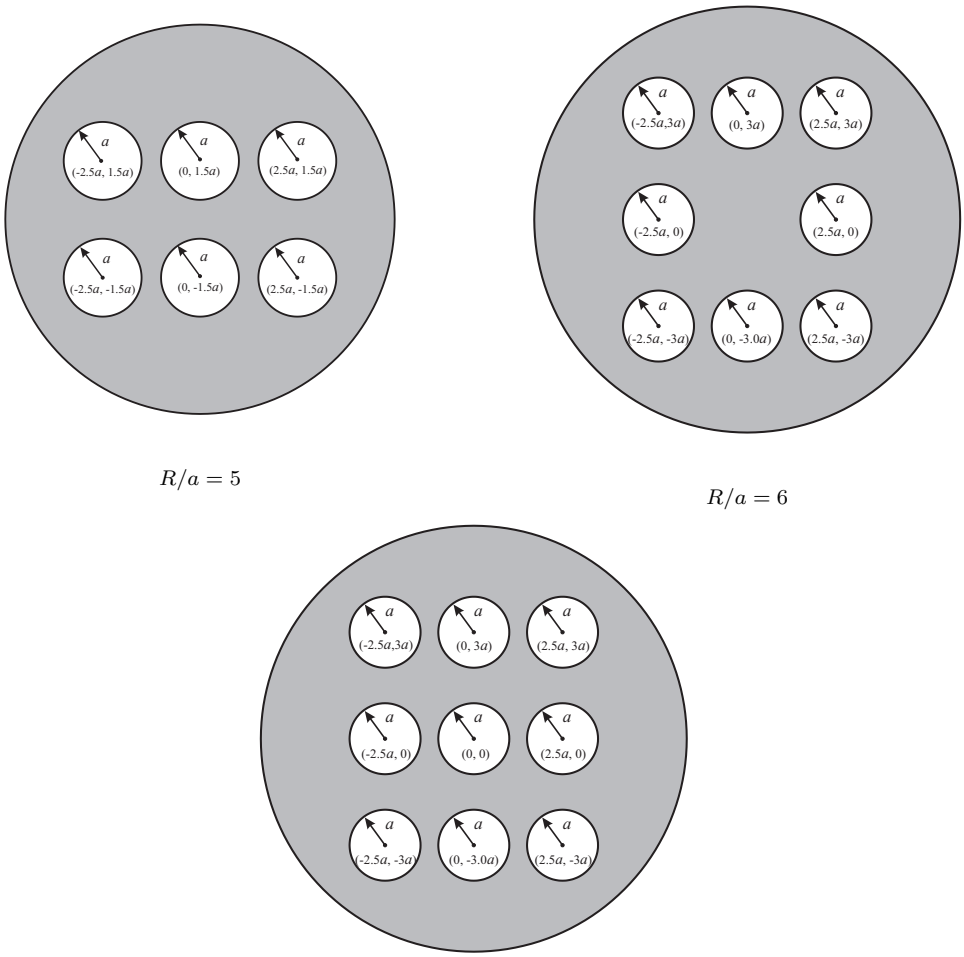

$R/a = 5$

$R/a = 6$

$R/a = 6$

Figure 6.2: Uniform distribution of the scatterers with the same radius.

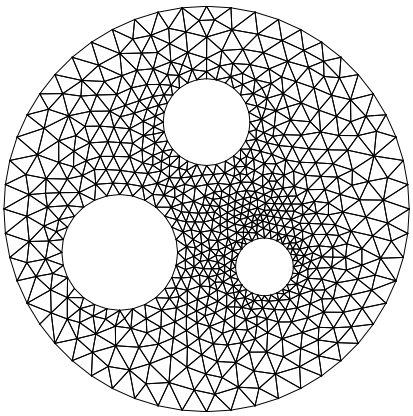

1220 elements, 676 nodes

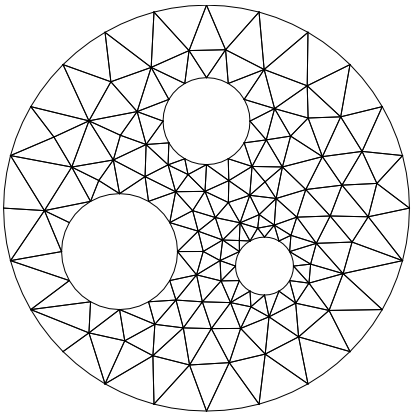

218 elements, 494 nodes

Figure 6.3: Mesh grids for $NC = 3$, (left) 3-noded and (right) 6-noded.

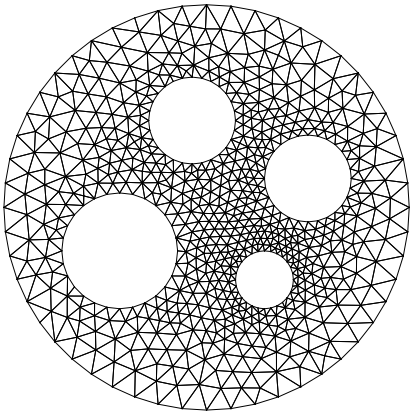

1204 elements, 681 nodes

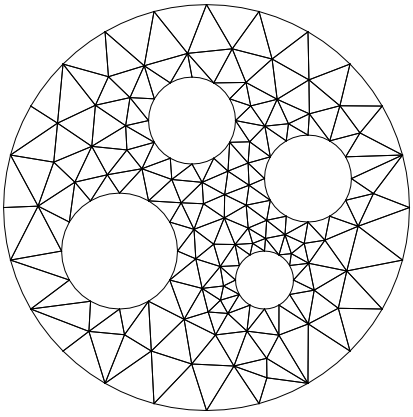

222 elements, 513 nodes

Figure 6.4: Mesh grids for $NC = 4$, (left) 3-noded and (right) 6-noded.

length is given in Tables 6.1 and 6.2. It is clear that τ is high at a low wave number and decreases as the wave number increases. The problems are solved first with the analytical solution applied on the domain boundary through a Robin type boundary condition and then with Neumann and BGT-2 boundary conditions.

The real part of the diffracted potential is plotted in Figures 6.9 and 6.10 for $ka = 4\pi$ and Figures 6.11 and 6.12 for $ka = 8\pi$. The L_2 errors for $ka = 2\pi$, for all the considered configurations and for both types of boundary conditions are listed in Table 6.3. In a similar way for $ka = 4\pi, 6\pi$ and 8π the L_2 errors are listed in Tables 6.4, 6.5 and 6.6, respectively.

For $ka = 2\pi$ and when the analytical solution is applied on the domain boundary a relatively similar error is obtained with 3- or 6-noded elements, however, when

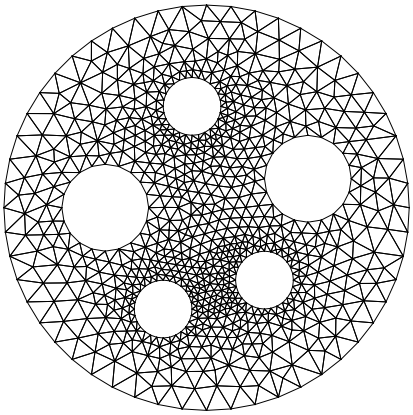

1456 elements, 812 nodes

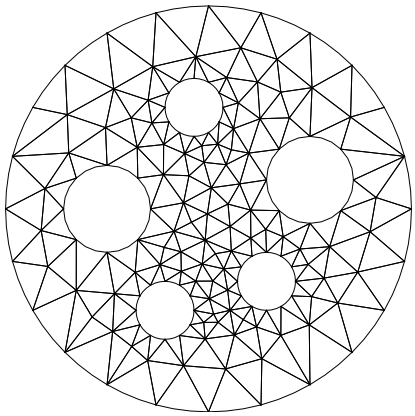

260 elements, 592 nodes

Figure 6.5: Mesh grids for $NC = 5$, (left) 3-noded and (right) 6-noded.

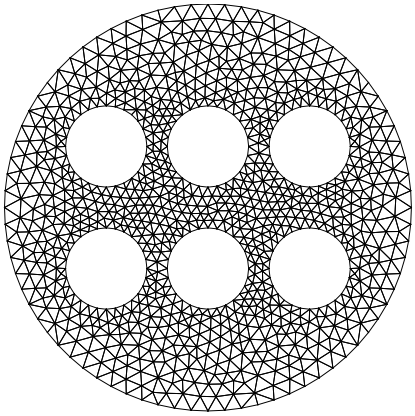

1696 elements, 965 nodes

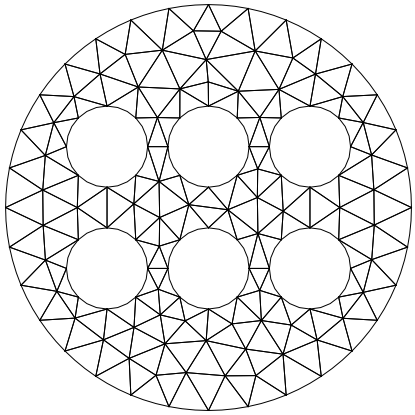

216 elements, 507 nodes

Figure 6.6: Mesh grids for $NC = 6$, (left) 3-noded and (right) 6-noded.

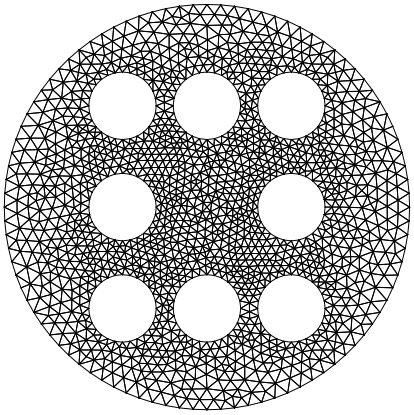

2710 elements, 1506 nodes

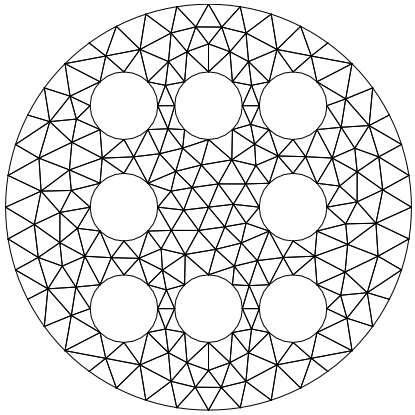

324 elements, 745 nodes

Figure 6.7: Mesh grids for $NC = 8$, (left) 3-noded and (right) 6-noded.

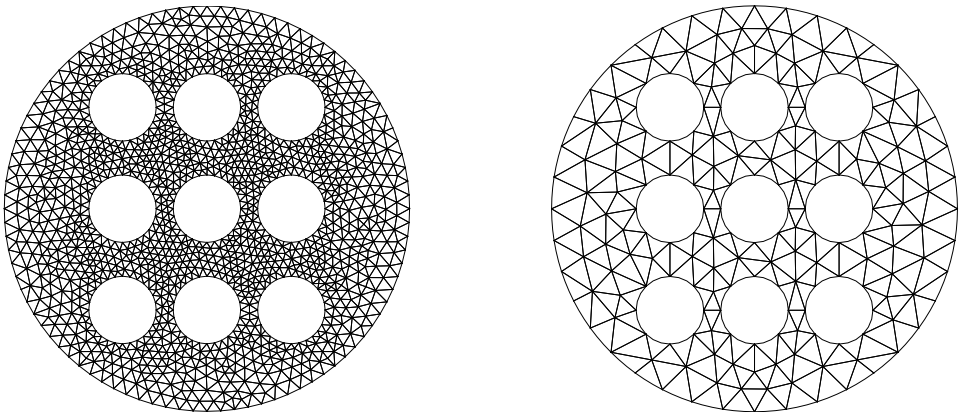

2544 elements, 1436 nodes

308 elements, 720 nodes

Figure 6.8: Mesh grids for $NC = 9$, (left) 3-noded and (right) 6-noded.

ka	$NC = 3$	$NC = 4$	$NC = 5$	$NC = 6$	$NC = 8$	$NC = 6$
2π	15.73	16.23	17.29	13.93	14.33	14.25
4π	7.86	8.12	8.65	6.96	7.17	7.13
6π	5.24	5.41	5.76	4.64	4.78	4.75
8π	3.93	4.06	4.32	3.48	3.58	3.56

Table 6.1: Number τ of DOF/λ for mesh grids with 3-noded elements.

ka	$NC = 3$	$NC = 4$	$NC = 5$	$NC = 6$	$NC = 8$	$NC = 6$
2π	16.47	17.25	18.08	12.36	12.35	12.36
4π	8.23	8.63	9.04	6.18	6.17	6.18
6π	5.49	5.75	6.03	4.12	4.12	4.12
8π	4.12	4.31	4.52	3.09	3.09	3.09

Table 6.2: Number τ of DOF/λ for mesh grids with 6-noded elements.

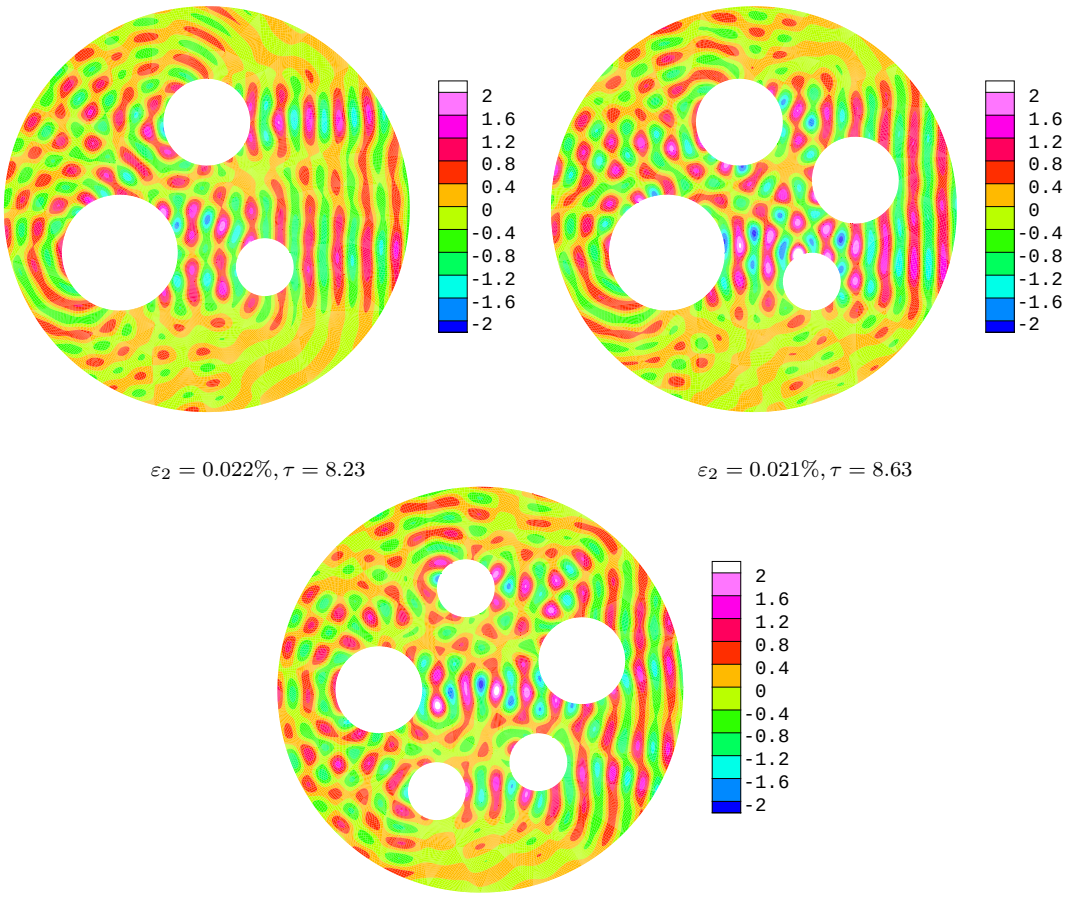

Figure 6.9: Contour plots of the real part of the diffracted potential and the corresponding L_2 errors, $NC = 3, 4$ and 5, $ka = 4\pi$.

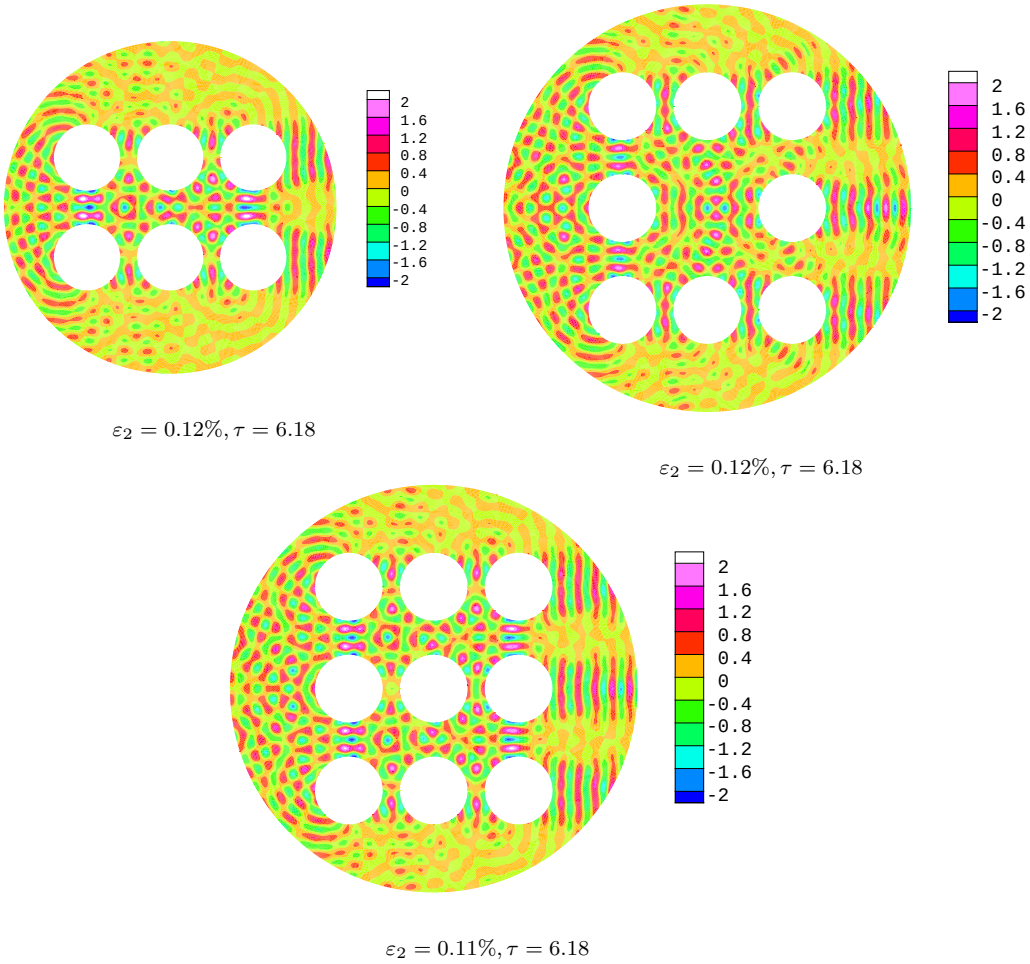

Figure 6.10: Contour plots of the real part of the diffracted potential and the corresponding L_2 errors, $NC = 6, 8$ and 9, $ka = 4\pi$.

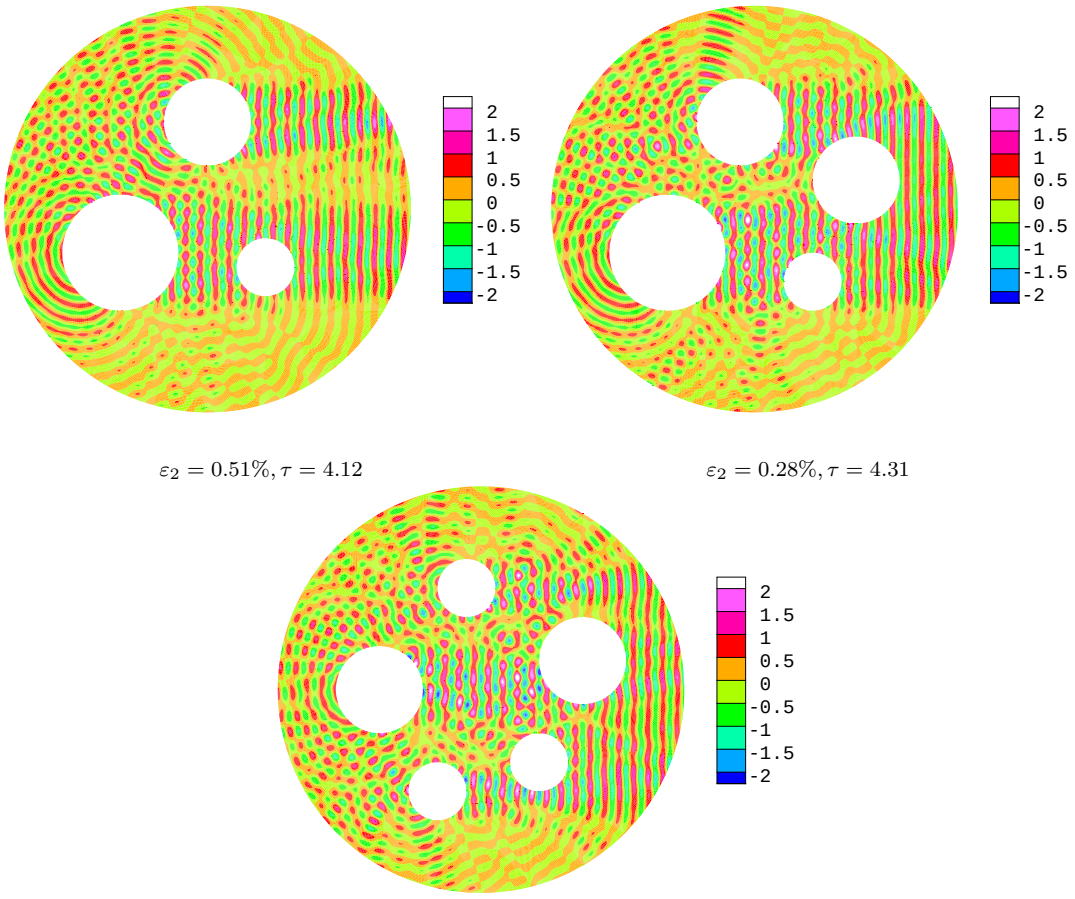

Figure 6.11: Contour plots of the real part of the diffracted potential and the corresponding L_2 errors, $NC = 3, 4$ and 5, $ka = 8\pi$.

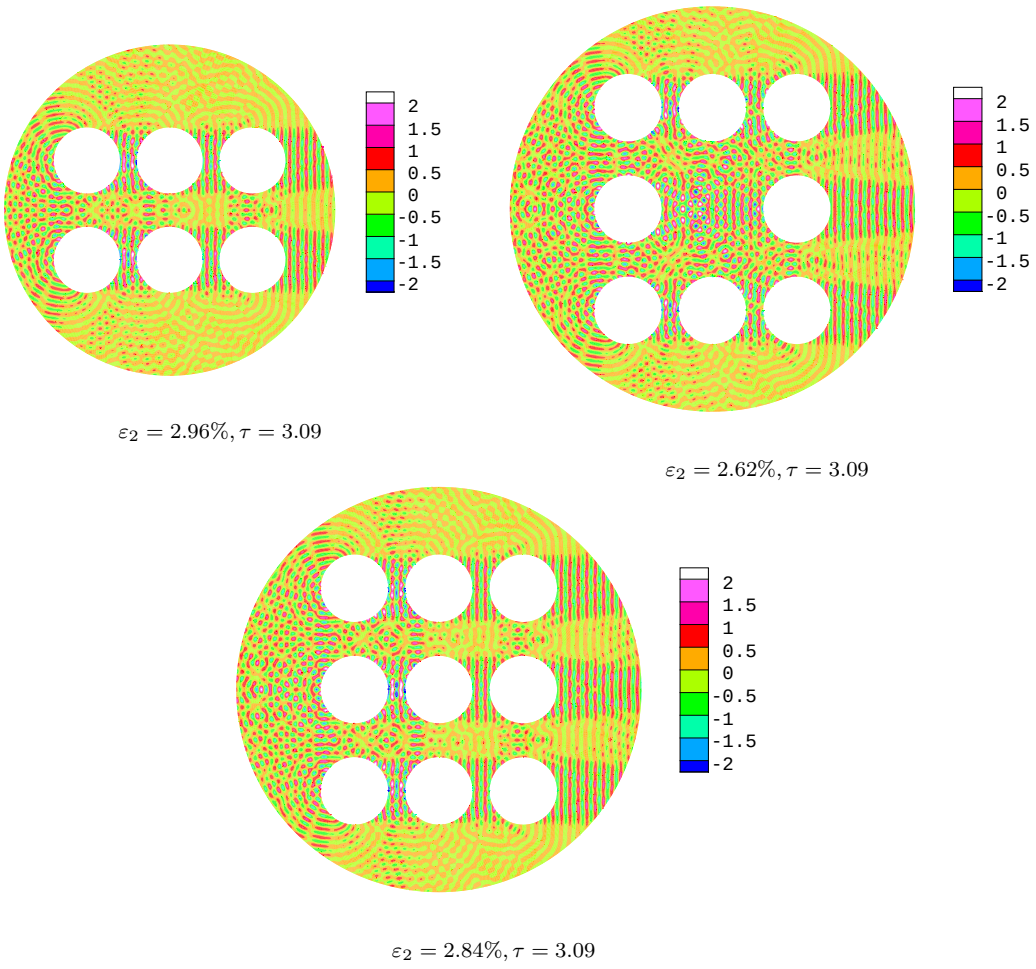

Figure 6.12: Contour plots of the real part of the diffracted potential and the corresponding L_2 errors, $NC = 6, 8$ and 9, $ka = 8\pi$.

	3-noded elements		6-noded elements	
NC	Robin	Neumann/Radiation	Robin	Neumann/Radiation
3	0.028	4.66	0.012	0.97
4	0.074	2.96	0.0092	1.01
5	0.038	6.38	0.039	0.95
6	0.019	7.30	0.063	1.66
8	0.025	10.67	0.060	1.62
9	0.046	8.41	0.063	1.54

Table 6.3: L_2 error, ε_2[%], for different configurations, $ka = 2\pi$.

	3-noded elements		6-noded elements	
NC	Robin	Neumann/Radiation	Robin	Neumann/Radiation
3	0.128	6.62	0.022	1.02
4	0.077	9.15	0.021	0.87
5	0.170	9.73	0.075	0.84
6	0.201	44.14	0.12	8.55
8	0.150	35.59	0.12	4.82
9	0.603	36.21	0.11	6.89

Table 6.4: L_2 error, ε_2[%], for different configurations, $ka = 4\pi$.

	3-noded elements		6-noded elements	
NC	Robin	Neumann/Radiation	Robin	Neumann/Radiation
3	7.49	18.53	0.041	1.05
4	2.32	17.77	0.047	1.00
5	5.87	18.11	0.093	1.08
6	14.29	28.19	0.42	4.21
8	13.33	31.92	0.41	4.56
9	6.26	36.29	0.37	4.98

Table 6.5: L_2 error, ε_2[%], for different configurations, $ka = 6\pi$.

	3-noded elements		6-noded elements	
NC	Robin	Neumann/Radiation	Robin	Neumann/Radiation
3	14.97	29.81	0.51	1.45
4	20.20	57.03	0.28	0.99
5	15.36	24.90	0.37	1.34
6	16.93	37.79	2.96	11.97
8	20.51	47.54	2.62	6.68
9	20.04	42.07	2.84	6.24

Table 6.6: L_2 error, $\varepsilon_2[\%]$, for different configurations, $ka = 8\pi$.

Neumann and BGT-2 are applied the error with 6-noded elements is lower. As the wave number is increased the results with both types of elements start to deteriorate. The error with 6-noded elements remains at acceptable levels except for $ka = 8\pi$ where Neumann and BGT-2 are applied with the configurations 6, 8 and 9. On the other hand, with 3-noded elements the results deteriorate much faster and the error gets to quite large values.

Even though a similar τ is maintained with both elements but the results with the 6-noded elements are of better quality especially at higher wave numbers. This can be due to the quadratic interpolation which describes the circular geometry of the boundary much better than with the linear interpolation. The mesh refinement with the 3-noded elements close to the scatterers does not improve the geometry interpolation enough when shorter wavelengths are considered. Even with the 6-noded elements, the quadratic interpolation becomes inaccurate and leads to poor results at high wave numbers although the considered wave numbers are not too high in these problems.

To achieve a good geometry simulation the size of the elements needs to be small enough compared to the wavelength. Since the PUFEM performs well with large elements then a combination of large and small elements becomes necessary. However, using such a combination where all the elements are enriched with the same number of plane waves could create conditioning problems. This will be discussed further in the next Chapter.

6.3 Conclusion

In this Chapter, the multiple scattering problem involving circular rigid scatterers and its solution with the PUFEM was presented. Different configurations are considered with two types of elements and with artificial boundary conditions or with the analytical solution applied on the domain boundary.

The results show the ability of the PUFEM to solve multiple scattering problems with large elements compared to the wavelength. But as mentioned in the previous Chapter, the geometry description is crucial as the wavelength becomes smaller. Therefore, when using straight edge finite elements, it is needed to refine the mesh grid around the scatterers to better describe the curved boundaries. Having both large and small elements within a mesh grid requires an adaptive approach in the enrichment process in order to avoid further ill-conditioning if the same number of approximating plane waves is used. This is explored in the next Chapter.

Chapter 7

Adaptive plane wave enrichment

In Chapter 4, it was shown that interpolating the circular geometry of the scatterers with polynomial shape functions induces some error into the PUFEM solution. A classical approach to reduce this error is to refine the mesh near the curved geometry. But because the wavelength may be much smaller than the scatterer characteristic size, the elements should be fine enough to describe the geometry smoothly relative to the wavelength.

Keeping the elements close to the curved boundaries fine while meshing most of the domain with multi-wavelength sized elements, is highly desirable in short wave problems. However, another problem arises from this variation in the element sizes, which leads to an increase of the condition number due to enriching the solution space with a constant number of plane waves.

In this Chapter, the advantages and the limitations of mesh grids containing both small and large elements, are discussed using two examples. Then it is proposed to enrich the solution space with a number m_j of plane waves which varies in the problem domain such that the number τ of degrees of freedom per wavelength is kept practically constant over the whole computational domain. This is shown for scattering problems where uniform and non-uniform mesh grids are used. The results obtained with both variable and constant numbers of enriching plane waves are compared based on the error and the conditioning.

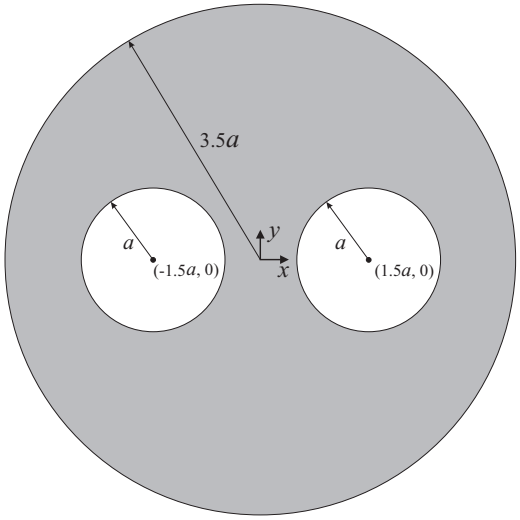

Figure 7.1: Two-scatterer problem outline.

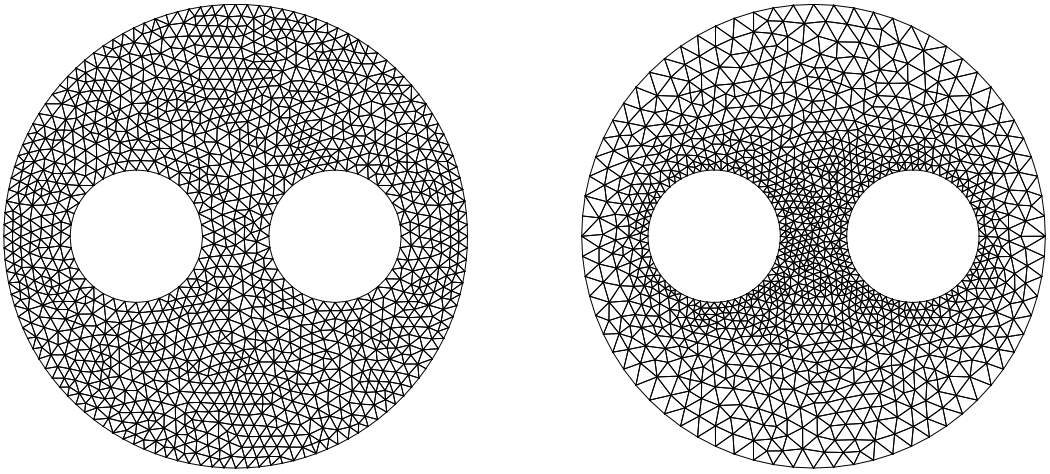

(i) 2432 elements, 1313 nodes

(j) 2330 elements, 1260 nodes

Figure 7.2: Two-scatterer problem: (left) uniform and (right) non-uniform mesh grids.

7.1 Non-uniform mesh grids

7.1.1 Example 1

A two-scatterer problem shown in Figure 7.1 is solved for the wave number $ka = 6\pi$ where Neumann and BGT-2 boundary conditions are applied on the scatterers and the outer boundary, respectively. The PUFEM solution is obtained with the computational domain meshed into 3-noded elements of the same size (Figure 7.2, mesh (i)) where the solution space is enriched with 12 plane waves.

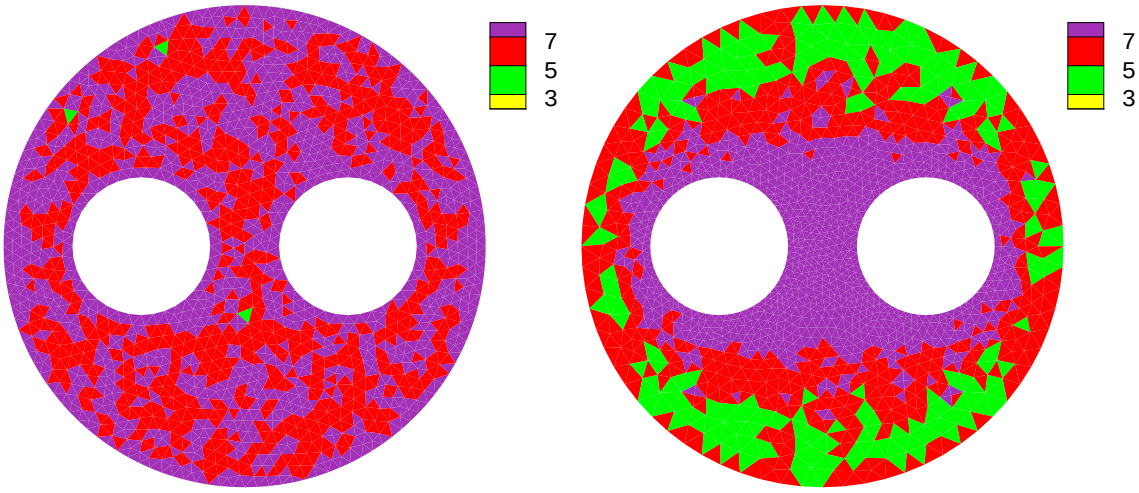

mesh (i) $\tau_{min} = 4.95$, $\tau_{max} = 11.97$, $\tau = 7.37$ mesh (j) $\tau_{min} = 3.47$, $\tau_{max} = 20.48$, $\tau = 7.28$

Figure 7.3: Two-scatterer problem: variation in τ with (left) uniform and (right) non-uniform mesh grids.

Despite the relatively high number of degrees of freedom per wavelength, $\tau = 7.37$, the L_2 error is too high $\varepsilon_2 = 8.4\%$. This is partially induced by the interpolated geometry and could be improved by refining the mesh around the scattering cylinder.

In mesh (i) the average element size is $h/a \approx 0.17$. To improve this, the area around the scatterers is re-meshed into elements of size $h/a = 0.1$ (Figure 7.2, mesh (j)), which increases the number of nodal points around each scatterer from 36 in the uniform mesh to 63 in the new mesh. The number of enriching plane waves is kept unchanged as before. To keep the results comparable, the number of elements is kept relatively the same with both mesh grids by considering larger elements $h/a = 0.3$ in mesh (j) near the outer boundary while gradually varying the elements inside the domain between $h/a = 0.1$ and 0.3. The number of elements in the new mesh is 2330 while it was 2432 in the previous one.

Although the outer boundary has fewer nodal spaces compared to the previous mesh grid but the L_2 error with the new mesh grid is improved to $\varepsilon_2 = 2.5\%$. This shows that the increase in the number of nodal points close to the scatterer helped to improve the geometry interpolation thus improved the error.

The average number of degrees of freedom per wavelength with the new mesh grid is similar to the previous one, $\tau \approx 7.3$. However, with mesh (j) the parameter τ varies from 3.47 close to the outer boundary to 20.48 close to the scatterers while with mesh (i) it varied between 4.95 and 11.97 (Figure 7.3). The higher value of τ

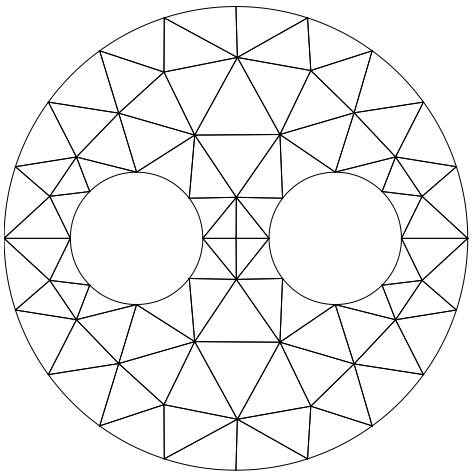

(h)

88 elements, 211 nodes

Figure 7.4: Two-scatterer problem: 6-noded mesh.

with mesh (j) obviously affects the conditioning, hence it is possible to improve the error further by reducing the high value of local τ by considering a reduction in the number of plane waves close to the scatterers.

The previous results show an error improvement for a better distribution of the elements. This is investigated further by solving the problem again for the wave numbers $ka = 8\pi$. The corresponding errors for this wave number are, respectively, 9.98% with mesh (i) and 5.72% with mesh (j). Despite the previous refinement considered with mesh (j) but at a higher wave number the results seems to be affected by the interpolated geometry and a further refinement of the mesh may be necessary. To expose the error due to the interpolated geometry, next, the previous problem is resolved using quadratic elements.

The problem is solved again for the above two wave numbers but using 6-noded elements (Figure 7.4, mesh (h)) where second order polynomials are used to interpolate the curved geometry of the problem. The number of plane waves enriching the solution space is increased to $m = 24$. In fact, in the PUFEM, as stated before it is more suitable to have large elements with high number of enriching plane waves. The numbers of degrees of freedom per wavelength become $\tau = 5.06$ and 3.80 for $ka = 6\pi$ and 8π, respectively, while the corresponding errors are 1.54% and 2.91%.

It should be noted that the distance between the scatterers and the outer boundary is only one unit of length at the most right and left points of the computational

domain which is relatively small compared to the scatterers size. Therefore BGT-2 boundary condition has a major contribution to the error as well, which explains the relatively large error in this example (see reference [99]). To reduce this error, one may consider a larger computational domain which will significantly increase the number of elements making the example computationally expensive. Another approach consists to apply the analytical solution on the domain boundaries. However this approach is not possible for real world problems.

7.1.2 Example 2

The eight-scatterer problem found in Chapter 6, with $ka = 8\pi$ and Robin boundary condition is reconsidered for this example. The domain outer boundary is taken to be straight lines. First the domain is meshed with elements of the same size (Figure 7.5, mesh (k)). Then areas close to the outer boundary and the domain central area are meshed with relatively large elements while other areas are meshed with elements of the same size as in the previous mesh (Figure 7.5, mesh (l)). Although the non-uniform mesh has larger elements compared to the uniform one but, close to the curved geometry, both mesh grids have the same element size i.e. the geometry is described similarly with both mesh grids. Because mesh (l) has fewer elements compared to mesh (k), the non-uniform mesh is enriched with 24 plane waves while the uniform one is enriched with 14 to achieve the same τ with both mesh grids, that is $\tau = 5.01$.

Using mesh (k), the numerical solution of the diffracted potential is obtained with an error $\varepsilon_2 = 0.99\%$. This error is increased to $\varepsilon_2 = 1.60\%$ with mesh (l). Although the average value of τ is the same with both mesh grids and mesh (l) has the advantage of large elements enriched with high number of plane waves but the error with mesh (k) is smaller. To explain this, one may examine τ and how it varies within the problem domain. If the local value of τ is considered, one may notice that τ varies with mesh (l) from $\tau_{max} = 9.68$ close to the scatterers to $\tau_{min} = 2.33$ in the central area while in mesh (k) it varies between 8.36 and 3.21 (Figure 7.6). Clearly the minimum local value of τ with mesh (l) falls below 2.5 which causes this increase in the error. In other words with a constant number of enriching plane waves, the variation in the element size leads to an accuracy which is influenced by the smallest

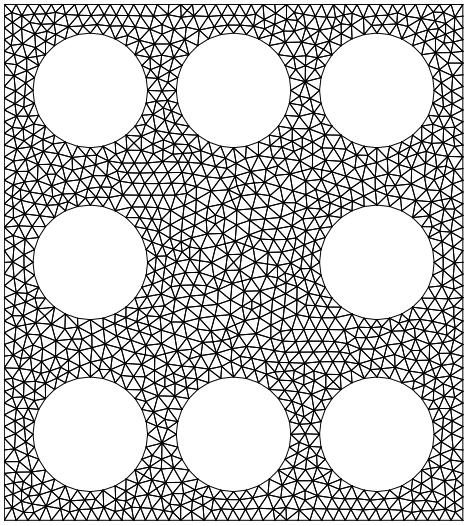

(k) 2322 elements, 1349 nodes

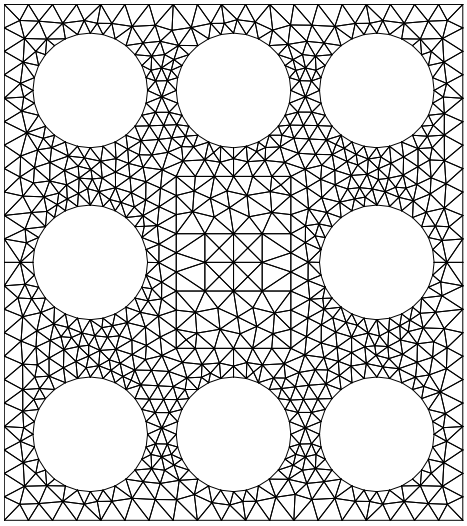

(l) 1286 elements, 789 nodes

Figure 7.5: Eight-scatterer problem: (left) uniform mesh grid, (right) non-uniform mesh grid.

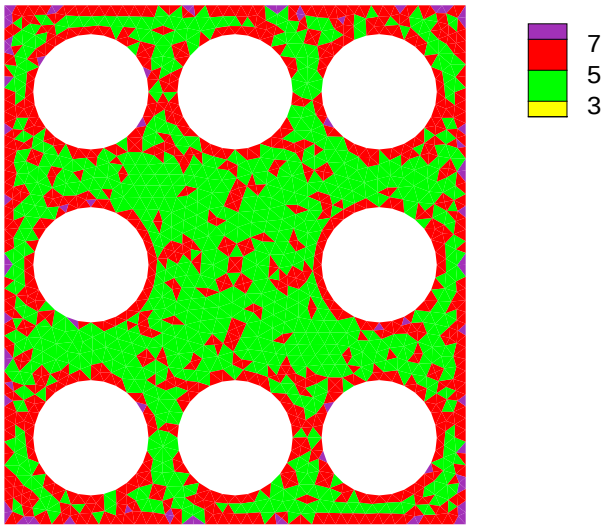

$\tau = 5.01$, $\tau_{min} = 3.21$ and $\tau_{max} = 8.36$

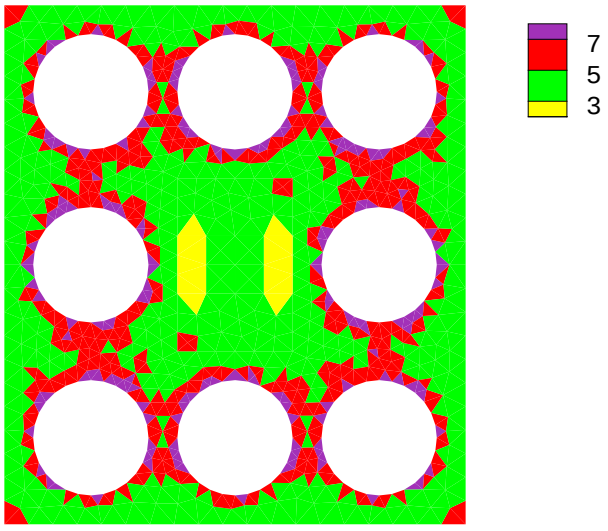

$\tau = 5.01$, $\tau_{min} = 2.33$ and $\tau_{max} = 9.68$

Figure 7.6: Eight-scatterer problem: local values of τ over the computational domain.

local value of τ.

One can see how varying the element size caused a reduction in the lowest value of τ which in turn reduces the accuracy. To overcome this, it is possible to assign more plane waves to the nodes of the large elements and less plane waves to the nodes of the small elements so that the local values of local τ are kept around a suitable value.

7.2 Variable number of enriching plane waves

In this section, it is proposed to take the number m_j of plane waves at a node j to be dependent on the longest edge h_j^{max} connected to this node. As a consequence, the elementary matrices will be of different sizes depending on the number of enriching plane waves. If the difference between the minimum and maximum m_j becomes too large the block corresponding to the maximum m_j will have a dominant effect on the results compared to smaller blocks. Such a case shall be avoided here. To achieve this, the relationship between h_j^{max} and m_j must be nonlinear such that the value of m_j grows quickly at smaller h_j^{max} and slowly at higher h_j^{max}. A similar nonlinear relationship may be found in reference [64].

$$m_j = round[kh_j^{max} + C(kh_j^{max})^{\frac{1}{3}}] \tag{7.1}$$

where C is a constant. For a considered mesh grid and a fixed wave number, in order to increase the number m_j, the value of C is increased such that $C = 3, 4, ..., 12$. It should be mentioned that the number of basis function calculated using this formula is based on the error analysis of truncation of the Jacobi-Anger expansion performed in the context of the multipole method for wave scattering problems [119]. The formula was used, without a rigorous mathematical analysis, in the PUFEM and the UWVF [64]. Because the aim here is to investigate the effect of a variable m_j rather than finding an optimum strategy to define it, this formula is considered to be satisfactory. Other strategies to define m_j may be found in reference [80].

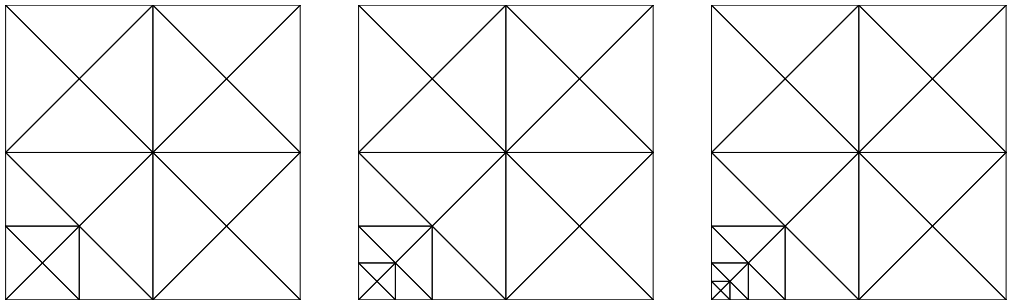

(m) 20 elements, 16 nodes (n) 24 elements, 19 nodes (o) 28 elements, 22 nodes

Figure 7.7: Mono scattering problem: mesh refinement at one corner.

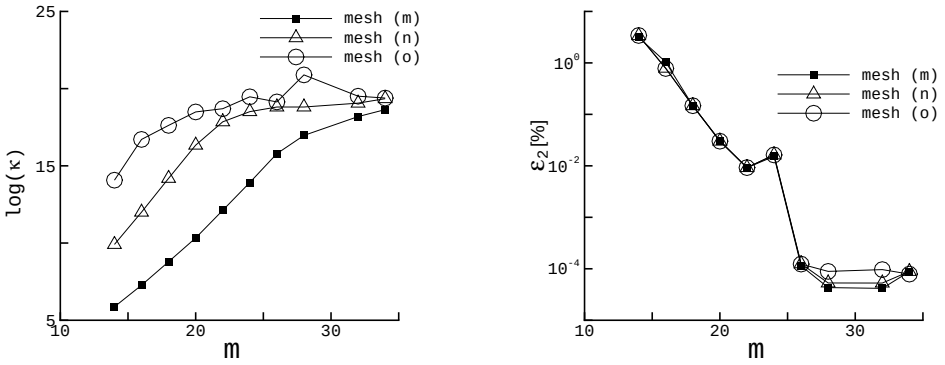

Figure 7.8: Mono scattering problem: results obtained with a constant m, $ka = 4\pi$.

7.3 Uniform versus non-uniform distribution of plane waves

The mono scattering problem of Chapter 3 is reconsidered and the computational domain is redefined as $(1,1) \leq (x,y) \leq (3,3)$. The domain is meshed into 14 triangular elements of the same size covering 87.5% of the computational domain area. The remaining 12.5% at one corner is meshed into 6 then 10 and finally 14 smaller elements. The resulting three mesh grids are shown in Figure 7.7.

The problem is solved for the wave number $ka = 4\pi$ using the three mesh grids where the solution space is enriched with a constant number of plane waves then with a variable number m_j calculated using expression (7.1). The solution is repeated with the number of plane waves being increased each time until the error stops improving.

The L_2 error corresponding to the results obtained with a constant m for the three considered mesh grids is plotted in Figure 7.8 alongside with the corresponding con-

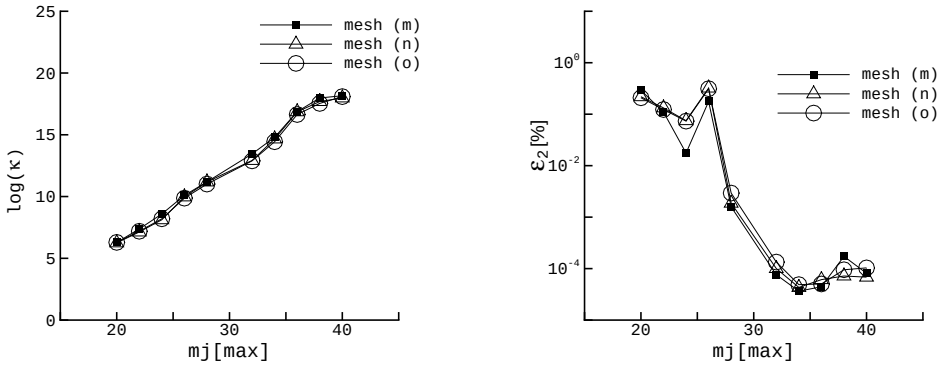

Figure 7.9: Mono scattering problem: results obtained with a variable m_j, $ka = 4\pi$.

dition number while Figure 7.9 displays similar plots for a variable m_j. These figures show that the L_2 error does not improve when refining the mesh at one corner with either a constant or a variable number of plane waves. On the other hand refining the mesh at one part with a constant m leads to a further increase in the condition number. This does not seem to affect the solution with a variable m_j where the results show no significant change in the conditioning.

The above observations may well be linked to the maximum and minimum local numbers of degrees of freedom per wavelength, τ_{max} and τ_{min}. Tables 7.1 and 7.2 show the values of τ corresponding to Figures 7.8 and 7.9, respectively. It could be observed from Table 7.1, where a constant m is considered, that τ_{min} does not increase with a finer mesh ($\tau_{min} = 2.75$ for $m = 14$ with all three mesh grids) while τ_{max} increases quite fast ($\tau_{max} = 7.79, 15.58$ and 31.16 for $m = 14$ with mesh grids (m), (n) and (o), respectively). A similar observation may be made when a variable number m_j is used but here τ_{max} increases in a slower way compared to the constant m case ($\tau_{max} = 7.07, 11.43$ and 19.6 for $m_j = 14$ with meshes (m), (n) and (o), respectively).

The previous tables may explain the behaviour of the L_2 error and the condition number. It was observed in Chapter 3 that τ influences the error and the conditioning. The error is influenced by the smallest value of τ. By refining one part of the considered mesh, τ_{min} does not change thus the L_2 error does not improve. On the other hand the conditioning is mostly affected by the highest value of τ. With a constant m, refining the mesh leads to a fast-growing τ_{max} which could explain the large increase of the condition number. With a variable m_j, the increase in τ_{max}

is relatively small which may be the reason why the conditioning does not change significantly.

	τ_{min}			τ_{max}		
m	mesh (m)	mesh (n)	mesh (o)	mesh (m)	mesh (n)	mesh (o)
14	2.75	2.75	2.75	7.79	15.58	31.16
16	2.94	2.94	2.94	8.33	16.65	33.31
18	3.12	3.12	3.12	8.83	17.66	35.33
20	3.29	3.29	3.29	9.31	18.82	37.24
22	3.45	3.45	3.45	9.76	19.53	39.06
24	3.61	3.61	3.61	10.20	20.40	40.79
26	3.75	3.75	3.75	10.61	21.23	42.46
28	3.89	3.89	3.89	11.02	22.03	44.06
32	4.16	4.16	4.16	11.78	23.55	47.10
34	4.29	4.29	4.29	12.14	24.28	48.55

Table 7.1: Maximum and minimum values of τ for a constant m, $ka = 4\pi$.

	τ_{min}			τ_{max}		
m_j^{max}	mesh (m)	mesh (n)	mesh (o)	mesh (m)	mesh (n)	mesh (o)
20	3.19	3.19	3.19	7.07	11.43	19.60
22	3.35	3.35	3.35	7.66	11.78	20.40
24	3.51	3.51	3.51	8.08	12.86	22.86
26	3.66	3.66	3.66	8.60	14.14	23.55
28	3.81	3.81	3.81	9.09	15.32	25.72
32	4.04	4.04	4.04	9.56	15.32	26.33
34	4.17	4.17	4.17	9.66	16.41	28.28
36	4.30	4.30	4.30	10.00	17.44	30.64
38	4.43	4.43	4.43	10.42	18.18	30.64
40	4.55	4.55	4.55	10.83	18.40	32.82

Table 7.2: Maximum and minimum values of τ for a variable m_j, $ka = 4\pi$.

In the second part of the numerical tests, the problem is solved for the wave numbers

$ka = 12\pi, 20\pi$ and 28π using mesh (n). Table 7.3 shows a comparison of the results obtained with a constant m and then with a variable m_j based on the total number of degrees of freedom, $totdof$, the L_2 error and the condition number.

	constant m				variable m_j			
ka	$totdof$	$totsys$	$\varepsilon_2[\%]$	$log(\kappa)$	$totdof$	$totsys$	$\varepsilon_2[\%]$	$log(\kappa)$
12π	912	308040	0.36	18.60	886	285349	0.012	11.94
12π	988	361478	0.015	18.74	924	310438	0.011	13.17
12π	1026	389799	0.0046	18.69	986	354159	0.00085	15.79
12π	1102	449645	0.00039	18.53	1046	397137	0.000017	17.13
12π	1178	513763	0.00015	19.09	1092	434230	0.000094	17.75
20π	1406	731749	0.44	18.63	1278	593501	0.090	13.04
20π	1482	812955	0.40	18.74	1332	644126	0.034	15.03
20π	1558	898433	0.048	18.97	1402	714099	0.0094	16.55
20π	1634	988183	0.0087	19.05	1464	779668	0.0034	16.90
20π	1710	1082205	0.0018	18.60	1538	859907	0.00027	17.33
28π	1938	1389903	0.23	18.53	1810	1189099	0.060	17.25
28π	2014	1501013	0.52	19.11	1876	1278214	0.0082	17.13
28π	2090	1616395	0.054	18.91	1942	1370933	0.0059	17.25
28π	2166	1736049	0.033	18.98	2030	1497417	0.00091	17.70
28π	2280	1923540	0.0019	18.88	2098	1598979	0.00059	18.60

Table 7.3: Comparison of the results obtained with a constant m or a variable m_j, mesh (n).

Table 7.3 shows that with a variable m_j a smaller $totdof$, compared to a constant m, leads to an error one order of magnitude lower. With a constant m the condition number is higher than 10^{18} for all the entries of the table including for $totdof = 912$ which corresponds to the smallest considered number of enriching plane waves, $m_j = 48$. However, with a variable m_j the condition number does not get this high until the last entry of the table, where $totdof = 2098$, which corresponds to $m_j^{max} = 146$. This shows the possibility of increasing the number of enriching plane waves while

	constant m				variable m_j			
ka	$totdof$	$totsys$	$\varepsilon_2[\%]$	$log(\kappa)$	$totdof$	$totsys$	$\varepsilon_2[\%]$	$log(\kappa)$
12π	1056	376080	0.38	18.85	852	243378	0.065	10.03
12π	1144	441324	0.015	19.24	924	286750	0.0091	12.04
12π	1188	475902	0.0058	19.27	1034	358567	0.00053	15.15
12π	1276	548970	0.00023	19.57	1152	444828	0.000075	17.53
12π	1364	627254	0.00011	19.43	1206	486233	0.000048	17.48
20π	1716	992550	0.20	19.82	1328	593884	0.092	13.06
20π	1804	1096914	0.050	18.95	1464	719128	0.0068	16.38
20π	1892	1206494	0.0081	19.15	1532	788454	0.0015	16.98
20π	1980	1321290	0.0024	18.88	1610	869203	0.00018	17.63
20π	2068	1441302	0.00032	19.63	1740	1013470	0.000090	18.51
28π	2420	1973510	0.18	19.18	1884	1192506	0.075	16.33
28π	2508	2119602	0.030	18.87	1956	1286330	0.0059	17.17
28π	2640	2348520	0.0025	19.46	2194	1614755	0.00023	18.29
28π	2728	2507652	0.0016	19.55	2272	1729464	0.00052	18.49
28π	2816	2672000	0.0013	19.64	2340	1836126	0.0011	18.62

Table 7.4: Comparison of the results obtained with a constant m or a variable m_j, mesh (o).

keeping the condition number relatively low.

The previous calculations are further extended by considering mesh (o). The new set of results, displayed in Table 7.4, show similar patterns as the previous ones. However, with a variable m_j the condition number increases faster than before. This may be expected as the elements in the refined part of the mesh become too small compared to the large elements of the mesh and to the considered wavelengths. If a further refinement is to be considered it will be difficult to attach enough enriching plane waves to the nodes in the finer parts while keeping the condition number low. In such a situation the approach of varying the number of plane waves will become less effective. However, in the case of mesh (o) the area of the smallest element is

	constant m				variable m_j			
ka	$totdof$	$totsys$	$\varepsilon_2[\%]$	$log(\kappa)$	$totdof$	$totsys$	$\varepsilon_2[\%]$	$log(\kappa)$
12π	1628	1002694	0.30	19.01	1186	515203	0.051	9.16
12π	1776	1193208	0.051	18.97	1368	689308	0.0026	12.05
12π	1850	1294675	0.00067	18.94	1460	785826	0.00028	14.05
12π	1924	1400282	0.00017	19.29	1568	905328	0.000051	16.52
12π	1998	1510029	0.000025	19.35	1650	1005115	0.000014	17.41
20π	2368	2120864	1.82	18.78	1710	1070261	0.31	9.11
20π	2442	2255451	0.83	18.88	1926	1359533	0.050	12.73
20π	2738	2835199	0.017	19.20	2050	1545099	0.0016	14.06
20π	2886	3149913	0.0011	19.21	2282	1914647	0.00019	17.43
20π	3034	3481187	0.00022	19.07	2382	2088309	0.000093	18.03
28π	3330	4193415	0.66	18.97	2218	1801379	0.48	9.39
28π	3478	4574369	0.19	18.84	2360	2037156	0.081	11.44
28π	3626	4971883	0.021	19.19	2608	2492488	0.0011	15.33
28π	3922	5816591	0.00093	19.19	2824	2931020	0.00039	17.62
28π	4070	6263785	0.00034	19.15	2966	3232953	0.00053	17.85

Table 7.5: Comparison of the results obtained with a constant m or a variable m_j, mesh (p).

less than 2% of the area of the largest element, with the approach of varying m_j still being effective.

In the previous calculations only one corner of the computational domain is re-meshed into finer elements. Similar calculations are performed but with all four corners being re-meshed. The resulting mesh grid consists of eight 3-noded elements of the same size covering 50% of the domain central area, while the other 50% is meshed into smaller elements (Figure 7.10, mesh (p)).

The problem is solved again with the new mesh grid using a constant m and then a variable m_j. The L_2 error and the condition number are displayed in Table 7.5. The results show, in the case of a variable m_j, a lower error and a smaller condition

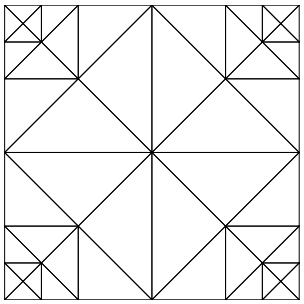

(p) 48 elements, 37 nodes

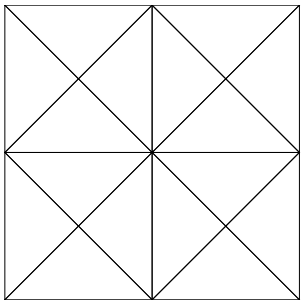

(q) 16 elements, 13 nodes

Figure 7.10: Mono scattering: Uniform (left) and non-uniform (right) mesh grids.

number with *totdof* being 20% lower than with a constant m. This confirms the previous conclusions.

	mesh (q)-constant m				mesh (p)-variable m_j			
ka	*totdof*	*totsys*	ε_2[%]	$log(\kappa)$	*totdof*	*totsys*	ε_2[%]	$log(\kappa)$
12π	676	177450	0.061	9.32	1186	515203	0.051	9.17
12π	702	191349	0.0087	10.43	1368	689308	0.0026	12.05
12π	754	220719	0.0007	11.93	1460	785826	0.00028	14.05
12π	832	268704	0.000063	15.37	1650	1005115	0.000014	17.41
20π	1014	399009	0.48	10.02	1710	1070261	0.31	9.10
20π	1118	484997	0.03	12.32	1842	1244135	0.02	11.37
20π	1170	531135	0.0022	13.40	2050	1545099	0.0016	14.06
20π	1222	579369	0.00061	15.16	2282	1914647	0.00019	17.43
28π	1378	736647	0.26	10.90	2218	1801379	0.48	9.39
28π	1430	793265	0.12	11.89	2468	2233090	0.014	12.89
28π	1560	943980	0.0057	15.16	2608	2492488	0.0011	15.33
28π	1612	1007934	0.0067	16.28	2824	2931020	0.00039	17.62

Table 7.6: Comparison of the results obtained with a constant to a variable m_j, meshes (p) and (q).

In the last part of the numerical tests, the results obtained with a non-uniform mesh and a variable m_j are compared to a uniform mesh and a constant m. The previous calculations are repeated with mesh grid (q) of Figure 7.10 and using a constant m.

The results are compared in Table 7.6 to the results of mesh (p) using a variable m_j. As expected, using a uniform mesh and a constant m has a great advantage over a non-uniform mesh and a variable m_j. The comparison shows that, in order to achieve the same order of error, the double of $totdof$ is required with mesh (p) compared to mesh (q). However, the difference in the condition number is relatively small with both mesh grids. This leads us to conclude that considering uniform mesh grids with large elements and a constant m is the best choice. If non-uniform mesh grids are required then a variable m_j would also lead to good quality results.

7.4 Conclusion

It is shown in this chapter that uniform mesh grids with a constant number of enriching plane waves lead to very good performance of the PUFEM. In this case, the average number of degrees of freedom per wavelength is constant throughout the whole computational domain.

But when problems involve geometry curvatures, it is necessary to have non-uniform mesh grids such that sufficiently small-size elements are used to reflect the geometry details. If a constant number of enriching plane waves is used with this type of mesh grids then the number τ of degrees of freedom per wavelength will vary throughout the domain.

In fact the average value of τ within the whole computational domain may be desirable but locally it will be too high around small-size elements, which may lead to poor conditioning, and low within large elements which may affect the solution quality.

For non-uniform mesh grids, it is practical to adapt the number of enriching plane waves as a function of the mesh size so that it is decreased at the nodes of finer elements and increased for the coarse elements. It is shown that this improves the conditioning and significantly reduces the required total number of degrees of freedom, in comparison to cases where constant numbers of enriching plane waves are used.

In the next chapter, the implementation of an iterative solver for the solution of the

PUFEM linear system is discussed. In order to improve its convergence preconditioners are also used.

Chapter 8

Iterative solution with preconditioning

In the previous chapters, to solve the resulting PUFEM system of equations, direct solvers were used. This was possible due to the relatively small size of the systems that have been considered so far. However, the computational cost of these solvers is of the order $\mathcal{O}(n_{tot}^3)$ which could be prohibitively expensive with large systems such as in three-dimensional problems. The same cost with iterative solvers is of the order $\mathcal{O}(n_{tot}^2)$ per iteration, hence, if the number of iterations, $iter$, is much smaller than the system size, n_{tot}, then iterative solvers become more attractive compared to the direct ones [120, 121].

As shown in Chapter 4, the system matrix resulting from the PUFEM is complex valued and symmetric when the unconjugated formulation is used. Therefore it requires general iterative approaches working for non-Hermitian matrices such as the Generalized Minimum Residual method (GMRES) [122] or the Quasi-Minimal Residual method (QMR) [123]. Because of the conditioning problem of the PUFEM the choice of an appropriate preconditioner becomes particularly important for the convergence acceleration of the considered solver.

In this Chapter, an iterative solver is used for the solution of the linear system. The PUFEM linear system is usually less sparse compared to the FEM one. Taking this into account, a suitable solver is suggested and in order to improve the convergence it is proposed to solve the system after transforming it into a wavelet space.

8.1 Properties of the PUFEM linear system

The following example highlights an important difference, with respect to the system matrix, between the PUFEM and the FEM.

A problem of the layout defined in Example 1, Chapter 7, is reconsidered with $ka = 20\pi$. The computational domain is the unit square $(-0.5, -0.5) \leq (x/a, y/a) \leq (0.5, 0.5)$ with the analytical solution applied on the domain boundary through a Robin type boundary condition. The numerical solution is obtained using seven structured mesh grids, similar to the ones considered in Chapter 3, containing 128, 98, 72, 50, 32, 18 and 8 triangular linear elements. For each mesh grid the number of enriching plane waves is chosen such that the number of degrees of freedom per wavelength, τ, is around 3.

Table 8.1 shows the accuracy of the results for a growing mesh size h/a and an increasing number m of approximating plane waves while the total number of degrees of freedom, $totdof$, and the number τ of degrees of freedom per wavelength are kept practically unchanged, $totdof \approx 900$ and $\tau \approx 3$. The number $totsys$ of storage locations needed for the solution of the linear system is listed in the table as well.

Although τ and $totdof$ remain unchanged, the results show that the accuracy of the PUFEM keeps improving when the size of the element and the number of enriching plane waves are increased. This is expected because of the good approximation properties of the plane waves. A similar observation was made in Chapter 3. Another important remark concerns $totdof$ which remains practically unchanged while $totsys$ and the condition number κ increase dramatically with the number m of enriching plane waves. This means that the coefficient matrix remains of the same size as $totdof$ does not change but it becomes denser as $totsys$ increases with an increasing m. To clarify this, one may note that the plane waves are shared degrees of freedom among the elements. The increase in the number of plane waves leads to larger element matrices, which leads to a system matrix of unchanged size but with a growing population.

In the PUFEM, larger elements in comparison to the wavelength with high numbers of enriching plane waves lead to very good performance of the method. Thus the system matrix is likely to become dense if compared to a matrix resulting from the

m	h/a	τ	totdof	totsys	$\varepsilon_2[\%]$	$\log \kappa$
12	$\sqrt{2}/8$	3.12	972	109998	8.31%	4.32
14	$\sqrt{2}/7$	2.99	896	105504	3.70%	4.71
18	$\sqrt{2}/6$	2.97	882	117243	0.73%	5.52
26	$\sqrt{2}/5$	3.06	936	154596	0.52%	8.49
36	$\sqrt{2}/4$	3.00	900	172170	0.0032%	12.16
56	$\sqrt{2}/3$	2.99	896	213696	0.00003%	17.92
100	$\sqrt{2}/2$	3.00	900	285450	0.00010%	18.78

Table 8.1: The PUFEM results for fixed $totdof$ and τ while increasing m, $ka = 20\pi$.

FEM. According to reference [120], the preconditioned GMRES method is usually the adequate choice to solve a system with a dense matrix because fewer matrix vector products are required compared to other iterative approaches. Therefore the GMRES is chosen for the calculation performed in this Chapter.

8.2 Preconditioned GMRES method

Given the following linear system of equations

$$\mathbf{A}\mathbf{x} = \mathbf{b} \tag{8.1}$$

The basic idea of the GMRES method could be summarized in the following steps. Starting with an initial guess $\mathbf{x}_0$, the residual $\mathbf{r}_0$ is computed as follows

$$\mathbf{r}_0 = \mathbf{b} - \mathbf{A}\mathbf{x}_0 \tag{8.2}$$

and the following vector is defined

$$\mathbf{v} = \frac{\mathbf{r}_0}{\|\mathbf{r}_0\|} \tag{8.3}$$

which is used to construct a Krylov subspace $\mathcal{K}_j \equiv \text{span}\{\mathbf{v}, \mathbf{A}\mathbf{v}, \ldots, \mathbf{A}^{j-1}\mathbf{v}\}$. Finally, $\mathbf{x}_j \in \mathbf{x}_0 + \mathcal{K}$ is set to minimize the residual $\mathbf{r}_j$. As the number of iterations increases, the computational and storage costs increase as well. To overcome this, it is possible to restart the method after a certain number $reiter$ of iterations with resetting $\mathbf{x}_0 = \mathbf{x}_{reiter}$. A detailed description of the method is presented in reference [124].

To enhance the convergence of the GMRES method it is important to improve the conditioning of the coefficient matrix. This is achieved by multiplying a specially designed non-singular matrix $\mathbf{Q}$ with the coefficient matrix either from right or from left. If a right preconditioner is applied to (8.1) then the system of equations is modified into

$$\mathbf{A}\mathbf{Q}^{-1}\mathbf{x}' = \mathbf{b} \qquad \text{with} \quad \mathbf{x}' = \mathbf{Q}\mathbf{x} \tag{8.4}$$

or with a left preconditioner, it is modified into

$$\mathbf{Q}^{-1}\mathbf{A}\mathbf{x} = \mathbf{Q}^{-1}\mathbf{b} \tag{8.5}$$

Different preconditioners are applicable with the GMRES method. Here the Incomplete LU factorization preconditioner (ILU) [124], which is effective for general linear systems, is adopted.

8.3 ILU factorization preconditioners

The ILU factorization approximates a given matrix $\mathbf{A}$ with a multiplication of an upper $\mathbf{U}$ and a lower $\mathbf{L}$ matrices, such that $\mathbf{A}' = \mathbf{L}\mathbf{U}$, with the residual $\mathbf{R}$ given by

$$\mathbf{R} = \mathbf{A}' - \mathbf{A} \tag{8.6}$$

The approximation $\mathbf{A}'$ is defined by two variables namely the level of fill ($lfill$) and the dropping tolerance ($dtoll$). For the first variable, $lfill$, a level for each non-zero entry in $\mathbf{A}'$ is defined. All the entries of a level larger than a certain value, defined by $lfill$, are dropped. For the second variable, $dtol$, all non-zero entries smaller than the product of the row norm and $dtol$, are dropped.

The ILU factorization with a low $lfill$ or a large $dtol$ may reduce the accuracy by dropping too many entries resulting in an increase in the number of iteration. To improve this, one may consider a higher $lfill$ and a lower $dtol$, which could as well sufficiently increase the cost of the factorization. Usually the latter increase in the computation cost is smaller than the cost of higher number of iterations. Further details about the algorithm of ILU factorization are found in reference [124].

8.4 Discrete Wavelet Transform

The Discrete Wavelet Transform (DWT) is a linear transformation which is usually used to approximate a dense matrix written in the standard basis with a sparse matrix written in the wavelet basis, if a suitable basis is chosen. This transform is commonly used in signal processing and image compression.

In this Chapter, only the family of Daubechies wavelet transform is considered of which Haar wavelet is the simplest. The family is defined by two sets of filters, namely z_i defining the low-pass filter and g_i defining the high-pass filter; $i = 0, 1, \ldots, p$ where p is the order of the DWT. The g_i set is derived from z_i as follows

$$g_i = (-1)^i z_{p-1-i} \tag{8.7}$$

The jth level transformation of a vector $\mathbf{v}$ of n components is defined as

$$\tilde{\mathbf{v}} = \mathbf{W}_j \mathbf{W}_{j-1} \ldots \mathbf{W}_1 \mathbf{v} \tag{8.8}$$

where $\mathbf{W}_j$ is a matrix of the dimension $n \times n$ and of the form

$$\mathbf{W}_j = \left[\begin{array}{c|c} \mathbf{W}_t & \Phi \\ \hline \Phi & \mathbf{I} \end{array}\right] \tag{8.9}$$

with $\mathbf{W}_t$ being $n/2^{j-1} \times n/2^{j-1}$ matrix defined as

$$\mathbf{W}_t = \begin{bmatrix}
z_0 & z_1 & z_2 & z_3 & \ldots & z_{m-1} & 0 & 0 & \ldots & & & 0 \\
0 & 0 & z_0 & z_1 & \ldots & & & z_{m-1} & \ldots & & & 0 \\
\vdots & & & & & & \ddots & & & & & \vdots \\
z_4 & z_5 & \ldots & & & & & & & z_0 & z_1 & z_2 & z_3 \\
z_2 & z_3 & \ldots & & & & & & & & & z_0 & z_1 \\
g_0 & g_1 & g_2 & g_3 & \ldots & g_{m-1} & 0 & 0 & \ldots & & & & 0 \\
0 & 0 & g_0 & g_1 & \ldots & & & g_{m-1} & \ldots & & & & 0 \\
\vdots & & & & & & \ddots & & & & & & \vdots \\
g_4 & g_5 & \ldots & & & & & & & g_0 & g_1 & g_2 & g_3 \\
g_2 & g_3 & \ldots & & & & & & & & & g_0 & g_1
\end{bmatrix} \tag{8.10}$$

$\mathbf{I}$ and Φ are the identity and the zero matrices of suitable sizes, respectively.

The application of DWT on a matrix is a direct expansion in two-dimensions of the application on a vector

$$\tilde{\mathbf{A}} = \mathbf{W}_j \mathbf{W}_{j-1} \ldots \mathbf{W}_1 \mathbf{A} \mathbf{W}_1^\top \ldots \mathbf{W}_{j-1}^\top \mathbf{W}_j^\top \tag{8.11}$$

which simply means that the transform is applied on every row and column of the matrix **A**. In the calculation carried out next, only two orders of Daubechies wavelets are considered, the case of $p = 2$ which leads to Haar wavelet with the following filter coefficients

$$\begin{aligned} \{z_i\} &= \{\frac{1}{\sqrt{2}}, \frac{1}{\sqrt{2}}\} \\ \{g_i\} &= \{\frac{1}{\sqrt{2}}, -\frac{1}{\sqrt{2}}\} \end{aligned} \tag{8.12}$$

and the case of $p = 4$ (Daub4) with the coefficients

$$\begin{aligned} \{z_i\} &= \{\frac{1+\sqrt{3}}{4\sqrt{2}}, \frac{3+\sqrt{3}}{4\sqrt{2}}, \frac{3-\sqrt{3}}{4\sqrt{2}}, \frac{1-\sqrt{3}}{4\sqrt{2}}\} \\ \{g_i\} &= \{\frac{1-\sqrt{3}}{4\sqrt{2}}, \frac{3-\sqrt{3}}{4\sqrt{2}}, \frac{3+\sqrt{3}}{4\sqrt{2}}, \frac{-1-\sqrt{3}}{4\sqrt{2}}\} \end{aligned} \tag{8.13}$$

A detailed description of the DWT is found in references [120, 125].

8.5 Wavelet based ILU preconditioner

The idea here is to transform the system (8.1) using a wavelet basis. The matrix **A** and the vectors **x** and **b** could be stored as

$$\mathbf{A} = \begin{bmatrix} \mathbf{A}_{1,1} & \dots & \mathbf{A}_{1,n} \\ \vdots & \ddots & \\ & & \\ \mathbf{A}_{n,1} & & \mathbf{A}_{n,n} \end{bmatrix} \quad , \quad \mathbf{x} = \begin{bmatrix} \mathbf{x}_1 \\ \vdots \\ \\ \mathbf{x}_n \end{bmatrix} \quad , \quad \mathbf{b} = \begin{bmatrix} \mathbf{b}_1 \\ \vdots \\ \\ \mathbf{b}_n \end{bmatrix} \tag{8.14}$$

where n is the total number of nodal points in a PUFEM model and $\mathbf{A}_{i,j}$ is a block matrix of dimension $m \times m$, while $\mathbf{x}_i$ and $\mathbf{b}_i$ are block vectors each corresponding to m plane waves allocated to node i.

The DWT is applied on each block matrix or vector. Thus the transformation matrix is written as

$$\mathbf{W} = \begin{bmatrix} \mathbf{Z} & \dots & \Phi \\ \vdots & \ddots & \\ & & \\ \Phi & & \mathbf{Z} \end{bmatrix} \tag{8.15}$$

with $\mathbf{Z} = \mathbf{W}_j \mathbf{W}_{j-1} \dots \mathbf{W}_1$ and the resulting transformed system corresponding to (8.1) becomes

$$\tilde{\mathbf{A}}\tilde{\mathbf{x}} = \tilde{\mathbf{b}} \tag{8.16}$$

where

$$\tilde{\mathbf{A}} = \mathbf{W}\mathbf{A}\mathbf{W}^\top , \quad \tilde{\mathbf{x}} = \mathbf{W}\mathbf{x} \text{ and } \quad \tilde{\mathbf{b}} = \mathbf{W}\mathbf{b} \tag{8.17}$$

The block diagonal matrix $\mathbf{W}$ is orthogonal because the block matrices forming its diagonal are orthogonal as well. Therefore both matrices $\tilde{\mathbf{A}}$ and $\mathbf{A}$ have the same eigenspectrum.

The two considered Daubechies DWTs, namely Haar and Daub4 transforms, form with the ILU($lfill$) and ILU($dtol$) preconditioners the following combinations:

- ILU($lfill$)-Haar where ILU($lfill$) is applied on $\tilde{\mathbf{A}}$ obtained via Haar DWT.
- ILU($lfill$)-Daub4 where ILU($lfill$) is applied on $\tilde{\mathbf{A}}$ obtained via Daub4 DWT.
- ILU($dtol$)-Haar where ILU($dtol$) is applied on $\tilde{\mathbf{A}}$ obtained via Haar DWT.
- ILU($dtol$)-Daub4 where ILU($dtol$) is applied on $\tilde{\mathbf{A}}$ obtained via Daub4 DWT.

Next the ILU factorization is applied to precondition the linear system before solving it in the standard domain. Then the system is transformed into a wavelet domain before applying the ILU preconditioner and solving it. The performance of the latter approach is tested on a mono scattering problem. It should be mentioned that the Haar wavelet transform was used in reference [73] to reduce the condition number for the micro-local discretization method where plane wave basis combined to the BEM are used to solve Helmholtz problems.

8.6 Numerical results

The PUFEM resulting linear system is preconditioned with either ILU($lfill$) or ILU($dtol$) factorizations. The preconditioned system is solved using the GMRES method in the standard domain. Then the preconditioned system is transformed into a wavelet domain and solved again using the GMRES method. To increase the

ka	m	τ	$totdof$	NNZ	$\log(\kappa)$
50	64	5.41	1856	675840	18.44
100	64	2.71	1856	675840	17.26
150	64	1.80	1856	675840	12.13
200	64	1.35	1856	675840	7.17
150	128	2.55	3712	2703360	18.30
200	128	1.91	3712	2703360	18.46
250	128	1.53	3712	2703360	17.41
300	128	1.28	3712	2703360	16.99
250	256	2.17	7424	10813440	18.95
300	256	1.80	7424	10813440	19.60

Table 8.2: Considered parameters for the problems solved iteratively, mesh grid h_1.

ka	m	τ	$totdof$	NNZ	$\log(\kappa)$
150	64	3.00	5120	2039808	17.62
200	64	2.25	5120	2039808	15.67
250	64	1.80	5120	2039808	12.84
300	64	1.50	5120	2039808	9.18
150	128	4.24	10240	8159232	19.21
200	128	3.18	10240	8159232	19.59
250	128	2.54	10240	8159232	19.71
300	128	2.12	10240	8159232	18.88

Table 8.3: Considered parameters for the problems solved iteratively, mesh grid $h_{\frac{1}{2}}$.

condition number, relatively high numbers of enriching plane waves are considered. This will increase the number of iterations required to obtain a solution.

The model problem, defined in Chapter 2, is reconsidered with the computational domain being defined as the square $(1,1) \leq (x/a, y/a) \leq (2,2)$. The numerical solution is obtained using the PUFEM with the mesh grid h_1 in Figure 8.1 and an increasing number of plane waves. The considered wave numbers are listed alongside with the number m of plane waves, the number τ of degrees of freedom per wavelength, the

	Standard					Haar wavelet					Daub4 wavelet				
ka	$lfill$	ε_2[%]	$NNZc$	$iter$	CPU[s]	$lfill$	ε_2[%]	$NNZc$	$iter$	CPU[s]	$lfill$	ε_2[%]	$NNZc$	$iter$	CPU[s]
50	7	0.000022	1601792	40	11.5	7	0.000041	1604608	40	14.9	7	0.000057	1601472	40	14.4
100	6	0.000018	1592000	20	10.4	6	0.000018	1710528	20	15.6	6	0.000017	1589376	20	14.0
150	7	0.76	1565376	4	10.1	7	0.76	1581120	4	13.8	7	0.76	1588224	4	13.6
200	5	31.3	1558720	16	11.0	5	31.3	1563840	4	13.3	5	31.3	1578176	3	13.9
ka	$dtol$	ε_2[%]	$NNZc$	$iter$	CPU[s]	$dtol$	ε_2[%]	$NNZc$	$iter$	CPU[s]	$dtol$	ε_2[%]	$NNZc$	$iter$	CPU[s]
50	10^{-9}	0.000022	1601792	40	12.5	10^{-9}	0.000041	1604608	40	16.0	10^{-9}	0.000057	1601472	40	14.4
100	10^{-9}	0.000016	1592000	20	11.8	10^{-9}	0.000018	1710528	20	15.5	10^{-9}	0.000018	1589376	20	14.0
150	10^{-8}	0.76	1565376	7	9.6	10^{-8}	0.76	1581120	14	13.8	10^{-8}	0.76	1588224	6	13.6
200	10^{-8}	31.3	1558848	5	9.1	10^{-8}	31.3	1563840	5	13.3	10^{-8}	31.3	1578176	5	13.4

Table 8.4: GMRES results in the standard domain compared to Haar and Daub4 wavelet domains with ILU($lfill$) or ILU($dtol$) preconditioners; mesh grid h_1, $m = 64$.

	Standard					Haar wavelet					Daub4 wavelet				
ka	$lfill$	ε_2[%]	$NNZc$	$iter$	CPU[s]	$lfill$	ε_2[%]	$NNZc$	$iter$	CPU[s]	$lfill$	ε_2[%]	$NNZc$	$iter$	CPU[s]
150	6	0.00016	6500736	160	101.0	6	0.00019	6516224	120	103.1	6	0.00014	6516480	120	102.0
200	7	0.000071	6383872	60	87.2	7	0.000058	6360448	60	97.5	7	0.000068	6383104	80	97.9
250	8	0.00056	6378752	20	87.3	8	0.00055	6361088	20	104.7	8	0.00055	6361344	20	106.9
300	8	0.11	6350464	15	74.9	8	0.11	6264960	12	91.4	8	0.11	6349184	12	96.7
ka	$dtol$	ε_2[%]	$NNZc$	$iter$	CPU[s]	$dtol$	ε_2[%]	$NNZc$	$iter$	CPU[s]	$dtol$	ε_2[%]	$NNZc$	$iter$	CPU[s]
150	10^{-10}	0.00016	6500736	160	85.3	10^{-10}	0.00019	6516224	120	101.7	10^{-10}	0.00014	6516480	120	113.0
200	10^{-10}	0.000077	6383488	80	81.3	10^{-10}	0.00085	6360448	60	99.3	10^{-10}	0.00007	6383104	80	111.2
250	10^{-12}	0.00056	6378752	20	87.3	10^{-12}	0.00053	6361088	20	93.3	10^{-12}	0.00055	6361344	20	95.3
300	10^{-10}	0.11	6350464	12	80.0	10^{-10}	0.11	6264960	14	101.0	10^{-10}	0.11	6349184	13	95.3

Table 8.5: GMRES results in the standard domain compared to Haar and Daub4 wavelet domains with ILU($lfill$) or ILU($dtol$) preconditioners; mesh grid h_1, $m = 128$.

	Standard					Haar wavelet					Daub4 wavelet				
ka	$lfill$	ε_2[%]	$NNZc$	$iter$	CPU[s]	$lfill$	ε_2[%]	$NNZc$	$iter$	CPU[s]	$lfill$	ε_2[%]	$NNZc$	$iter$	CPU[s]
250	-	-	-	> 15000	-	8	0.0017	26607616	14560	3498.5	8	0.0022	25964544	14480	3913.1
300	-	-	-	> 15000	-	7	0.0014	25949440	5660	1745.2	7	0.0018	26022144	6220	2281.5
ka	$dtol$	ε_2[%]	$NNZc$	$iter$	CPU[s]	$dtol$	ε_2[%]	$NNZc$	$iter$	CPU[s]	$dtol$	ε_2[%]	$NNZc$	$iter$	CPU[s]
250	-	-	-	> 15000	-	10^{-12}	0.0017	26607616	14560	4654.8	10^{-12}	0.0022	25964544	14480	4557.6
300	-	-	-	> 15000	-	10^{-14}	0.0014	25949440	5660	2232.6	10^{-14}	0.0018	26022144	6220	2153.4

Table 8.6: GMRES results in the standard domain compared to Haar and Daub4 wavelet domains with ILU($lfill$) or ILU($dtol$) preconditioners; mesh grid h_1, $m = 256$.

	Standard					Haar wavelet					Daub4 wavelet				
ka	$lfill$	ε_2[%]	$NNZc$	$iter$	CPU[s]	$lfill$	ε_2[%]	$NNZc$	$iter$	CPU[s]	$lfill$	ε_2[%]	$NNZc$	$iter$	CPU[s]
150	14	0.000033	8417728	20	102.4	14	0.000032	8189056	20	186.2	14	0.000032	8369753	20	189.2
200	14	0.014	8065285	9	102.3	14	0.014	8002880	9	180.5	14	0.014	7979776	9	186.5
250	14	0.48	7802816	5	94.3	14	0.48	7622784	5	180.0	14	0.48	7980800	5	193.1
300	16	12.1	7798016	3	85.7	16	12.1	7673216	3	172.7	16	12.1	8031872	3	177.4
ka	$dtol$	ε_2[%]	$NNZc$	$iter$	CPU[s]	$dtol$	ε_2[%]	$NNZc$	$iter$	CPU[s]	$dtol$	ε_2[%]	$NNZc$	$iter$	CPU[s]
150	10^{-10}	0.000033	8417728	20	113.5	10^{-10}	0.000032	8189056	20	186.3	10^{-10}	0.000032	8369753	20	199.3
200	10^{-10}	0.014	8065285	10	89.5	10^{-10}	0.014	8002880	9	178.6	10^{-10}	0.014	7979776	9	182.4
250	10^{-9}	0.48	7802816	5	82.9	10^{-9}	0.48	7622784	7	170.3	10^{-9}	0.48	7980800	5	188.7
300	10^{-9}	12.1	7798016	6	86.6	10^{-9}	12.1	7673216	4	169.4	10^{-9}	12.1	8031872	5	179.6

Table 8.7: GMRES results in the standard domain compared to Haar and Daub4 wavelet domains with ILU($lfill$) or ILU($dtol$) preconditioners; mesh grid $h_{\frac{1}{2}}$, $m = 64$.

	Standard					Haar wavelet					Daub4 wavelet				
ka	$lfill$	ε_2[%]	$NNZc$	$iter$	CPU[s]	$lfill$	ε_2[%]	$NNZc$	$iter$	CPU[s]	$lfill$	ε_2[%]	$NNZc$	$iter$	CPU[s]
150	-	-	-	> 15000	-	12	0.00065	34546560	8560	3130.5	12	0.00073	33366912	7900	3079.5
200	14	0.00056	34764416	14480	5243.6	14	0.00092	34277632	9260	3419.4	14	0.00086	34297216	6500	2527.3
250	14	0.00031	32709888	12680	4642.8	14	0.0011	35924224	5800	2697.7	14	0.00058	32461696	4140	1934.7
300	16	0.00029	35854592	6260	2912.0	16	0.00055	34287744	1060	1410.4	16	0.00068	33683584	320	1169.7
ka	$dtol$	ε_2[%]	$NNZc$	$iter$	CPU[s]	$dtol$	ε_2[%]	$NNZc$	$iter$	CPU[s]	$dtol$	ε_2[%]	$NNZc$	$iter$	CPU[s]
150	-	-	-	> 15000	-	10^{-10}	0.00065	34546560	8560	3596.2	10^{-10}	0.00073	33366912	7900	3431.4
200	10^{-13}	0.00056	34764416	14480	5245.7	10^{-13}	0.00092	34277632	9260	4076.9	10^{-13}	0.00086	34297216	6500	3282.5
250	10^{-12}	0.00031	32709888	12680	4493.1	10^{-12}	0.0011	35924224	5800	2902.7	10^{-12}	0.00058	32461696	4140	2164.4
300	10^{-12}	0.00029	35854592	6260	2802.8	10^{-12}	0.00055	34287744	1060	1578.8	10^{-12}	0.00068	33683584	320	1319.1

Table 8.8: GMRES results in the standard domain compared to Haar and Daub4 wavelet domains with ILU($lfill$) or ILU($dtol$) preconditioners; mesh grid $h_{\frac{1}{2}}$, $m = 128$.

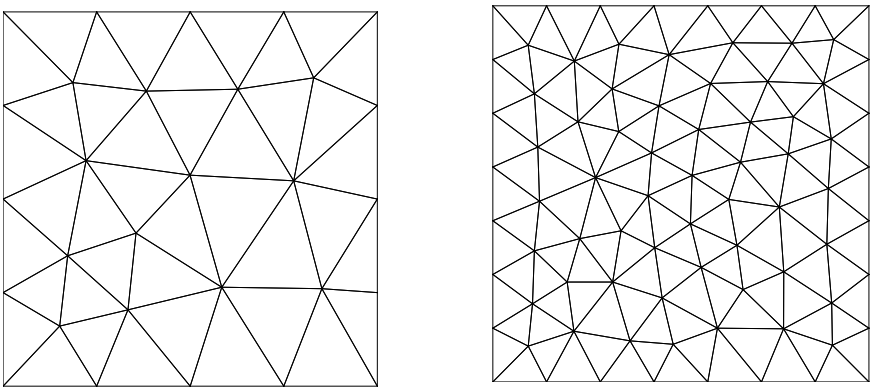

h_1: 40 elements, 29 nodes

$h_{\frac{1}{2}}$: 130 elements, 80 nodes

Figure 8.1: Considered mesh grids.

total number of degrees of freedom, $totdof$, the number NNZ of non-zero entries in the system matrix and the condition number of the system matrix, in Table 8.2. The considered $lfill$ (or $dtol$) of the relevant preconditioner is large (low) enough to obtain the best possible approximation of the system matrix without dropping any element. The computations are performed on Intel(R) Core(TM) 2 Duo CPU (3.00 GHz and 2.99 GHz) with 3.46 GB of RAM under Windows XP Professional (Service Pack 2). The initial guess is zero and the method is restarted every 20 iterations. It is assumed that the solution is found when the criterion $\|\mathbf{r}_j\| \leq \varepsilon(\|\mathbf{A}\|\|\mathbf{x}_j\| + \|\mathbf{b}\|)$, with $\varepsilon = 10^{-8}$, is met. The iterations are terminated if no solution is found after 15,000 iterations.

The results obtained in the standard and the wavelet domains are compared in Tables 8.4, 8.5 and 8.6 for $m = 64, 128$ and 256, respectively. The compared parameters include the L_2 error, the number $NNZc$ of non-zero entries in the conditioned system matrix, the number $iter$ of iterations, the solution CPU time in seconds and the level of fill, $lfill$, or the dropping tolerance, $dtol$, of the relevant preconditioner. For the results obtained with $m = 64$ or 128, the GMRES performs similarly in the standard and the wavelet domains with practically the same error achieved in these domains within similar numbers of iterations. However, the solution time is slightly smaller in the standard domain due to the time needed for the DWT in the wavelet domain. In this set of results the number of non-zeros entries is practically the same if the wavelet domain is compared to the standard domain. When the results obtained with $m = 256$ are considered, the solver performance seems to be improved in the wavelet domain. The results show that the solution does not converge after $15,000$

iterations in the standard domain while it converges in the wavelet domain within this number, which may suggest an improved performance in the wavelet domain.

The solver performance is investigated further by considering the mesh grid $h_{\frac{1}{2}}$ in Figure 8.1 with the considered parameters listed in Table 8.3. The results obtained with the solution space enriched with 64 and 128 plane waves are listed in Tables 8.7 and 8.8, respectively.

The new set of results is consistent with the previous one. Again for the smaller system of equations, with $m = 64$, the solver performs similarly in both domains. When a larger system of equations is considered, with $m = 128$, the solution CPU time is reduced by up to 50% with Haar and by up to 60% with Daub4 in the wavelet domains. This large saving in the solution time is due to the efficient reduction in the number of iterations. Transforming the system into the wavelet domain did not change much the number of non-zero entries in the conditioned system matrix where practically the same numbers are found in the standard or the wavelet domains. The importance of this reduction of the CPU time for the large systems comes from the fact that implementing GMRES is only of practical interest in the case of very large systems.

8.7 Conclusion

In this Chapter, GMRES was used as an iterative solver combined with the ILU factorization preconditioners for the solution of the PUFEM linear system of equations. The solver is used for the solution of small and large systems of equations with a range of wave numbers and different numbers of enriching plane waves, in both the standard and the wavelet domains. The results suggest a significant improvement of the solution time when transforming a large system into Haar or Daub4 wavelet domains. For a small system the DWT does not lead to any improvement but it does not have any significant negative effect on the results as well.

Implementing iterative solvers with the PUFEM has always been an issue due to the conditioning problem. The results here show some promising outcome of such an implementation with an improved convergence when transforming the linear system

with the DWT.

In the next Chapter, general scattering problems are solved with the PUFEM. The scattering bodies are of general shapes and present the effect of singularities in the geometry of the scatterer. Hence no analytical solutions are available and comparisons are carried out by considering high resolution numerical solutions using conventional finite elements.

Chapter 9

Application to general scattering problems

Various aspects of the solution of Helmholtz problems were investigated in the previous chapters using model problems of smooth geometries. Although such problems cover a wide range of applications but engineering applications include non-smooth geometries as well. In this Chapter, problems involving scatterers with non-smooth geometry are dealt with. This is particularly challenging as singularities, due to geometry in this case, may affect the performance of the PUFEM. As there are no analytical solutions available for these problems, the FEM solution is used for comparison.

First, the efficiency and the accuracy of the PUFEM are tested against the FEM on a model problem where the analytical solution is considered to be the reference. Then simple problems with scatterers of sharp corners are solved with both methods and finally a scattering problem by a submarine-like object is considered. For the PUFEM, the assembling process is speeded up by using the exact integration scheme, presented in Chapter 5. The adaptive plane wave enrichment approach, presented in Chapter 7, is used as well.

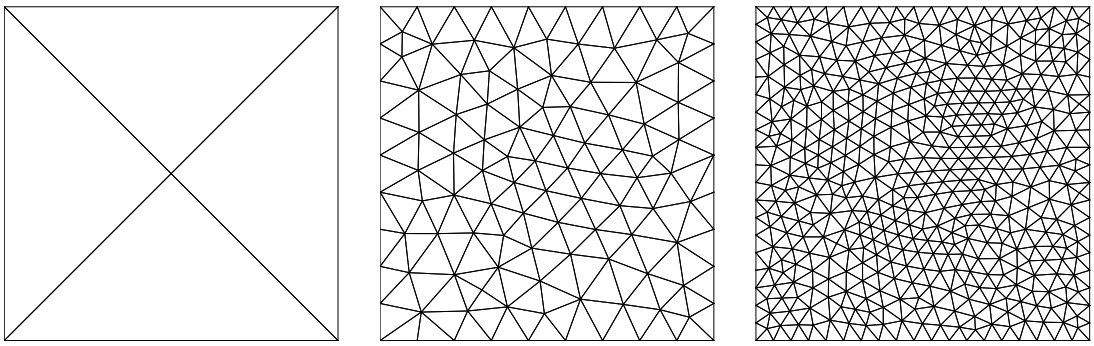

(a) 4 elements, 5 nodes (b) 190 elements, 114 nodes (c) 898 elements, 488 nodes

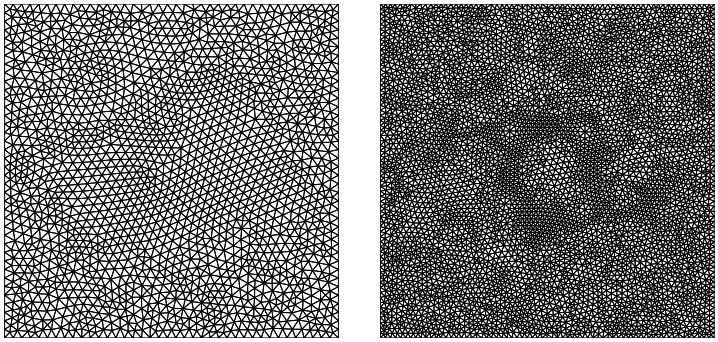

(d) 3526 elements, 1842 nodes (e) 10138 elements, 5202 nodes

Figure 9.1: Mesh grids on the square domain: (a) PUFEM and (b, c, d and e) FEM.

9.1 PUFEM versus FEM

The scattering problem defined in Chapter 8, Section 8.1, is reconsidered for this study with the wave number $ka = 2\pi$ ($\lambda/a = 1$). The diffracted potential is first obtained with the PUFEM where the computational domain is meshed into four elements (Figure 9.1, mesh (a)) with six enriching plane waves at each node. To improve the results, the number of enriching plane waves is increased to $8, 10$ and finally 12 with the mesh being kept unchanged. Then the problem is solved again with the FEM where the computational domain is meshed into elements of a side length of about $h/a = 0.1$ resulting in the resolution of about 10 nodal points per wavelength (Figure 9.1, mesh (b)). To improve this, the domain is re-meshed into smaller elements of size $h/a = 0.05$ then 0.025 and finally 0.015 (Figure 9.1, meshes(c, d and e), respectively). The corresponding number of elements is increased from 190 in mesh (b) to 898 then $3,526$ and finally $10,138$ elements in mesh (e).

Table 9.1 shows the number τ of degrees of freedom per wavelength alongside the total number of degrees of freedom, $totdof$, the total number of the system matrix

entries needed to be stored, *totsys*, and the L_2 error with both methods. The results show clearly that the PUFEM leads to a better accuracy with a much smaller *totdof* and *totsys*. It is also clear that with the PUFEM adding only a few plane waves improves the results significantly while in the FEM re-meshing is necessary to achieve same improvement in the results. It is even possible to further improve the results with the PUFEM by increasing the number of plane waves because the total number of degrees of freedom with 12 enriching plane waves is still low, $totdof = 60$.

PUFEM				FEM			
τ	totdof	totsys	ε_2[%]	τ	totdof	totsys	ε_2[%]
5.48	30	429	2.25%	10.68	114	3626	5.39%
6.32	40	756	0.20%	22.09	488	74852	1.28%
7.07	50	1175	0.11%	42.92	1842	1093561	0.31%
7.75	60	1686	0.03%	72.12	5202	8644656	0.11%

Table 9.1: PUFEM results versus FEM results for an increasing number of degrees of freedom, $ka = 2\pi$.

The comparison is carried out further by increasing the wave number to $ka = 4\pi$. The results with both methods are compared in Table 9.2. The PUFEM results with six plane waves and the FEM results with mesh (b) are excluded as the L_2 error becomes too high in these cases. The new set of results is consistent with the previous one where the PUFEM requires much fewer degrees of freedom to obtain a better accuracy. Despite the relatively low wave numbers and the small computational domain, the FEM solution started already to become cumbersome with more than 5,200 degrees of freedom to obtain an error just below 1%. This shows the difficulty of solving wave problems with the FEM. On the other hand, the PUFEM seems to be much more practical with a total of 60 degrees of freedom being enough to obtain a similar error.

In the second part of this study the results with both methods are compared for a similar τ. The considered computational domain is redefined to include the area around the two scatterers, $(-3.0, -1.5) \leq (x/a, y/a) \leq (3.0, 1.5)$. The problem is solved for the wave number $ka = 2\pi$ using the mesh grids displayed in Figure 9.2 and with the analytical solution being applied on the boundary through a Robin type

PUFEM				FEM			
τ	totdof	totsys	$\varepsilon_2[\%]$	τ	totdof	totsys	$\varepsilon_2[\%]$
3.16	40	756	4.65%	11.05	488	74852	9.46%
3.54	50	1175	1.38%	21.46	1842	1093561	2.41%
3.87	60	1686	0.81%	36.06	5202	8644656	0.85%

Table 9.2: PUFEM results versus FEM results for an increasing number of degrees of freedom, $ka = 4\pi$.

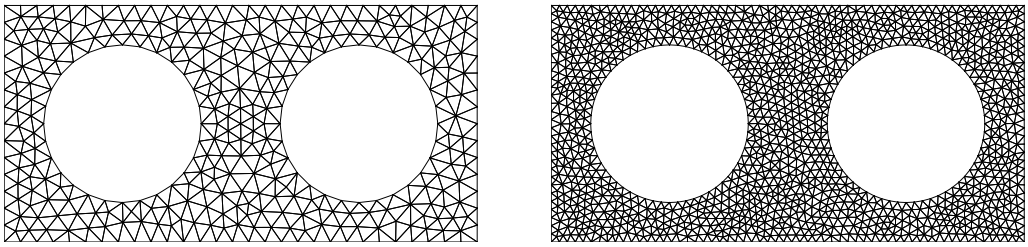

(f) 604 elements, 372 nodes

(g) 2534 elements, 1414 nodes

Figure 9.2: Mesh grids: (f) PUFEM and (g) FEM.

boundary condition. This simulates a case in which many small elements are required due to geometry description. Such a case is not preferred with the PUFEM where larger elements and high numbers of enriching plane waves, improve the method performance. The relatively coarse mesh is used with the PUFEM while the fine mesh is used with the FEM. By enriching the PUFEM mesh grid with four plane waves a similar τ is achieved with both methods.

For $\tau = 10.99$, the FEM leads to results with an error $\varepsilon_2 = 6.28\%$ while for a slightly higher value, $\tau = 11.26$, the PUFEM leads to results with an error $\varepsilon_2 = 0.66\%$. Although the FEM has the advantage of a better geometry representation but the PUFEM leads to better quality results. This shows the potential of the PUFEM compared to the FEM in solving such problems.

It should be added that the relatively low numbers of enriching plane waves was necessary here in order to have a comparable number τ of degrees of freedom per wavelength in both methods. For a higher number of enriching plane waves in the PUFEM a much more refined mesh with the FEM is required in order to keep a similar τ.

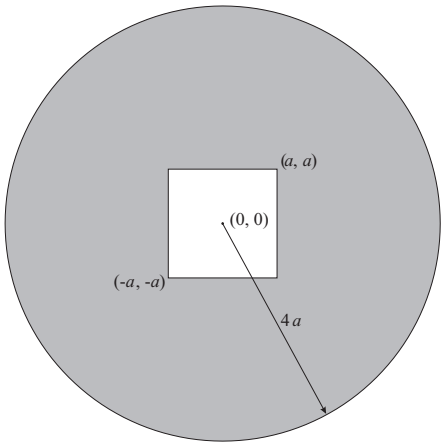

Figure 9.3: Square scatterer problem layout.

9.2 Non-smooth scatterers

If the scatterer presents a non-smooth geometry, such as sharp corners, the solution may display singularities around the corners. In numerical methods, the existence of such singularities makes the solution computationally expensive as mesh refinements may be required around the corners otherwise large errors may occur. Dealing with these singularities in numerical methods was investigated by many authors. A notable contribution in the context of the enriched FEM with problems including a square, a snowflake and a cavity scatterers were solved in reference [70]. A comprehensive list of references in this regard is found in [126].

In this section, the PUFEM is tested with singularities due to the geometry description. Different non-smooth scatterers are considered where the PUFEM results are compared to the FEM solution.

9.2.1 Square scatterer

A mono scattering problem is considered where a square cylinder is hit by a plane wave, with $ka = 2\pi$, propagating in the positive x-direction. Figure 9.3 shows the problem layout. The considered boundary conditions are Neumann on the scatterer and BGT-2 on the outer boundary. The weak form of this problem is similar to that derived in Chapter 4, expression (4.23). First the problem is solved with the FEM and then with the PUFEM.

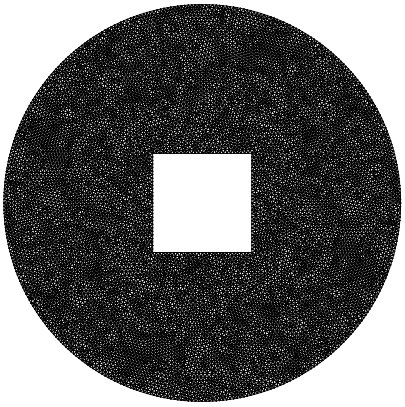

FEM mesh (1) (coarse)

21416 elements, 10942 nodes

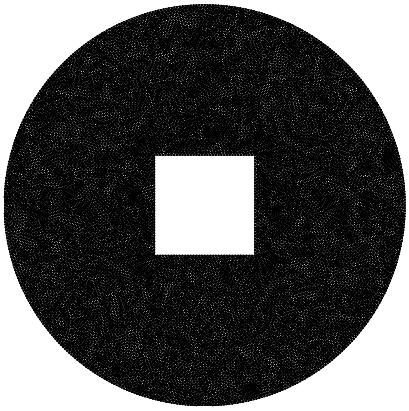

FEM mesh (2) (fine)

34846 elements, 17723 nodes

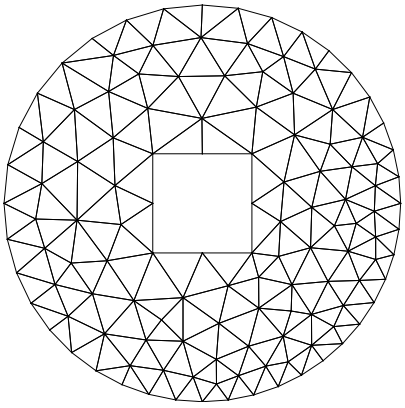

PUFEM mesh

204 elements, 126 nodes

Figure 9.4: Square scatterer: considered mesh grids.

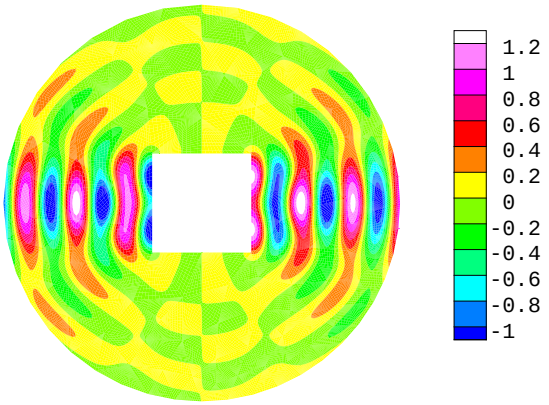

Figure 9.5: Square scatterer: real part of the diffracted potential, FEM solution, $ka = 2\pi, \tau_{\text{PUFEM}} = 8.1, \tau_{\text{FEM1}} = 15.4, \tau_{\text{FEM2}} = 19.5$.

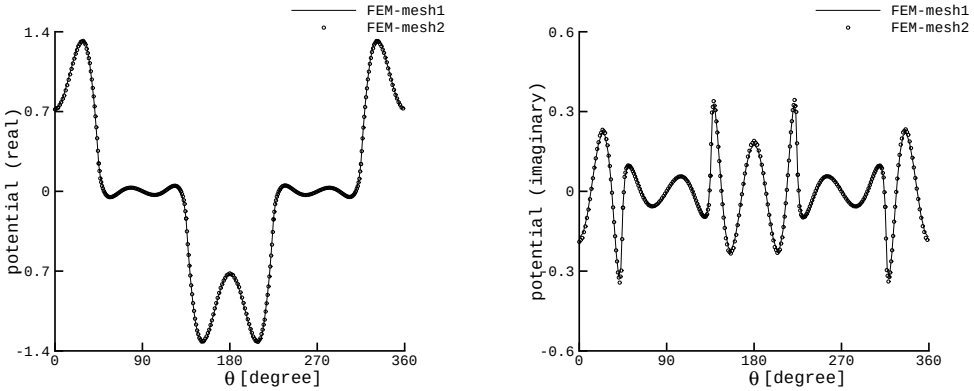

Figure 9.6: Square scatterer: real and imaginary parts of the diffracted potential around the scatterer, FEM solutions, $ka = 2\pi$.

To ensure the convergence of the numerical solution with the FEM, the considered problem is solved twice. First the domain is meshed such that there is at least ten nodal spaces per wavelength. Then a finer mesh is considered and the problem is solved again. The two mesh grids are shown in Figure 9.4. The convergence of the FEM is confirmed when the solutions with both mesh grids coincide well. In other words further refining the mesh does not change the solution.

A contour plot of the real part of the diffracted potential obtained with the finest mesh grid is displayed in Figure 9.5 while the real and the imaginary parts of the diffracted potential around the scatterer are plotted in Figure 9.6. The latter figure shows that the solutions with both mesh grids have captured the same scattering pattern.

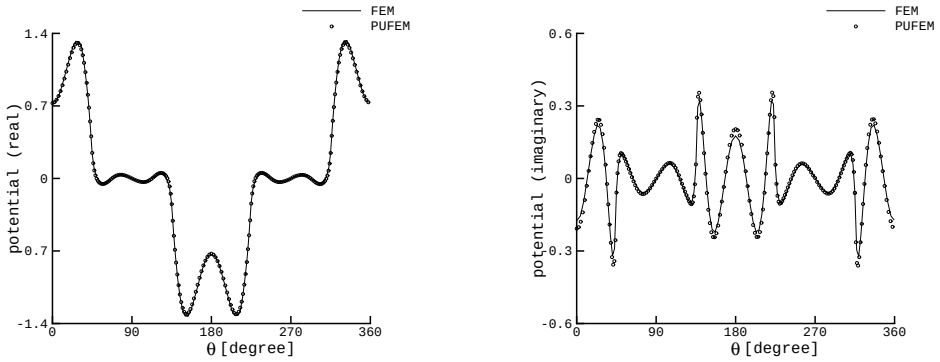

Figure 9.7: Square scatterer: real and imaginary parts of the diffracted potential around the scatterer, FEM and PUFEM solutions, $ka = 2\pi$.

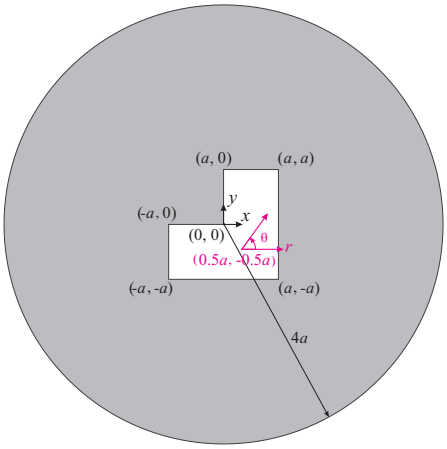

Figure 9.8: Non-convex polygon scatterer: problem layout.

The PUFEM is used to solve the problem using the coarse mesh grid shown in Figure 9.4. The number of enriching plane waves is $m = 18$. The real and imaginary parts of the diffracted potential around the scatterer are compared to the FEM results in Figure 9.7 which shows a good agreement. However, the total number of degrees of freedom with the PUFEM is $totdof = 3,024$ ($\tau = 8.1$) while with the FEM (coarse mesh) is $totdof = 10,942$ ($\tau = 15.4$). This shows the large saving when the PUFEM is used and confirms the previous conclusions.

9.2.2 Non-convex polygon scatterer

A non-convex polygon scatterer is hit by a plane wave, with $ka = 2\pi$, propagating in the positive x-direction. Figure 9.8 shows the problem layout. Again the problem is first solved with the FEM then with the PUFEM.

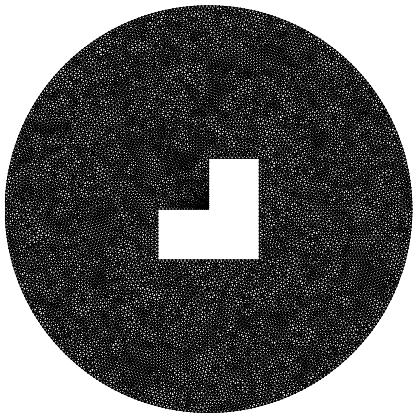

FEM mesh (1) (coarse)

22162 elements, 11320 nodes

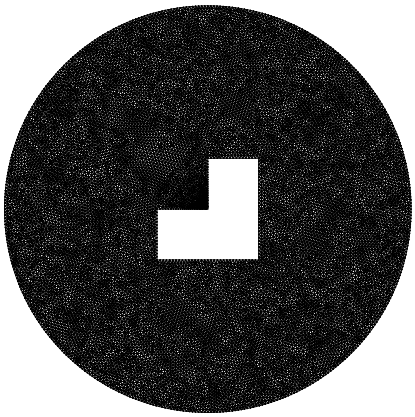

FEM mesh (2) (fine)

29402 elements, 14982 nodes

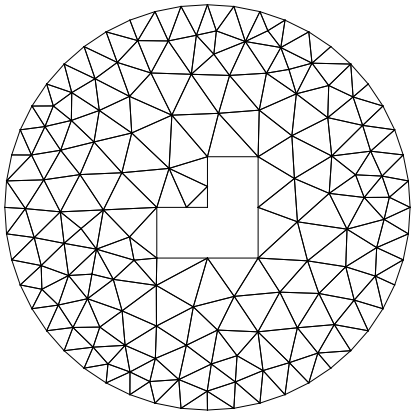

PUFEM mesh

256 elements, 157 nodes

Figure 9.9: Non-convex polygon scatterer: mesh grids.

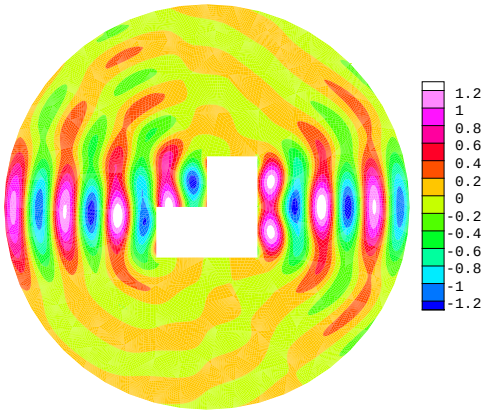

Figure 9.10: Non-convex polygon scatterer: real part of the diffracted potential, FEM solution, $ka = 2\pi, \tau_{\text{PUFEM}} = 7.7, \tau_{\text{FEM1}} = 15.4, \tau_{\text{FEM2}} = 17.7$.

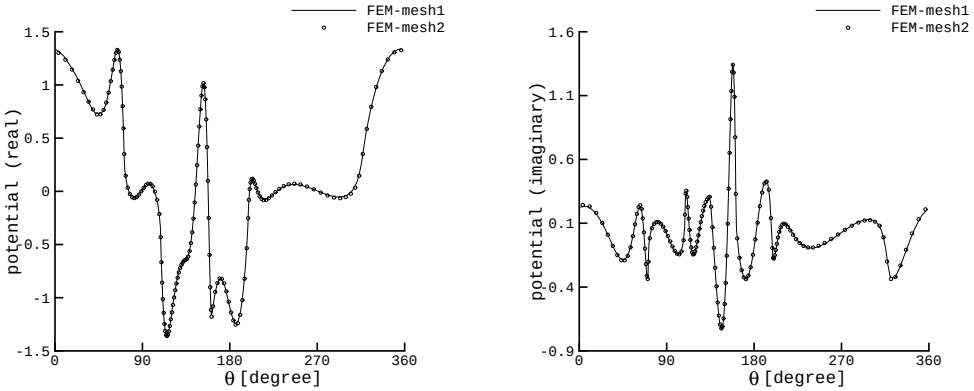

Figure 9.11: Non-convex polygon scatterer: real and imaginary parts of the diffracted potential around the scatterer, FEM solutions, $ka = 2\pi$.

For the FEM solution, the same procedure as before is followed by solving the problem twice to ensure the solution convergence. In the first mesh the traditional requirement of at least ten nodal spaces per wavelength is fulfilled. In both meshes finer elements are used in the area close to the reflex angle of the polygon. Figure 9.9 shows the two mesh grids.

A contour plot of the real part of the diffracted potential is displayed in Figure 9.10 while the real and imaginary parts of the diffracted potential around the scatterer obtained using both mesh grids are plotted in Figure 9.11 where the angle θ in this figure is noted in Figure 9.8. It can be seen that both mesh grids lead to similar results.

For the PUFEM solution, the computational domain is meshed into relatively coarse

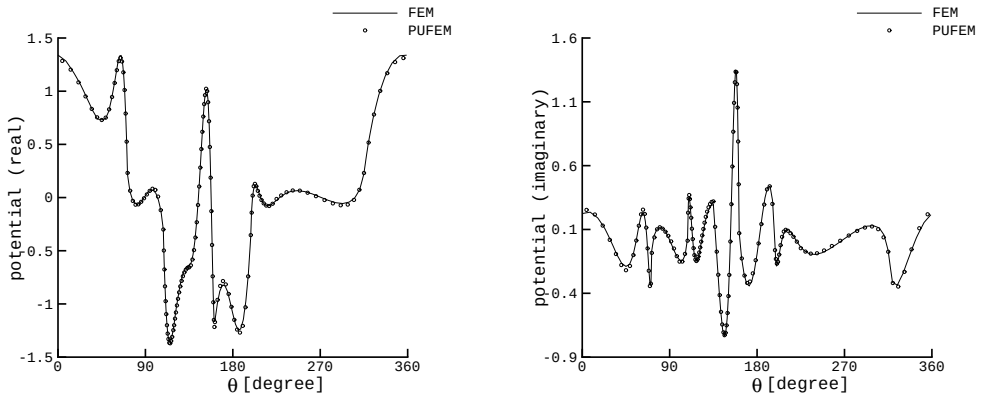

Figure 9.12: Non-convex polygon scatterer: real and imaginary parts of the diffracted potential around the scatterer, FEM and PUFEM solutions, $ka = 2\pi$.

elements with no mesh refinement close to the reflex angle (Figure 9.9). The solution space is enriched with 18 plane waves. The real and imaginary parts are plotted with the FEM results in Figure 9.12 which shows good agreement although the number of degrees of freedom with the PUFEM $totdof = 2,826$ ($\tau = 7.7$) is smaller than the FEM with the coarse mesh being considered, $totdof = 11,320$ ($\tau = 15.4$).

9.2.3 Submarine-like shaped scatterer

In this subsection, an elongated scatterer that is shaped like a submarine is considered. This problem has already been dealt with by different authors [80, 127, 128]. The computational domain is relatively large due to the elongated body of the scatterer and the circular character of the outer boundary. The problem layout is shown in Figure 9.13. The weak formulation and the boundary conditions are the same as in previous problems. The scatterer has relatively complicated geometry in comparison to the problems solved so far in this thesis and includes singularities at the right angled corners of the conning tower.

The scatterer is hit by a plane wave propagating in the positive x-direction with the wave number $ka = 2\pi$. The FEM convergence is confirmed in the same way as before using the two mesh grids displayed in Figure 9.14. The results obtained using these mesh grids are plotted in Figure 9.15 while Figure 9.16 shows contour plots of the real part of the diffracted potential over the computational domain. Figure 9.15 shows good agreement between the results using both FEM mesh grids.

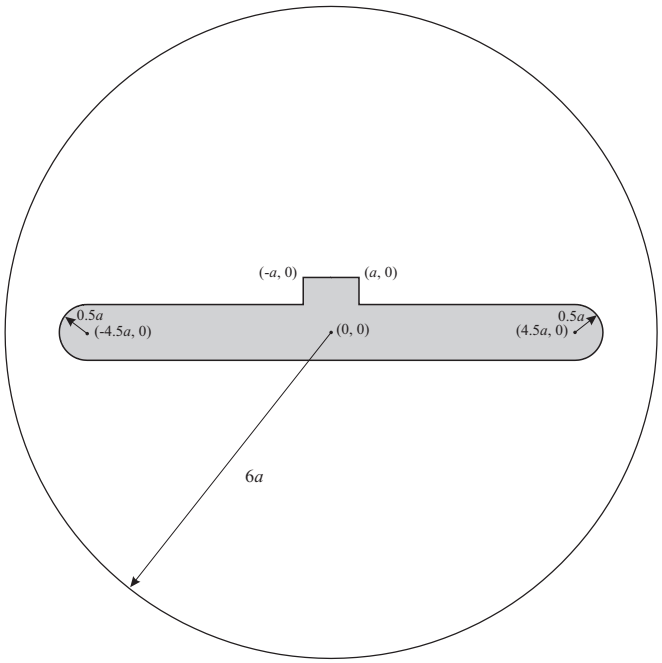

Figure 9.13: Submarine-like scatterer problem layout.

For the PUFEM solution, mesh (1) of Figure 9.17 is used with a variable number of plane waves ($m_{min} = 12$ and $m_{max} = 30$). It is important to refine the mesh close to the front and rear parts of the scatterer in order to take into consideration the circular geometry at these locations while the rest of the domain is filled with relatively large elements. Comparisons of the PUFEM and the FEM results are carried out and shown in Figure 9.18. The results again show that the solution with the PUFEM is similar to that with the FEM. The total number of degrees of freedom is $totdof = 11,398$ and $\tau = 10.5$ while the corresponding numbers with the coarse FEM mesh are $totdof = 11,791$ and $\tau = 10.7$. The relatively high value of τ with the PUFEM is due to the large number of elements close to the curved edges and to the low wave number considered, however, in the next section τ is significantly reduced when higher wave numbers are considered.

The problem is now solved for higher wave numbers $ka = 6\pi, 8\pi$ and 10π. A new mesh grid is considered with finer elements close to the curved sides and the corners of the scatterer (Figure 9.17, mesh (2)). The number of plane waves is varied between 8 and 50. The results are plotted in Figures 9.19, 9.20 and 9.21. The resulting numbers of degrees of freedom per wavelength are $\tau = 4.57, 3.42$ and 2.74 for $ka = 6\pi, 8\pi$ and 10π, respectively. This shows the potential of the PUFEM in solving problems of a complicated geometry with relatively coarse mesh grids and low number of degrees

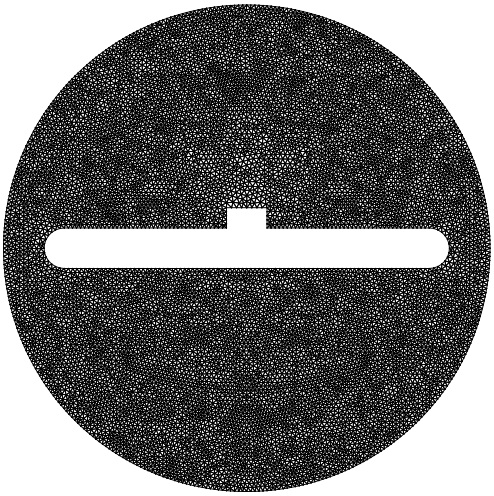

mesh (1): 22992 elements, 11791 nodes

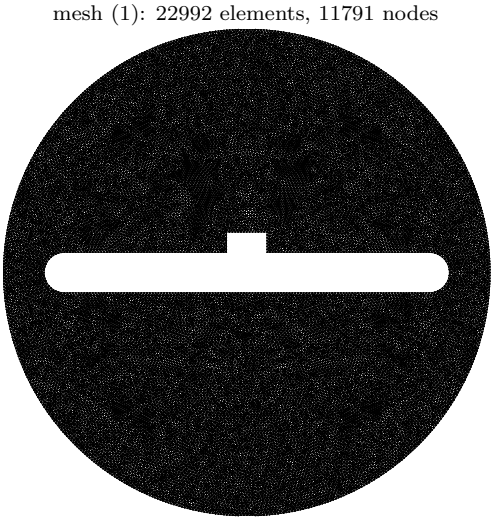

mesh (2): 48228 elements, 24539 nodes

Figure 9.14: Submarine-like scatterer: FEM mesh grids.

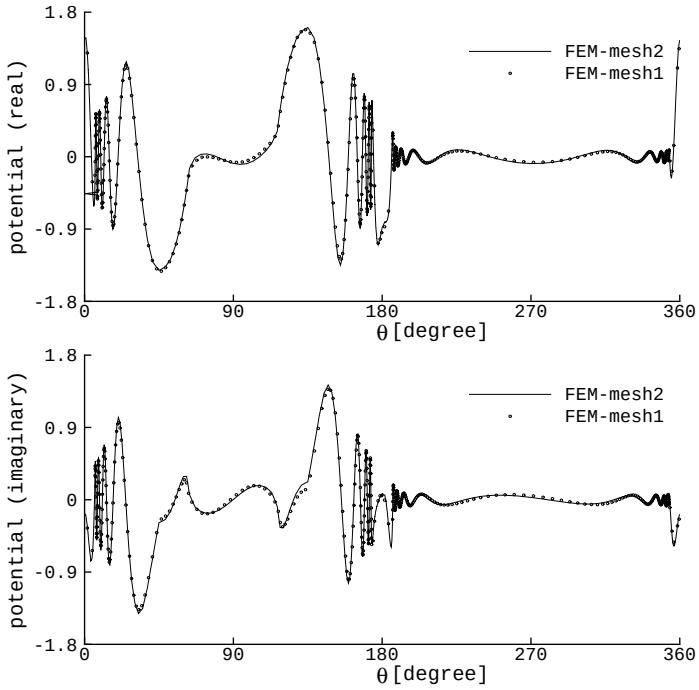

Figure 9.15: Submarine-like scatterer: real and imaginary parts of the diffracted potential around the scatterer, FEM solutions, $ka = 2\pi$.

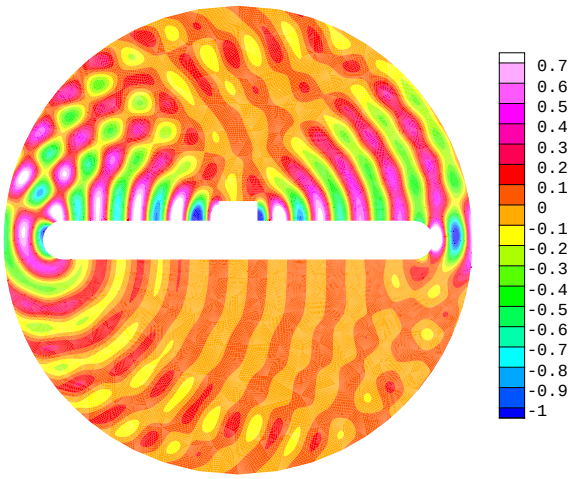

Figure 9.16: Submarine-like scatterer: real part of the diffracted potential, FEM solution, $ka = 2\pi, \tau_{\text{PUFEM}} = 10.5, \tau_{\text{FEM1}} = 10.7, \tau_{\text{FEM2}} = 15.4$.

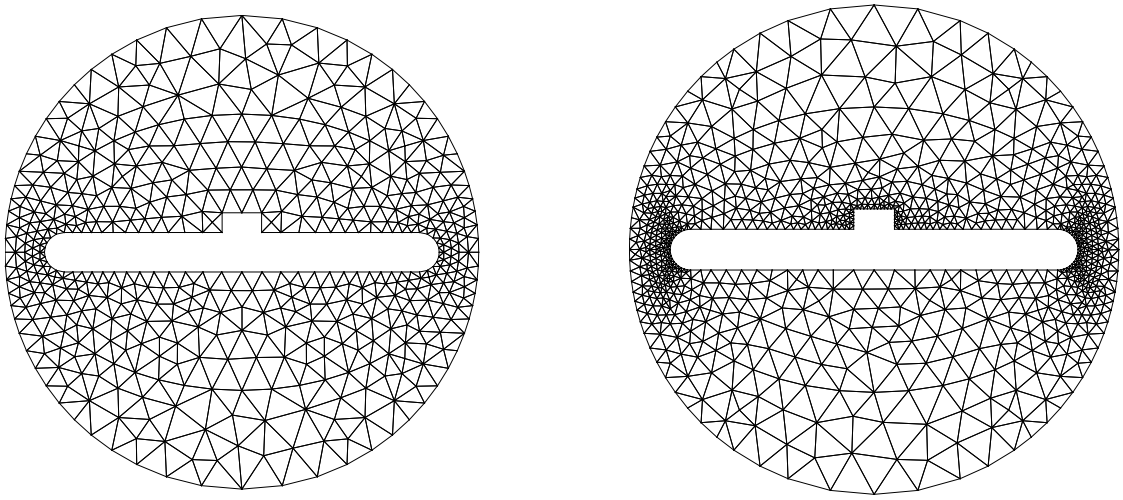

mesh (1): 537 nodes, 932 elements

mesh (2): 982 nodes, 1756 elements

Figure 9.17: Submarine-like scatterer: PUFEM mesh grids.

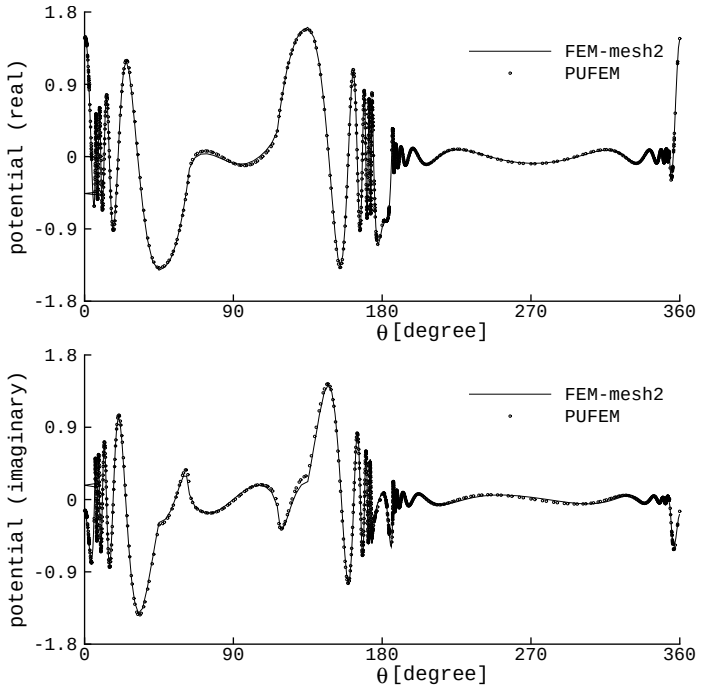

Figure 9.18: Submarine-like scatterer: real and imaginary parts of the diffracted potential around the scatterer, FEM and PUFEM solutions, $ka = 2\pi$.

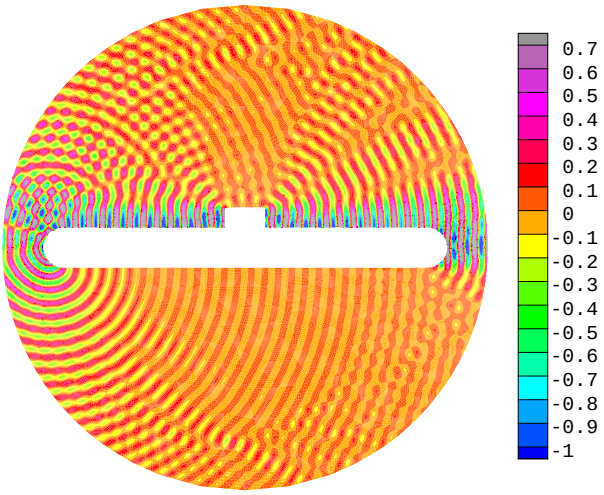

Figure 9.19: Submarine-like scatterer: real part of the diffracted potential, $ka = 6\pi, \tau = 4.57$.

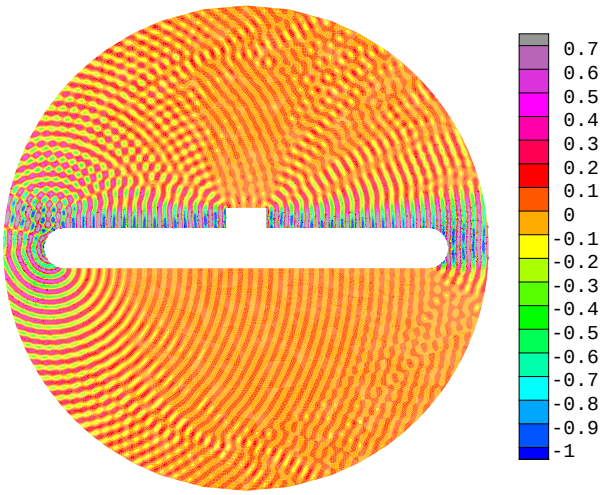

Figure 9.20: Submarine-like scatterer: real part of the diffracted potential, $ka = 8\pi, \tau = 3.42$.

of freedom per wavelength. For these examples, no comparisons were carried out with the FEM solutions because the FEM would require huge numbers of nodal points to satisfy the traditional *rule of thumb*. However, higher discretization levels were considered by increasing the numbers of enriching plane waves and the results remained unchanged.

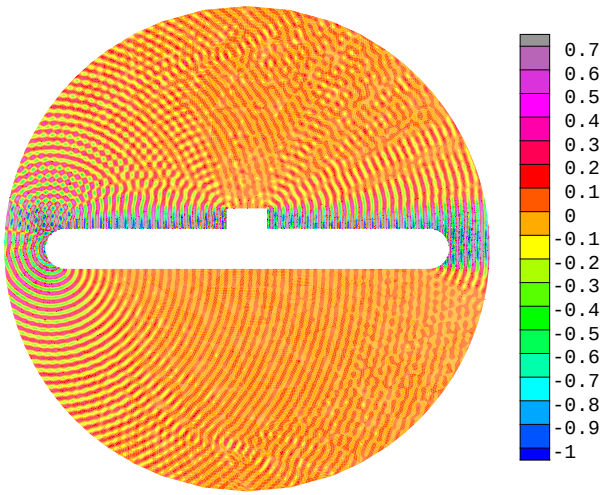

Figure 9.21: Submarine-like scatterer: real part of the diffracted potential, $ka = 10\pi, \tau = 2.74$.

9.3 Conclusion

In this Chapter the PUFEM was used for the solution of general scattering problems. As there are no analytical solutions available for such problems, FEM solutions are used for comparison. First the efficiency of the PUFEM was tested against the FEM. Then problems of simple geometry scatterers with singularities were considered. The results show the reduction in the total number of degrees of freedom with the PUFEM compared to the FEM.

A scattering problem by a submarine-like scatterer is dealt with using both the FEM and the PUFEM. The two methods lead to similar results at a low wave number. At higher wave numbers, it is possible to solve the problem using the PUFEM by keeping the mesh grid unchanged and increase the number of enriching plane waves. Solving the same cases with the FEM is not possible because it would require larger computing facilities than those used for this work.

Chapter 10

Conclusion

In this work, a few numerical aspects affecting the performance of the PUFEM for the solution of two-dimensional Helmholtz wave problems are analysed with the aim to improve its efficiency. Overall, the method proved to be very successful in solving short wave problems with significant reduction of the computational effort and improved quality of the results, in comparison to the FEM.

First, it is known from past work carried out by various researchers that the use of cylindrical waves, named Vekua functions, leads to the same performance obtained with the plane wave enrichment. However, it is shown from the current work that the use of Vekua functions in the far field of exterior scattering problems lead to even more reduction of the computational effort, in comparison to the plane waves. With the plane wave enrichment, it was stated that at high wave numbers a discretization level of around 2.5 degrees of freedom per wavelength was enough to achieve results of engineering accuracy. It is shown here that, in the far field, the Vekua function approximation provides accurate results even when the number of degrees of freedom per wavelength is very low.

Unlike in the FEM, in the PUFEM the computational burden shifts from the solution to the matrix assembly process due to the highly oscillatory integrals of the element matrices. But the ease of analytically evaluating these integrals for straight edges elements makes the plane wave enrichment preferred to the cylindrical waves.

Through the convergence analysis, it is shown that both h-refinement and an increase of the number m of the approximating plane waves (q-convergence) lead to

a significant decrease of the error, provided that the condition number is not too high. In fact, it was observed for a 3-noded finite element scheme that h-refinement leads to an exponential decrease of the error with an estimated rate of convergence $\alpha \geq \frac{m}{2} - 1$. Moreover, for a same total number of degrees of freedom, higher order elements (p-convergence) lead to more accurate results in comparison to low order elements but at the price of a higher condition number.

It is clear from the various analyses carried out in this work that better performance of the PUFEM can be achieved by considering large elements, compared to the wavelength, with high numbers of approximating plane waves rather than use small elements with low numbers of approximating plane waves. In practice, this is not usually possible due to the need of accurately describing the geometry details and/or capturing singularities and hence small elements as well as large elements should be used. In such cases, adaptive plane wave enrichment whereby the number of approximating plane wave is adapted with respect to the mesh size, leads to good quality results while keeps the conditioning within acceptable limits.

The plane wave basis finite elements proved to be very successful in dealing with multiple scattering problems and with problems presenting the effect of singularities in the geometry of the scatterer. The numerical tests clearly showed that the wave enriched elements lead to similar results provided by high resolution numerical solutions using conventional finite elements. This was achieved at a low computational effort, in comparison to polynomial based finite elements, especially when the exact integration and the adaptive plane wave enrichment are used.

Despite speeding up the matrix assembly process, through the exact integration of the element matrices, the use of the PUFEM to large scale problems such as three dimensional wave scattering would require substantial time for the solution process. It is obvious that an iterative approach combined with an efficient preconditioner is the way forward. In this work, the GMRES iterative solver was used with an incomplete lower and upper based preconditioner. It is shown that the iterative solution could be further enhanced by solving the system in the wavelet domain.

Recommendations for further research

From the method point of view, since most scattering problems involve infinite media, it would be suitable to couple the plane wave basis finite elements (PUFEM) with the plane wave basis boundary element method (PUBEM). Like the PUFEM, the PUBEM leads to significant improvements over the performance of conventional boundary elements. In such combined method, the PUFEM will deal with the computational domain containing details of interest while the PUBEM will deal with the outer boundary so that radiation to infinity would be automatically incorporated in the formulation.

An obvious drawback of this coupling is the non-local aspect of the PUBEM leading to a fully populated matrix, which spoils the sparse characteristic of the PUFEM system matrix. One way of overcoming this issue is to consider the fast multipole method to speed up the matrix-vector products of the iterative solution.

Another possibility would be to enrich the finite element space with both plane waves and Vekua functions. If this proves to be successful in solving exterior scattering problems, the plane waves would be useful to model the near field while the Vekua functions would perform better in modelling the far field. An obvious difficulty lies in the integration of the Vekua functions for which an exact method is not straightforward.

From the application point of view, a challenging problem would concern the wave scattering in fluid-solid coupled problems. The fluid may have different densities and the solid medium may be multilayered. This is of great interest for hydrocarbons prospection research, among many examples.

Appendix A

Single scattering model

The scattering of a plane wave by a rigid circular cylinder is considered. The potential of the incident plane wave ϕ_I propagating in the positive x-direction is given by

$$\phi_I = e^{\mathrm{i}kx} = e^{\mathrm{i}kr\cos\theta} \tag{A.1}$$

Figure A.1 shows the scatterer and the direction of the plane wave.

The exponential part of (A.1) could be rewritten as an infinite series of the first kind Bessel function

$$\phi_I = \sum_{q=0}^{+\infty} \mathrm{i}^q \epsilon_q J_q(kr)\cos(q\theta) \tag{A.2}$$

where $\epsilon_q = 2$ for $q = 0$ and 1 for $q \in [1, +\infty]$. $J_q(kr)$ is the Bessel function of the first kind and order q.

The incident wave is diffracted by a vertical cylinder of the radius a (Figure A.1).

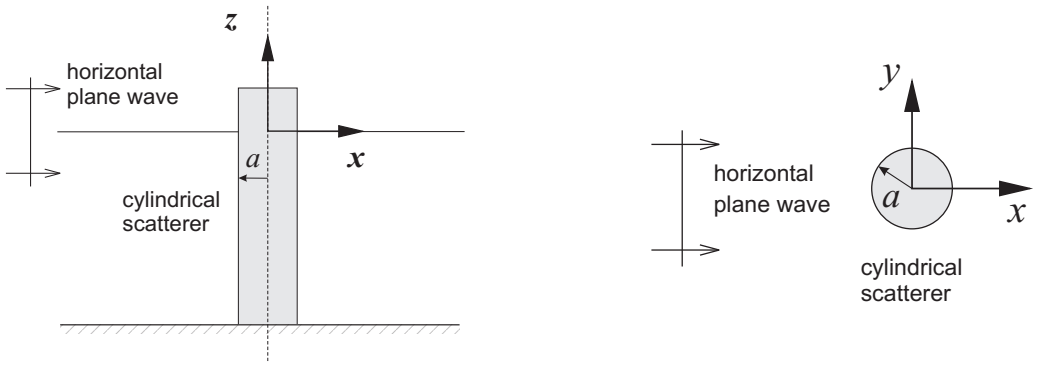

Figure A.1: Single scattering in medium depth water.

The scattered potential ϕ_S in the domain Ω satisfies the Helmholtz equation

$$(\nabla^2 + k^2)\phi_S = 0 \qquad \text{in} \quad \Omega \tag{A.3}$$

The scatterer is rigid and impermeable. Thus the incident and the scattered potentials are equal on the cylinder surface which is expressed by Neumann boundary condition

$$\frac{\partial \phi_S}{\partial r} = -\frac{\partial \phi_I}{\partial r} \qquad \text{on} \quad r = a \tag{A.4}$$

The outgoing scattered wave radiates away from the scatter which is expressed by Sommerfeld radiation boundary condition.

$$\lim_{r\to\infty} r^{1/2}(\frac{\partial \phi_S}{\partial r} - \mathrm{i}kr) = 0 \qquad \text{uniformly in} \quad \theta \tag{A.5}$$

The solution of the boundary value problem defined by the Helmholtz equation and the Neumann and Radiation boundary conditions is expressed by

$$\phi_S = -\sum_{q=0}^{+\infty} \mathrm{i}^n \epsilon_q B_q H_q(kr)\cos(q\theta) \tag{A.6}$$

where B_q is an unknown.

The radiation boundary condition is satisfied by the presence of the first order Hankel function $H_q(kr)$. The unknown B_q is defined to fulfill Neumann boundary condition. From (A.2, A.6 and A.4) one can find

$$B_q = \frac{J'_q(ka)}{H'_q(ka)} \tag{A.7}$$

The prime in $J'_q(ka)$ and $H'_q(ka)$ denotes differentiation with respect to the argument. Thus (A.6) becomes

$$\phi_S = -\sum_{q=0}^{+\infty} \mathrm{i}^n \epsilon_q \frac{J'_q(ka)}{H'_q(ka)} H_q(kr)\cos(q\theta) \tag{A.8}$$

The total potential ϕ_T is the sum of the incident and the diffracted waves $\phi_\mathrm{T} = \phi_I + \phi_S$ thus

$$\phi_\mathrm{T} = \sum_{q=0}^{+\infty} \mathrm{i}^n \epsilon_q [J_q(kr) - \frac{J'_q(ka)}{H'_q(ka)} H_q(kr)]\cos(q\theta) \tag{A.9}$$

For numerical implementation

$$Q_{min} = Rk \tag{A.10}$$

where Q_{min} is the minimum number of components to obtain accurate results with R being the distance between the center of the scatterer and the farthest considered

point from the center. It is possible to consider more components however considering a much larger number may increase the round off error which will affect the accuracy. Now (A.9) may be rewritten as

$$\phi_{\mathrm{T}} = \sum_{q=0}^{Q_{min}} \mathrm{i}^n \epsilon_q [J_q(kr) - \frac{J'_q(ka)}{H'_q(ka)} H_q(kr)] \cos(q\theta) \tag{A.11}$$

which is the analytical model of the single scattering problem.

Appendix B

Multiple scattering model

The scattering of a plane wave by an array of NC cylinders is considered. Figure B.1 shows a distribution of multiple scatterers with respect to the plane wave while Figure B.2 shows the spatial correlation of two scatterers.

The plane wave is of a phase equal to zero at the origin thus the phase at the cylinder number j is given by

$$I_j = e^{\mathrm{i}kx_j} \tag{B.1}$$

where x_j and y_j are the coordinates of the center of the cylinder. If a local polar coordinate system is chosen at the center (r_j, θ_j) the plane wave in the new coordinates could be rewritten as

$$\phi_I = I_j e^{\mathrm{i}kr_j \cos\theta_j} \tag{B.2}$$

Again here, the exponential part of (B.2) might be expressed as an infinite series of

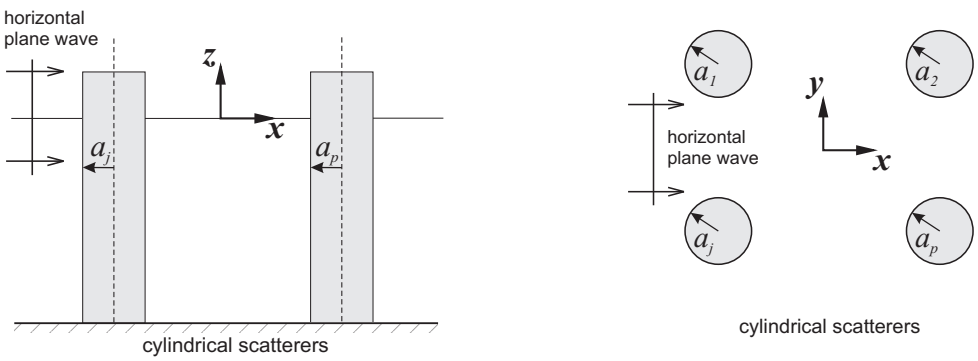

Figure B.1: Multiple scattering problem in medium depth water.

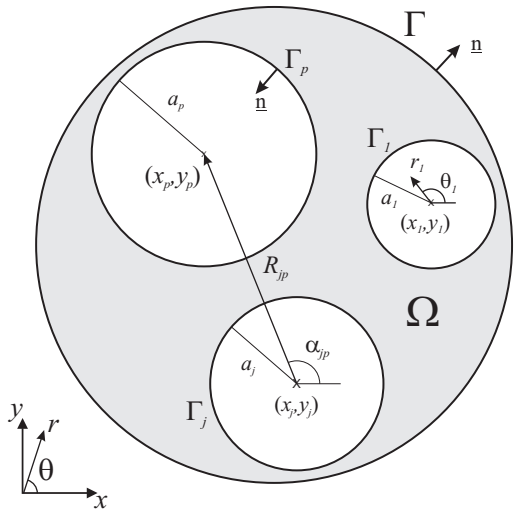

Figure B.2: Spatial correlation of the scatterers.

the first order Bessel function.

$$\phi_I = I_j \sum_{q=-\infty}^{+\infty} J_q(kr_j) e^{\mathrm{i}q(\frac{\pi}{2}-\theta_j)} \tag{B.3}$$

The potential of a plane wave scattered by a single cylinder is expressed in the following form (A.9)

$$\phi_S = -\sum_{q=-\infty}^{+\infty} \mathrm{i}^q \frac{J'_q(ka)}{H'_q(ka)} H_q(kr) e^{\mathrm{i}q\theta} \tag{B.4}$$

The above equation could be then used to express the potential of the plane wave scattered by the jth cylinder. But here the scattered wave will re-scatter again by hitting the neighboring cylinders. To take this re-scattering processes into consideration a new term B_q^j is added to (B.4). Thus the above equation is written in a general form as

$$\phi_S^j = \sum_{q=-\infty}^{+\infty} B_q^j \frac{J'_q(ka_j)}{H'_q(ka_j)} H_q(kr_j) e^{\mathrm{i}q\theta_j} \tag{B.5}$$

where a_j is the radius of the cylinder. Then the scattered potential is the sum of the previous expression over the NC scatterers

$$\phi_S = \sum_{j=1}^{NC} \sum_{q=-\infty}^{+\infty} B_q^j \frac{J'_q(ka_j)}{H'_q(ka_j)} H_q(kr_j) e^{\mathrm{i}q\theta_j} \tag{B.6}$$

All the scatterers are rigid and impermeable. This is expressed by Neumann boundary condition

$$\frac{\partial \phi_{\mathrm{T}}}{\partial r_j} = 0 \qquad \text{on} \quad r_j = a_j \qquad \text{where} \quad j = 1 \text{ to } N \tag{B.7}$$

The radiation boundary condition is satisfied by the presence of the Hankel function while the complex value of the term B_q^j is defined to fulfill Neumann boundary condition. The total potential ϕ_{T} is the sum of the potentials of the incident and the scattered waves

$$\phi_{\mathrm{T}} = e^{\mathrm{i}kr\cos\theta} + \sum_{j=1}^{NC}\sum_{q=-\infty}^{+\infty} B_q^j \frac{J_q'(ka_j)}{H_q'(ka_j)} H_q(kr_j)e^{\mathrm{i}n\theta_j} \tag{B.8}$$

To apply the boundary conditions first (B.8) is expressed in terms of the local coordinates (r_j, θ_j) then the Bessel function is expanded according to Graf's addition theorem [129]. The resulting system of equations is

$$\begin{gathered} B_l^p + \sum_{j=1, j\neq p}^{NC}\sum_{q=-\infty}^{+\infty} B_q^j \frac{J_q'(ka_j)}{H_q'(ka_j)} e^{\mathrm{i}(q-l)\alpha_{jp}} H_{q-l}(kR_{jp}) = -I_p e^{\mathrm{i}l\frac{\pi}{2}} \\ 1 \leq p \leq NC \quad \text{and} \quad -\infty \leq l \leq +\infty \end{gathered} \tag{B.9}$$

where α_{jp} is the angle formed by the vector $\vec{jp}$ and the positive x-direction with j and p being the centres of the cylinders j and p, respectively. R_{jp} is the magnitude of this vector. All these spatial attributes are defined in Figure B.2.

If a higher value of q is considered a better accuracy is achieved. However, it was found that the results are accurate to four significant figures if $Q_{min} = 6$ where $-Q_{min} \leq q \leq +Q_{min}$ unless the cylinders are too close to each other [117].

$$\begin{gathered} B_l^p + \sum_{j=1, j\neq p}^{NC}\sum_{q=-Q_{min}}^{+Q_{min}} B_q^j \frac{J_q'(ka_j)}{H_q'(ka_j)} e^{\mathrm{i}(q-l)\alpha_{jp}} H_{q-l}(kR_{jp}) = -I_p e^{\mathrm{i}l\frac{\pi}{2}} \\ 1 \leq p \leq NC \quad \text{and} \quad -Q_{min} \leq l \leq +Q_{min} \end{gathered} \tag{B.10}$$

The above derivation could be found in more details in [117] and [130].

References

[1] I. Newton, *An hypothesis explaining the properties of light*, The history of the Royal Society; T. Birch, 3, London (1757), 247-305.

[2] J. C. Maxwell, *A dynamical theory of the electromagnetic field*, P R Soc London, 13, (1863 - 1864), 531-536.

[3] J. F. Mulligan, *Heinrich Rudolf Hertz: a collection of articles and addresses*; with an Introductory Biography by the editor, New York: Garland, 1994.

[4] A. Einstein, *Sidelights on relativity*, New York: Dover Publication Inc, 1983.

[5] E. Willett, *The basics of quantum physics: understanding the photoelectric effect and line spectra*, New York: Rosen Publishing Group, 2004.

[6] A. P. Lightman, *Great ideas in physics: the conservation of energy, the second law of thermodynamics, the theory of relativity, quantum mechanics*, New York: McGraw-Hill, 2000.

[7] S. Kichenassamy, *Nonlinear wave equations*, New York: M. Dekker Inc, 1996.

[8] J. D. Cutnell, K. W. Johnson, *Physics*, 3rd Edition, Hoboken, New Jersey: John Wiley and Sons, 1994.

[9] P. V. O'Neil, *Beginning partial differential equations*, New York: Wiley-Interscience Publication, 1999.

[10] E. Garber, *The language of physics: the calculus and the development of theoretical physics in Europe*, Boston: Birkhäuser, 1999.

[11] J. C. Nédélec, *Acoustic and electromagnetic equations: integral representations for harmonic problem*s, New York: Springer Verlag, 2001.

[12] K. Kawano, T. Kitoh, *Introduction to optical waveguide analysis: solving Maxwell's equations and the Schrödinger equation*, New York: Wiley-Interscience Publication, 2001.

[13] P. M. Morse, H. Feshbach, *Methods of theoretical physics*, New York: McGraw-Hill, 1953.

[14] D. T. Blackstock, *Fundamentals of physical acoustics*, New York: Wiley-Interscience Publication, 2000.

[15] M. A. Sumbatyan, A. Scalia, Contributor A. Scalia, *Equations of mathematical diffraction theory*, New York: CRC Press LLC, 2005.

[16] J. G. Harris, *Linear elastic waves*, Cambridge: Cambridge University Press, 2001.

[17] L. C. Wrobel, M. Aliabadi, *The boundary element method*, Chichester: John Wiley and Sons, 2002.

[18] M. Schanz, *Wave propagation in viscoelastic and poroelastic continua: a boundary element approach*, Berlin: Springer Verlag, 2001.

[19] C. Rajakumar, A. Ali, *The boundary element method: application in sound and vibration*, London: Taylor and Francis, 2004.

[20] F. B. Jensen, W. A. Kuperman, M. B. Portor, H. Schmidt, *Computational ocean acoustics*, New York: Springer Verlag, 1994.

[21] F. Ihlenburg, *Finite element analysis of acoustic scattering*, New York: Springer Verlag, 1998.

[22] A. Deraemaeker1, I. Babuška, P. Bouillard, *Dispersion and pollution of the FEM solution for the Helmholtz equation in one, two and three dimensions*, Int J Numer Meth Eng, 46 (1999) 471-499.

[23] F. Ihlenburg, I. Babuška, *Finite element solution of the Helmholtz equation with high wave number part I: The h-Version of the FEM*, Comput Math Appl, 30 (1995) 9, 9-37.

[24] W. Desmet, *Mid-frequency vibro-acoustic modelling: challenges and potential solutions*, Proc. of ISMA2002, 2 (2002) 835-862.

[25] P. Bettess, *Short-wave scattering: problems and techniques*, Phil Trans R Soc Lond A, 362 (2004) 421-443.

[26] J. M. Melenk, *On generalized finite element methods*, PhD thesis, University of Maryland, 1995.

[27] J. M. Melenk, I. Babuška, *The partition of unity finite element method: Basic theory and applications*, Comput Method Appl M, 139 (1996) 289-314.

[28] I. Babuška, J. M. Melenk, *The partition of unity method*, Int J Numer Meth Eng, 40 (1997) 727-758.

[29] P. Mayer, J. Mandel, *The finite ray element method for the Helmholtz equation of scattering: first numerical experiments*. UCD=CCM Report, 111 (1997). URL: http://www-math.cudenver.edu/ccm/reports.html.

[30] O. Laghrouche, P. Bettess, *Short wave modelling using special finite elements*, J Comput Acoust, 8 (2000) 189-210.

[31] O. Laghrouche, P. Bettess, R. J. Astley, *Modelling of short wave diffraction problems using approximating systems of plane waves*, Int J Numer Meth Eng, 54 (2002) 1501-1533.

[32] O. Laghrouche, P. Bettess, E. Perrey-Debain, J. Trevelyan, *Plane wave basis for wave scattering in three dimensions*, Commun Numer Meth En, 19 (2003) 715-723.

[33] E. Perrey-Debain, O. Laghrouche, P. Bettess, J. Trevelyan, *Plane wave basis finite elements and boundary elements for three dimensional wave scattering*, Philos T Roy Soc A, 362 (2004) 380, 561-577.

[34] O. Laghrouche, P. Bettess, E. Perrey-Debain, J. Trevelyan, *Wave interpolation finite elements for Helmholtz problems with jumps in the wave speed*, Comput Method Appl M, 194 (2005) 367-381.

[35] A. El Kacimi, O. Laghrouche, *Numerical modelling of elastic wave scattering in frequency domain by the partition of unity finite element method*, Int J Numer Meth Eng, 77 (2009) 12, 1646-1669.

[36] A. El Kacimi, O. Laghrouche, *Numerical analysis of two plane wave finite element schemes based on the partition of unity method for elastic wave scattering*, doi:10.1016/j.compstruc.2009.09.008.

[37] O. Laghrouche, M. S. Mohamed, *Locally enriched finite elements for the Helmholtz equation in two dimensions*, Comput Struct, doi:10.1016/j.compstruc.2008.04.006.

[38] R. J. Astley , P. Gamallo, G. Gabard, *Finite element models for acoustic propagation on mean flows*, Proceedings of 4th European Congress on Computational Methods in Applied Science and Engineering, Jyvaskyla Finland, II (2004) 20.

[39] P. Gamallo, R. J. Astley, *The partition of unity finite element method for short wave acoustic propagation on non-uniform potential flow*, Int J Numer Meth Eng, 65 (2006) 425-444.

[40] T. Mertens, P. Gamallo, R. J. Astley, P. Bouillard, *A mapped finite and infinite partition of unity method for convected acoustic radiation in axisymmetric domains*, Comput Method Appl M, 197 (2008) 4273-4283.

[41] P. Ortiz, E. Sanchez, *An improved partition of unity finite element model for diffraction problems*, Int J Numer Meth Eng, 50 (2001) 2727-2740.

[42] L. R. Higdon, *Absorbing boundary conditions for difference approximations to the multi dimensional wave equation*, Math Comput, 47 (1986) 437-459.

[43] B. Li, *A generalized conjugate gradient model for the mild slope equation*, Coast Eng, 23 (1994) 215-226.

[44] P. Ortiz, *Finite elements using a plane-wave basis for scattering of surface water waves*, Philos T Roy Soc A, 362 (2004) 525-540.

[45] T. Strouboulis, I. Babuška, K. Copps, *The design and analysis of the generalized finite element method*, Comput Method Appl M, 181 (2000) 43-69.

[46] T. Strouboulis, K. Copps, I. Babuška, *The generalized finite element method*, Comput Method Appl M, 190 (2001) 4081-4193.

[47] T. Strouboulis, I. Babuška, R. Hidajat, *The generalized finite element method for Helmholtz equation: Theory, computation, and open problems*, Comput Method Appl M, 195 (2006) 4711-4731.

[48] T. Strouboulis, R. Hidajat, I. Babuška, *The generalized finite element method for Helmholtz equation Part II: Effect of choice of handbook functions, error due to absorbing boundary conditions and its assessment*, Comput Method Appl M, 197 (2008) 364-380.

[49] T. Strouboulis, R. Hidajat, *Partition of unity method for Helmholtz equation: q-convergence for plane-wave and wave-band local bases*, Appl Math-Czech, 51 (2006) 2, 181-204.

[50] C. Farhat, I. Harari, L. Franca, *The discontinuous enrichment method*, Comput Method Appl M, 190 (2001) 6455-6479.

[51] J. S. Hesthaven, T. Warburton, *Nodal discontinuous Galerkin methods: algorithms, analysis, and applications* Springer Texts in Applied Mathematics 54, New York: Springer Verlag, 2008.

[52] C. Farhat, I. Harari, U. Hetmanuk, *A discontinuous Galerkin method with Lagrange multipliers for the solution of Helmholtz problems in the mid-frequency regime*, Comput Method Appl M, 192 (2003) 1389-1419.

[53] R. Tezaur, A. Macedo, C. Farhat, R. Djellouli, *Three-dimensional finite element calculations in acoustic scattering using arbitrarily shaped convex artificial boundaries*, Int J Numer Meth Eng, 53 (2002) 1461-1476.

[54] R. Tezaur, C. Farhat, *Three-dimensional discontinuous Galerkin elements with plane waves and Lagrange multipliers for the solution of mid-frequency Helmholtz problems*, Int J Numer Meth Eng, 66 (2005) 5, 796-815.

[55] L. Zhang, R. Tezaur, C. Farhat, *The discontinuous enrichment method for elastic wave propagation in the medium-frequency regime*, Int J Numer Meth Eng, 66 (2005) 13, 2086-2114.

[56] M. Amara, R. Djellouli, C. Farhat, *Convergence analysis of a discontinuous Galerkin method with plane waves and Lagrange multipliers for the solution of Helmholtz problems*, SIAM J Numer Anal, 47 (2009) 2, 1038-1066.

[57] E. Grosu, I. Harari, *Studies of the discontinuous enrichment method for two-dimensional acoustics*, Finite Elem Anal Des, 44 (2008) 272-287.

[58] A. Gillman, R. Djellouli, M. Amara, *A mixed hybrid formulation based on oscillated finite element polynomials for solving Helmholtz problems*, J Comput Appl Math, 204 (2007) 515-525.

[59] O. Cessenat, B. Despres, *Application of an ultra weak variational formulation of elliptic PDEs to the two-dimensional Helmholtz problem*, SIAM J Numer Anal, 35 1 (1998) 1, 255-299.

[60] O. Cessenat, B. Despres, *Using plane waves as base functions for solving time harmonic equations with the ultra weak variational formulations*, J Comput Acoust, 11 (2003) 2, 227-238.

[61] T. Huttunen, P. Monk, J. P. Kaipio, *Computational aspects of the ultra weak variational formulation*, J Comput Phys, 182 (2002) 27-46.

[62] T. Huttunen, P. Monk, F. Collino, J. P. Kaipio, *The ultra weak variational formulation for elastic wave problems*, SIAM J Sci Comp, 25 (2004) 1717-1742.

[63] T. Huttunen, J. P. Kaipio, P. Monk, *The perfectly matched layer for the ultra weak variational formulation of the 3D Helmholtz equation*, Int J Numer Methods Eng, 61 (2004) 7, 1072-1092.

[64] T. Huttunen, P. Gamallo, R. J. Astley, *Comparison of two wave element methods for the Helmholtz problem*, Commun Numer Meth En, 25 (2009) 35-52.

[65] P. Monk, D. Wang, *A least square method for the Helmholtz equation*, Comput Method Appl M, 175 (1999) 121-136.

[66] E. Giladi, J. B. Kellery, *A hybrid numerical asymptotic method for scattering problems*, J Comput Phys, 174 (2001) 226-247.

[67] E. Giladi, *Asymptotically derived boundary elements for the Helmholtz equation in high frequencies*, J Comput Appl Math, 198 (2007) 52-74.

[68] W. Desmet, *A wave based prediction technique for coupled vibro-acoustic analysis*, Ph.D. thesis, Katholieke Universiteit Leuven, 1998.

[69] B. van Hal, W. Desmet, D. Vandepitte, *Hybrid finite element wave-based method for steady-state interior structural-acoustic problems*, Comput Struct, 83 (2005) 167-180.

[70] A. H. Barnett, T. Betcke, *An exponentially convergent nonpolynomial finite element method for time-harmonic scattering from polygons*, submitted to SIAM J Sci Comp, 2009

[71] A. de La Bourdonnaye, *A microlocal discretization method and its utilization for a scattering problem*, Comptes Rendus de l'Académie des Science. Paris. Série I, 318 (1994) 385-388.

[72] A. de La Bourdonnaye, *Convergence of the approximation of wave functions by oscillatory functions in the high frequency limit*, Comptes Rendus de l'Académie des Science. Paris. Série I, 318 (1994) 765-768.

[73] A. de La Bourdonnaye, M. Tolentino, *Reducing the condition number for microlocal discretization problems*, Philos T Roy Soc A, 362 (2004) 541-559.

[74] E. Perrey-Debain, J. Trevelyan, P. Bettess, *New special wave boundary elements for short wave problems*, Commun Numer Meth En, 18 (2002) 4, 259-68.

[75] E. Perrey-Debain, J. Trevelyan, P. Bettess, *Use of wave boundary elements for acoustic computations*, J Comput Acoust, 11 (2003) 305-321.

[76] E. Perrey-Debain, J. Trevelyan, P. Bettess, *Plane wave interpolation in direct collocation boundary element method for radiation and wave scattering: numerical aspects and applications*, J Sound Vib, 261 (2003) 839-58.

[77] E. Perrey-Debain, J. Trevelyan, P. Bettess, *P-wave and S-wave decomposition in boundary integral equation for plane elastodynamic problems*, Commun Numer Meth En, 19 (2003) 12, 945-958.

[78] E. Perrey-Debain, J. Trevelyan, P. Bettess, *Wave boundary elements: a theoretical overview presenting applications in scattering of short waves*, Eng Anal Bound Elem, 28 (2004) 131-141.

[79] E. Perrey-Debain, *Plane wave decomposition in the unit disc: convergence estimates and computational aspects*, J Comput Appl Math, 193 (2006) 140-156.

[80] H. Bériot, E. Perrey-Debain, M. Ben Tahar, C. Vayssade, *Plane wave basis in Galerkin BEM for bidimensional wave scattering*, Eng Anal Bound Elem, 34 (2010) 130143.

[81] S. N. Chandler-Wilde, S. Langdon, L. Ritter, *A high-wavenumber boundary-element method for an acoustic scattering problem*, Philos T Roy Soc A, 362 (2004) 647-671.

[82] S. N. Chandler-Wilde, S. Langdon, *A Galerkin boundary element method for high frequency scattering by convex polygons*, SIAM J Numer Anal, 45 (2007) 610-640.

[83] S. Langdon, S. N. Chandler-Wilde, *A wavenumber independent boundary element method for an acoustic scattering problem*, SIAM J Numer Anal, 43 (2006) 2450-2477.

[84] T. Huttunen, T. Luostari, P. Monk, *Development of the ultra weak variational formulation*, Proceedings of WAVES2009, Pau France (2009) 92-93.

[85] T. Luostari, T. Huttunen, P. Monk, *The ultra-weak variational formulation using Bessel basis functions*, Proceedings of MAFELAP 2009, Uxbridge UK 2009.

[86] I. Herrera, F. J. Sabina , *Connectivity as an alternative to boundary integral equations: Construction of bases*, Applied Physical and Mathematical Sciences, 75 (1978) 2059-2063.

[87] P. Bettess, J. A. Bettess, *A profile matrix solver with built-in constraint facility*, Eng Computation, 3 (1986) 3, 209-216.

[88] T. H. Havelock, *The pressure of water waves on a fixed obstacle*, Proc Roy Soc A, 175 (1940) 409-421.

[89] P. M. Morse, H. Feshbach, *Methods of theoretical physics*, New York: McGraw-Hill Book Company Inc., 1953.

[90] F. Ihlenburg, I. Babuška, S. Sauter, *Reliability of finite element methods for the numerical computation of waves*, Adv Eng Softw, 28 (1997) 417-424.

[91] M. S. Mohamed, A. El Kacimi, O. Laghrouche, *Multi-Wavelength sized finite elements for Helmholtz wave problems*, Proceedings of WAVES2009, Pau France (2009) 244-245.

[92] K. Gerdes, *The conjugated vs. the unconjugated infinite element method for the Helmholtz equation in exterior domains*, Comput Method Appl M, 152 (1998) 125-145.

[93] B. Engquist, A. Majda, *Radiation boundary conditions for acoustic and elastic calculations*, Commun Pur Appl Math, 32 (1979) 313-357.

[94] A. Bayliss, E. Turkel, *Radiation boundary conditions for wave-like equations*, Commun Pur Appl Math, 33 (1980) 707-725.

[95] D. Givoli, *Non-reflecting boundary conditions: a review*, J Comput Phys, 94 (1991) 1-29.

[96] J. B. Keller, D. Givoli, *Exact non-reflecting boundary conditions*, J Comput Phys, 82 (1989) 172-192.

[97] D. Givoli, J. B. Keller, *Non-reflecting boundary conditions for elastic waves*, Wave Motion, 12 (1990) 261-279.

[98] V. S. Ryabenkii S. V. Tsynkov, *Artificial boundary conditions for the numerical solution of external viscous flow problems*, Siam J Numer Anal, 32 (1995) 1355-1389.

[99] O. Laghrouche, A. El-Kacimi, J. Trevelyan, *A comparison of NRBCs for PUFEM in 2D Helmholtz problems at high wave numbers*, J Comput Appl Math, doi:10.1016/j.cam.2009.08.014.

[100] R. Sugimoto, P. Bettess, J. Trevelyan, *A Numerical integration scheme for special quadrilateral finite elements for Helmholtz equation*, Commun Numer Meth En, 19 (2002) 233-245.

[101] P. Bettess, J. Shirron, O. Laghrouche, B. Peseux, R. Sugimoto, J. Trevelyan, *A numerical integration scheme for special finite elements for Helmholtz equation*, Int J Numer Meth Eng, 56 (2003) 531-552.

[102] E. Darrigrand, *Coupling of fast multipole method and microlocal discretization for the 3-D Helmholtz equation*, J Comput Phys, 181 (2002) 126-154.

[103] J. Trevelyan, M. E. Honnor, *A Numerical coordinate transformation for efficient evaluation of oscillatory integrals over boundary element*, J Integral Equations Appl, 21 (2009) 3, 449-470.

[104] W. B. Gordon, *Far-Field Approximation to the Kirchhoff-Helmholtz Representations of Scattered Fields*,IEEE T Antenn Propag, July (1975), 590-592.

[105] G. Gabard, *Exact integration of polynomial exponential products with application to wave-based numerical methods*, Commun Numer Meth En, 25 (2009) 3, 237-246.

[106] G. N. Watson, *The Diffraction of Electric Waves by the Earth*, Proc R Soc Lon Ser-A, 95 (1918) 83-99.

[107] B. Van der Pol, H. Bremmer, *The diffraction of electromagnetic waves from an electrical point source round a finitely conducting sphere, with applications to radiotelegraphy and the theory of the rainbow*, Philos Mag, 24 (1937) 825-864.

[108] W. Franz, R. Galle, *Semiasymptotische Reihen für die Beugung einer ebenen Welle am Zylinder*, Zeitschrift Naturforschung Teil A, 10 (1955) 374-378.

[109] W. Franz, P. Beckmann, *Creeping waves for objects of finite conductivity*, IEEE T Antenn Propag, 4 (1956) 3, 203-208.

[110] W. Franz, *Theorie der Beugung Elektrornagnetischer Wellen*, Berlin: Springer, 1957

[111] P. C. Clemmow, *On the theory of the diffraction of a plane wave by a large perfectly conducting circular cylinder*, Proc R Soc Lon Ser-A, 264 (1961), 235-245.

[112] R. C. MacCamy, R. A. Fuchs, *Wave forces on piles: a diffraction theory*, Technical Memorandum No. 69, US Army Corps of Engineers, Beach Erosion Board (1954).

[113] H. S. Chen, C. C. Mei, *Wave forces on a stationary platform of elliptical shape*, J Ship Res, 17 (1973) 2, 61-71.

[114] A. N. Williams, *Wave forces on an elliptic cylinders*, J Waterw Port C-ASCE, 111 (1985) 2, 433-449.

[115] P. Hillion, *Diffraction of plane waves on a parabolic cylinder*, Rep Math Phys, 37 (1996) 3, 349-364.

[116] A. M. Mansour, A. N. Williams, K. H. Wang, *The diffraction of linear waves by a uniform vertical cylinder with cosine-type radial perturbations*, Ocean Eng, 29 (2002) 239-259.

[117] C. M. Linton, D. V. Evans, *The interaction of waves with arrays of vertical circular cylinders*, J Fluid Mech, 215 (1990) 549-569.

[118] P. A. Martin, *Multiple scattering interaction of time-harmonic waves with N obstacles*, Cambridge: Cambridge University Press, 2006.

[119] Q. Carayol, F. Collino, *Error estimates in the fast multipole method for scattering problems part 1: truncation of the jacobi-anger series*, ESAIM-Math Model Num, 38 (2004) 2, 371-394.

[120] J. Ford, *Wavelet-based Preconditioning of Dense Linear systems*, PhD thesis, University of Liverpool, 2001.

[121] Y. A. Erlangga, *A robust and efficient iterative method for the numerical solution of the Helmholtz equation*, PhD thesis, Delft University of Technology, 2005.

[122] Y. Saad, M. H. Schultz, *GMRES: a generalized minimal residual algorithm for solving nonsymmetric linear systems*, SIAM J Sci Stat Comp, 7 (1986) 3, 856-869.

[123] R. W. Freund, N. M. Nachtigal, *QMR: a quasi-minimal residual method for non-Hermitian linear systems*, Numer Math, 60 (1991) 3, 315-339.

[124] Y. Saad, *Iterative methods for sparse linear systems*, Boston: PWS Publishing Company, 1996.

[125] I. Daubechies, *Ten lectures on wavelet*, Philadelphia: SIAM, 1992.

[126] L. Marin, D. Lesnic, V. Mantic, *Treatment of singularities in Helmholtz-type equations using the boundary element method*, J Sound Vib, 278 (2004) 39-62.

[127] R. Djellouli, C. Farhat, A. Macedo, R. Tezaur, *Finite element solution of two-dimensional acoustic scattering problems using arbitrarily shaped convex artificial boundaries*, J Comput Acoust, 8 (2000) 81-100.

[128] R. Kechroud, A. Soulaimani, X. Antoine, *A performance study of plane wave finite element methods with a Padé-type artificial boundary condition in acoustic scattering*, Adv Eng Softw, 40 (2009) 738-750.

[129] I. S. Gradshteyn, I. M. Ryzhik, *Tables of integrals, series and products*, New York: Academic Press, 1965.

[130] P. McIver, D. V. Evans, *Approximation of wave forces on cylinder arrays*, Appl Ocean Res, 6 (1984) 101-107.

[131] T. Huttunen, P. Monk, *The use of plane waves to approximate wave propagation in anisotropic media*, J Comput Math, 25 (2007) 350-367.

[132] M. E. Honnor, J. Trevelyan, P. Bettess, M. Elhachemi, O. Hassan, K. Morgan, J. Shirron, *An integration scheme for electromagnetic scattering using plane wave edge elements*, Adv Eng Softw, 40 (2009) 58-65.

[133] M. E. Honnor, J. Trevelyan, D. Huybrechs, *Numerical evaluation of 2D partition of unity boundary integrals for Helmholtz problems*, J Comput Appl Math, doi:10.1016/j.cam.2009.08.012.

[134] D. Huybrechs, S. Vandewalle, *On the evaluation of highly oscillatory integrals by analytic continuation*, SIAM J Numer Anal, 44 (2006) 1026-1048.

[135] D. Huybrechs, S. Vandewalle, *A sparse discretisation for integral equation formulations of high frequency scattering problems*, SIAM J Sci Comput, 6 (2007) 2305-2328.